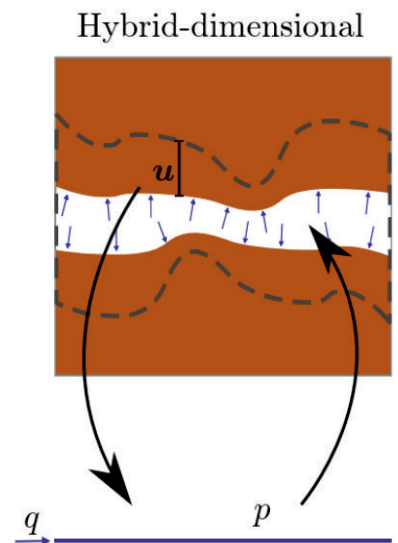
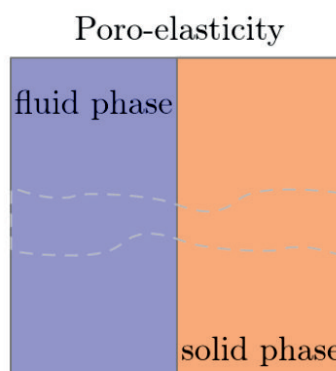
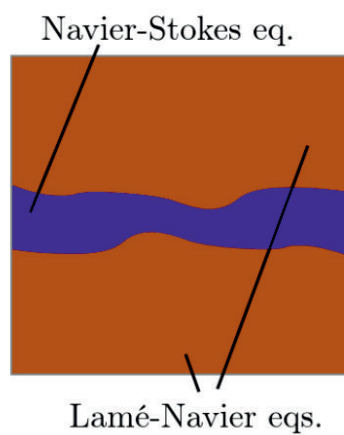


Hydro-mechanical coupling in fractured rocks: modeling and numerical simulations

Carlo Vinci



Hydro-mechanical coupling in fractured rocks: modeling and numerical simulations

Von der Fakultät für Bau- und Umweltingenieurwissenschaften
der Ruhr-Universität Bochum zur Erlangung
des Grades Doktor-Ingenieur (Dr.-Ing.) genehmigte

Dissertation

von

Carlo Vinci

Bochum 2014

Abstract

A comprehensive understanding of subsurface fluid flow is necessary for an efficient management of natural reserves and energy resources. Flow through fractured geological media is a subject in several areas of engineering and geosciences, for example oil and gas production, water reservoir management, and geothermal energy exploitation. Characterization of subsurface fluid flow requires accounting for hydro-mechanical coupling between fluid-pressure variations and rock deformation.

Within this thesis, modeling aspects and numerical simulations of a compressible fluid along a single compliant hydraulic conduit, such as a joint or a fracture, are investigated. To efficiently model transport processes through fractures with realistic geometries, i.e., characterized by high aspect ratios, a *hybrid-dimensional* approach is derived. The theoretical approach is complemented by a dimensional analysis of the governing equations to characterize hydro-mechanical effects with respect to different material and geometrical parameters.

Field data from well pumping tests are numerically approximated to obtain a set of parameters characterizing the surrounding fractured rock. Further numerical investigations comprise simulation of periodic pumping tests and pressure-sensitivity analysis to various parameters, e.g., rock stiffness or pumping period. An analysis of flow induced by solid deformation follows, where attenuation related to fracture flow as well as to leak-off is investigated.

Results of the theoretical analyses and of the simulations suggest that coupling effects quantitatively increase with the aspect ratio of the analyzed fracture and are closely related to the non-local deformation of the fracture boundaries. The presented approach allows for an efficient modeling of fluid flow through thin fractures. The comparison of field data with numerical results revealed that the hybrid-dimensional approach is an effective tool to constrain effective properties of fractured materials and, therefore, to improve understanding of subsurface fluid flow.

Zusammenfassung

Ein umfassendes Verständnis von Fluidströmungen durch geologische Formationen ist für das effiziente Management von natürlichen Lagerstätten und Energieressourcen unentbehrlich. Die Strömung durch geklüftete, poröse Medien ist ein wichtiger Gegenstand in verschiedenen Bereichen der Ingenieur- und Geowissenschaften, beispielsweise der Öl- und Gasproduktion, der Überwachung von Wasserlagerstätten sowie der Nutzung geothermischer Energie. Die Charakterisierung der unterirdischen Strömungen erfordert dabei die Berücksichtigung der hydromechanischen Kopplung von Fluiddruckänderungen und Gesteinsdeformationen.

Im Rahmen der vorliegenden Arbeit werden Modellierungsaspekte und numerische Simulationen eines kompressiblen Fluids entlang eines nachgiebigen Strömungskanals, wie zum Beispiel einer Kluft oder eines Risses, untersucht. Um die Transportprozesse in Rissen mit realistischen Geometrien, d. h. mit einem großen Längen-/Seitenverhältnis, effizient zu modellieren, wird ein hybrid-dimensionaler Ansatz entwickelt. Dieser Modellierungsvorschlag wird durch eine Dimensionsanalyse der maßgeblichen Gleichungen ergänzt, um die hydromechanischen Effekte im Hinblick auf verschiedene Material- und Geometrieparameter zu beschreiben.

Felddaten aus Bohrlochpumpversuchen werden numerisch untersucht um Parametersätze zu erhalten, die das umgebende, geklüftete Gestein realitätsnah approximieren. Weitere numerische Studien enthalten Untersuchungen periodischer Pumpversuche sowie eine Druckempfindlichkeitsanalyse verschiedener Parameter, wie Gesteinsfestigkeit oder Pumpzyklen. Im letzten Teil der Arbeit werden die Resultate aus den vorangegangenen Abschnitten genutzt, um das effektive (viskoelastische) Materialverhalten fluidgefüllter Risse numerisch zu untersuchen. Homogenisierte Materialeigenschaften von einfachen Modellsystemen werden dazu im Zeit- und Frequenzbereich analysiert und diskutiert.

Die Ergebnisse der theoretischen Analyse und der Simulationen lassen darauf schließen, dass die Kopplungseffekte mit zunehmendem Seitenverhältnis des untersuchten Risses quantitativ anwachsen und eng mit nicht-lokalen Deformationen der Rissränder verbunden sind. Der vorgestellte Ansatz erlaubt dafür eine effiziente Modellierung von Fluidströmungen durch dünne Risse. Der Vergleich von Felddaten und numerischen Ergebnissen zeigt, dass der hybrid-dimensionale Ansatz ein effektives Mittel ist, um die effektiven Eigenschaften von geklüftetem Material zu charakterisieren und somit zu einem verbesserten Verständnis von unterirdischen Fluidströmungen durch geklüftete, poröse Gesteinmaterialien führt.

Contents

List of Figures	III
List of Tables	V
Notation	VII
1 Introduction	1
1.1 Motivation	1
1.2 Aims and outline	3
2 Modeling hydro-mechanical coupling: theoretical aspects	5
2.1 Introduction	5
2.2 Navier-Stokes and Lamé-Navier equations	7
2.3 Poro-elastic theory	9
2.4 Hybrid-dimensional approach	13
2.5 Summary	20
3 Numerical modeling of the hydro-mechanics of fractures	23
3.1 Introduction	23
3.2 Background and modeling approaches	25
3.3 Analysis of the modeling equations	34
3.4 Numerical modeling	38
3.5 Discussion	45
3.6 Conclusions	46
4 The imprint of hydro-mechanics in periodic pumping tests	49
4.1 Introduction	49
4.2 Background and modeling approaches	50
4.3 Results	54
4.4 Discussion	64
4.5 Conclusions	66

5	On attenuation associated with fracture flow	69
5.1	Introduction	69
5.2	Modeling approach	70
5.3	Results	74
5.4	Discussion	82
5.5	Conclusions	84
	Conclusions	87
	Bibliography	91
	Curriculum Vitae	99

List of Figures

1.1	Example of an intact rock and a naturally fractured rock . . .	1
1.2	Boreholes configuration at the testing location, Kemnader See, Bochum, Germany (source: Google Earth, modified with lines)	3
2.1	Example of a hydro-mechanical problem induced by fluid to solid coupling	6
2.2	Example of a hydro-mechanical problem induced by solid to fluid coupling	7
2.3	Modeling approaches to account for hydro-mechanical coupling	9
2.4	Feasibility of modeling approaches depending on the aspect ratio of the analyzed fracture	11
2.5	Generic fracture geometry written in cylindrical coordinates . .	14
2.6	Accounting for leak-off in the hybrid-dimensional approach . .	19
3.1	Experimental setup: injection and monitoring boreholes	25
3.2	Experimental pressure transients in injection and monitoring boreholes	26
3.3	Borehole intersecting a single horizontal fracture modeled by elliptical geometry	27
3.4	Boundary value problem for the poro-elastic approach	28
3.5	Boundary value problem for the hybrid-dimensional approach .	29
3.6	Non-local character of fracture deformation due to local pressure changes	32
3.7	Pressure transient along a fracture and deviation between solutions of the poro-elastic approach and hybrid-dimensional approach	41
3.8	Results for a simulation of a high-aspect-ratio fracture using the hybrid-dimensional approach	42
3.9	Pressure evolution at the injection borehole and at monitoring borehole: comparison of numerical solutions and field data . . .	44
4.1	Analyzed configuration: injection well and monitoring wells intersecting a single ellipsoidal fracture	51

4.2	Periodic pumping: geometry and initial-boundary-value problem of the surrounding rock material	52
4.3	Periodic pumping: geometry and initial-boundary-value problem related to fluid flow	52
4.4	Transient pressure at injection and monitoring boreholes: full hydro-mechanic and diffusion-based approach	55
4.5	Contour of logarithm of maximum pressure at monitoring borehole for combinations of fracture initial aperture and rock dry modulus	57
4.6	Contour of logarithm of storage multiplier for combinations of fracture initial aperture and rock dry modulus	58
4.7	Contour of pressure in the fracture along the time domain. Transport of pressure is induced by a pressure boundary condition at the injection well	59
4.8	Periodic pumping test: (top) logarithm of amplitude ratios vs. phase shifts; (bottom) phase shift vs. normalized distance . . .	61
4.9	Amplitude ratio vs. phase shift at monitoring boreholes for different pumping periods, obtained with the diffusion-based approach and the hybrid-dimensional approach	63
5.1	Geometry of the unit cell: two-dimensional poro-elastic rock containing two interconnected fractures	71
5.2	One-dimensional domains of the two interconnected fractures .	72
5.3	Inverse quality factor for fracture flow, leak-off only, and for both processes	73
5.4	Effect of vertical fracture aperture on characteristic frequency and attenuation	75
5.5	Inverse quality factor for a deformable and an undeformable vertical fracture	75
5.6	Characteristic frequencies for different values of the logarithm of the aspect ratio	76
5.7	Comparison of full hydro-mechanical results, diffusion and convection, and simple diffusion: amplitude of the inverse quality factor vs. logarithm of aspect ratio	78
5.8	Rectangular shaped vertical fracture	78
5.9	Vertical fracture intersecting the horizontal fracture with angle γ	79
5.10	Polar plot of the normalized attenuation and critical frequencies for different intersecting angles	80
5.11	Dimensionless attenuation for an artificially impermeable rock .	81
5.12	Dimensionless attenuation for a permeable rock	82
5.13	Dimensionless attenuation for leak-off and fracture flow	83

List of Tables

2.1	Comparison of modeling approaches	21
3.1	Comparison of the governing equations of the hybrid-dimensional approach and the radial component of the poro-elastic approach	36
3.2	Parameters used for the numerical examples with a low-aspect-ratio fracture	39
3.3	Parameters used for the numerical examples with high-aspect-ratio fractures	43
4.1	Parameters used for the simulation of periodic pumping tests .	53
4.2	Ranges of parameters used for the sensitivity analyses	56
5.1	Material parameters applied in the numerical investigation . . .	77

Notation

Latin characters

a [m]	fracture half-length
A [-]	dimensionless number scaling time-dependent pressure term
AR [-]	fracture aspect ratio ($AR = 2a/\delta$)
\mathbf{b} [kg/m ² s ²]	body forces
B [-]	dimensionless number scaling nonlinear diffusion
C [-]	dimensionless number scaling coupling effects
C_C [m/s]	convection coefficient
C_D [m ² /s]	hydraulic diffusivity
D [m ² /s]	hydraulic diffusivity
D_F [m/s]	fracture diffusivity
DEV [-]	relative deviation between numerical solutions
E [Pa]	average Young's modulus of the rock's solid constituents
f [Hz]	frequency
G [Pa]	shear modulus
G_{eff} [Pa]	effective shear modulus
\mathbf{I} [-]	second order unity tensor
J [-]	Jacobian
K [Pa]	bulk modulus
K_d [Pa]	bulk modulus of the dry rock
K_{eff} [Pa]	effective bulk modulus
K^f [Pa]	bulk modulus of the fluid
K^s [Pa]	grain bulk modulus of the solid
k [m ²]	fracture permeability derived from the parallel plate approximation

k^s [m ²]	intrinsic permeability
k_{rock}^s [m ²]	intrinsic permeability of rock
l [m]	length in a deformed configuration
l_0 [m]	length in an undeformed configuration
L [m]	distance between injection and monitoring boreholes
M [Pa]	Biot's coupling coefficient
\mathbf{n} [-]	vector orthogonal to fracture surface
p [Pa]	fluid pressure measured relative to p_0
\bar{p} [Pa]	pressure boundary condition
p_0 [Pa]	initial pressure
p_{rock} [Pa]	pressure in the poro-elastic rock domain
p_{PE} [Pa]	pressure: numerical solution of poro-elastic approach
p_{HD} [Pa]	pressure: numerical solution of hybrid-dimensional approach
q [m ³ /s]	fluid flux
\bar{q} [m ³ /s]	flux boundary condition
r [m]	radial component of the position vector in the current configuration
r_w [m]	radius of injection borehole
R [m]	radial component of the position vector in an undeformed configuration
s_{F} [1/Pa]	specific fracture storage capacity
S_{F} [m/Pa]	bulk fracture storage capacity
t [s]	time
t_{end} [s]	size of computational time domain
\mathbf{T} [Pa]	total stress
\mathbf{u}_{s} [m]	displacement of the solid phase
\mathbf{v}_{f} [m/s]	velocity of the fluid phase
v_{fr} [m/s]	radial component of \mathbf{v}_{f}
\mathbf{v}_{s} [m/s]	velocity of the solid phase
v_{sr} [m/s]	radial component of \mathbf{v}_{s}
v_{sz} [m/s]	vertical component of \mathbf{v}_{s}
V [m ³]	arbitrary volume
V_{f} [m ³]	volume of fracture domain
\mathbf{w}_{f} [m/s]	velocity of the fluid relative to the solid
\bar{w} [m/s]	prescribed fluid flux per unit area
w_{fr} [m/s]	radial component of \mathbf{w}_{f}
w_{fN} [m/s]	seepage velocity in direction orthogonal to the fracture surface
z [m]	vertical component of the position vector in the current configuration

Greek characters

α [-]	Biot-Willis parameter
α_s [-]	storage multiplier
β_f [1/Pa]	isothermal fluid compressibility
δ [m]	fracture aperture
δ_0 [m]	fracture aperture constant in time
$\delta_0(r_w)$ [m]	initial fracture aperture at injection borehole
η^{fR} [Pa·s]	effective viscosity of the fluid
θ [-]	angle from a reference direction
λ [Pa]	Lamé's first parameter
μ [Pa]	Lamé's second parameter
ν [-]	Poisson's ratio
ρ [kg/m ³]	density of the mixture
ρ^{fR} [kg/m ³]	effective density of the fluid
ρ^{sR} [kg/m ³]	effective density of the solid
σ_E^s [Pa]	Cauchy extra stress tensor (effective stress)
σ^m [Pa]	mean stress
ϕ [-]	porosity
Ψ^* [-]	dimensionless variable
$\tilde{\Psi}$ []	characteristic variable for dimensional analysis

Notation specific to Chapter 4

Latin characters

A_i [Pa]	pressure amplitude at monitoring wells
A_0 [Pa]	pressure amplitude at injection well
L_{diff} [m]	diffusion length
L_i [m]	distance between injection and monitoring boreholes
p_{eq} [Pa]	pressure at steady state
p_{max} [Pa]	maximum pressure reached at injection well
r^* [-]	normalized position
t_{eq} [s]	time to reach a steady state
T [s]	pumping period

Greek characters

$\Delta\varphi$ [-]	phase shift
φ_i [-]	signal phase at monitoring wells
φ_0 [-]	signal phase at injection well

Notation specific to Chapter 5

Latin characters

c_1 [-]	generic coefficient for a line equation
c_2 [-]	generic coefficient for a line equation
D [m ² /s]	hydraulic diffusivity
f_c [Hz]	characteristic frequency
$f_{c,fr}$ [Hz]	characteristic frequency of fracture flow
$f_{c,lo}$ [Hz]	characteristic frequency of leak-off
$M(f)$ [Pa]	complex stiffness
Q [-]	quality factor
t_{appl} [s]	application time of the pressure boundary condition

Greek characters

γ [-]	intersection angle between fractures
δ_h [-]	initial and maximum aperture of the horizontal fracture
δ_v [-]	initial and maximum aperture of the vertical fracture
$\varepsilon_{s,yy}$ [-]	Fourier-transformed averaged strain of the rock matrix
ξ [m]	local coordinate system in the one-dimensional models of the fractures
σ_{yy} [Pa]	stress component in vertical direction
$\bar{\sigma}_{yy}(f)$ [Pa]	Fourier-transformed averaged total stress

Chapter 1

Introduction

1.1 Motivation

The increasing need for energy and natural resources requires an optimized management of the available reserves. Fluid flow through fractured material is crucial for provision of liquids or heat from the subsurface or their storage in it. Understanding subsurface fluid flow allows for an improved control over procedures related to energy or fluid exploitation. Injection or production of fluids related to subsurface reservoirs are procedures that concern several areas of engineering or geosciences. Production of oil and gas from wells constitutes the very heart of the hydrocarbon industry [e.g., 31]. Enhanced recovery methods involve fluid injection into the reservoirs to maintain reservoir pressure. One fluid is injected in a reservoir, for example a gas, to improve oil displacement. In geothermal research, flow is induced through fractured rock to extract heat transported with the fluid.

Fractures often represent fluid conduits that allow increased flow in comparison to flow through a non-fractured porous material, cf. Figure 1.1. Preferential



Figure 1.1: Example of an intact rock (left) and of a naturally fractured rock (right). Rock fractures often represent preferential flow paths that greatly increase permeability compared to fluid flow through intact rocks.

paths can be natural or artificially induced fractures. For various applications in reservoir engineering the aim is to increase fluid flux taking place through the fractured rock. At oil and gas drilling sites, an enhanced reservoir permeability results in an increased oil or gas production rate. In the case of water reservoirs, water management can be optimized exploiting the available fluid resources [e.g., 37, 60]. For the operation of geothermal power plants, increase of permeability is crucial not only to improve fluid flow but also to expand the area between fluid and rock and optimize heat exchange. In several areas related to fluid or heat production, the procedure of hydraulic fracturing is commonly applied. Massive fluid amounts are injected from a well to fracture the neighboring rock and, thus, increase permeability of the reservoir.

The aim of other applications is to minimize the fluid flux through a certain rock domain. In the field of research for CO₂ sequestration or for waste disposal [e.g., 26], the objective is to store (supercritical) fluids within a rock domain and minimize transport through it. All reservoir-engineering applications share the necessity to know the hydraulic and mechanical properties of the analyzed domain. For procedures involving one or more boreholes, information characterizing the neighboring reservoir is crucial before and after any procedure is performed. For example, knowledge about the environment surrounding a well is essential to adjust the required fluid volume and flux for a safe and efficient application of hydraulic fracturing. Furthermore, characterization of the fractured rock is needed to estimate the results of hydraulic fracturing.

Permeability or permeability anisotropy as well as storage capacity values of the fractured rock are needed to estimate flow rates of the fluid. Different procedures have been investigated to efficiently characterize the subsurface. Non destructive testing procedures have been investigated, based on the interpretation of the propagation of mechanical waves in porous rock material [52, 53, 55, 70, 90]. Frequently, pumping procedures are performed in an injection well. Pressure or flux information from the injection point as well as from other monitoring boreholes is used and interpreted to mechanically and hydraulically describe the surrounding reservoir [3, 20, 34, 57]. Conventionally pulse tests have been analyzed [18, 49, 50, 91] as well as harmonic [74] or non-harmonic [75] periodic pumping signals with single frequency or multi frequency content [19]. With the limited information gained from wells, interpretation of data obtained at single points is the key to describe and characterize domains surrounding boreholes, cf. Figure 1.2. Numerical modeling of flow through fractures and, therefore, of the resulting pressure transients, can be used as a predictive tool to constraint effective properties of fractured material.

1.2 Aims and outline

The motivation of this work is to explain critical observations recorded during pumping experiments at a field location at Kemnader See, cf. Figure 1.2 (left). Pressure transients induced by a periodic flux showed inverse responses to pumping [36, 88, 98, 100] that seem at first counterintuitive and could not be explained by modeling approaches developed so far. In this work, efficient numerical methods for modeling of fractured material are tested that can account for hydro-mechanically induced phenomena.



Figure 1.2: Field test location, Kemnader See, Bochum, Germany: (left) configuration of boreholes BK1-BK3. Pumping operations are performed in one borehole and pressure is monitored at all three wells. Interpretation and inversion of information recorded at the boreholes allows for characterization of the material surrounding the wells (source: Google Earth, modified with lines); (right) borehole inspection with different sensors to characterize the rock surrounding the well.

This investigation focuses mainly on two closely linked objectives. First, the aim is to understand the occurring physical processes, in particular the coupling effects due to fluid and solid interaction. For this purpose, investigations of the sensitivity of occurring physical phenomena to various material and geometrical properties of the fluid and the solid material are involved. Based on that knowledge, a further objective is to characterize fractured rock by means of effective hydraulic and material properties. Subsurface fluid flow models are developed to allow for efficient analyses of data from well testing procedures. Analysis of pressure transients in wells or along fractures allows for investigations of the occurring physical phenomena related to hydro-mechanical coupling and for hydraulic characterization of the surrounding rocks. Particular consideration is given to characterization of rock domains containing high-aspect-ratio inclusions and to understanding the role of conduit-aspect ratio on the occurring physical phenomena [99].

This work is structured in the following way:

- Theoretical aspects for modeling hydro-mechanical problems are analyzed in Chapter 2. A novel modeling scheme, the *hybrid-dimensional approach*, is derived that efficiently addresses hydro-mechanical coupled problems involving high-aspect-ratio inclusions at reduced computational effort.
- Fluid injection in a single horizontal ellipsoidal fracture is modeled in Chapter 3 to investigate the physical processes involved in fluid flow in deformable conduits and to understand the importance of the coupling between fluid flow and rock deformation. Numerical results obtained from the hybrid-dimensional approach are first compared to the well established theory of poro-elasticity. Furthermore, the hybrid-dimensional approach is used to approximate pressure transients recorded during field experiments to characterize the fractured rock surrounding boreholes at the Kemnader See, Bochum, Germany.
- Based on the field data fitting, periodic pumping tests from a vertical borehole are simulated to investigate the diagnostic potential of periodic pumping tests for hydro-mechanical effects on subsurface-fluid flow, cf. Chapter 4. Numerical results are analyzed to characterize and quantify hydro-mechanics in comparison to diffusion effects. Furthermore, sensitivity analyses are performed, based on parameter sweep studies.
- In Chapter 5, fractured domains are investigated based on the occurring fluid-flow phenomena induced by deformation. Properties of fractured rock are investigated by characterization of dissipative flow mechanisms that occur at scales related to the fracture size. Furthermore, sensitivity studies with respect to various geometrical and material parameters are performed to understand the role of high-aspect-ratio inclusions in hydro-mechanical coupling.
- Finally, the main results of this investigation are summarized in the conclusions.

It should be noted that parts of this work have been published or will be soon submitted for publishing in scientific peer-reviewed journals. The results of Chapter 3 have been published in *Water Resources Research* by Vinci et al. [98]. Chapters 4 and 5 will be soon submitted for publication at *Geophysical Journal International* and *Geophysical Research Letters*, respectively [99, 100].

Chapter 2

Modeling hydro-mechanical coupling: theoretical aspects

2.1 Introduction

Analysis of fluid flow through fractured media requires to account not only for the fluid flow and the mechanics of the solid material, but also for interactions between the two constituents [e.g., 2, 65, 104]. To properly model fully saturated fractured media, one has to allow for hydro-mechanical coupling of the equations governing the solid deformation as well as the equations governing the fluid pressure evolution [e.g., 62, 63, 88, 98]. Rock deformation and fluid pressure transport cannot be investigated separately, but for strongly simplified cases [e.g., 30, 76].

As a generic example of a coupled hydro-mechanical problem, a fluid-filled fracture surrounded by rock material is considered, cf. Figure 2.1 (left). On the one hand, a coupled problem can be induced by fluid pressure changes that affect the solid deformation (fluid to solid coupling, cf. Figure 2.1). An induced fluid flux \bar{q} transports fluid pressure p along a conduit. Pressure variations along the fluid domain act on the conduit's boundaries and deform the surrounding solid material. In response to the induced deformations, the rock acts on the fluid domain with surface stresses \mathbf{t} , which affect the fluid pressure p and the volume of the fluid domain. On the other hand, displacement applied on the solid material can induce fluid flow (solid to fluid coupling, cf. Figure 2.2). Deformation of the solid constituent generates surface stresses \mathbf{t} on the boundaries of the fluid domain, which deform accordingly. A reduction in space available for the fluid induces fluid flow $\mathbf{q} \neq 0$ along the conduit. In turn, an increase in conduit volume decreases pressure p . In addition to the two-way coupling, indirect coupling effects occur. Interactions between fluid pressure and solid deformation influence the transport processes, for example by changing material or hydraulic properties. Shrinkage of the conduit volume

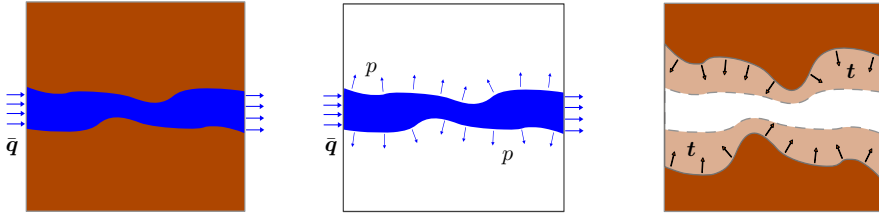


Figure 2.1: Example of a hydro-mechanical problem induced by fluid to solid coupling; (left) flow \bar{q} is prescribed in a fluid domain surrounded by a solid material; (center) the fluid acts on the solid with a pressure p . Pressure variations are induced by transport processes along the fluid conduit; (right) due to pressure variations, the solid material is deformed and counteracts the fluid pressure with the surface stress \mathbf{t} on the boundaries between fluid and solid.

not only triggers fluid flux, but also diminishes the thickness of the conduit, thus affecting its transmissivity.

Coupling depends on the material and geometrical properties of the analyzed problem and on the occurring physical phenomena, which vary in space and time. The relation, for example, between fluid pressure distribution and solid deformation is non-local and non-unique. Deformation at a certain point is not only induced by the pressure applied at that position, but also by pressure values acting along the entire boundary surface. This non-local property of deformation together with the hydro-mechanical coupling characteristic explained above lead to a complex transport behavior along deformable conduits, which shows counterintuitive effects.

Having general examples in mind (Figures 2.1, 2.2), hydro-mechanical coupling can be modeled using different approaches and different coupling schemes. The most simple, local approach to describe a coupled problem is to model the fluid flow by means of the well-known Navier-Stokes equation and characterize the solid phase as a linear elastic material containing discrete conduits. As an alternative, the theory of poro-elasticity [12] can be used to describe the entire domain, containing both fluid and solid, with the same set of equations. Phenomena occurring at the pore scale are homogenized and heterogeneities at the length scale related to a fluid-filled conduit are accounted for varying the porosity of the rock and of the fracture domain.

Each modeling approach has advantages and disadvantages in comparison to other procedures depending on the field of application, cf. Table 2.1. The present work focuses on hydro-mechanical coupling between a solid phase and a high-aspect-ratio fluid conduit, to better model the geometry of real fractures. During the numerical solution procedure of the governing equations, for example with the Finite Element Method, spatial discretization of the narrow domain describing the fracture represents a challenge. For high-aspect-ratio ge-

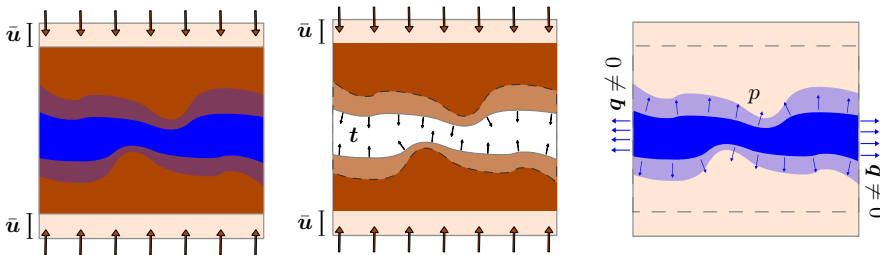


Figure 2.2: Example of a hydro-mechanical problem induced by solid to fluid coupling; (left) the domain containing solid and fluid is deformed with a prescribed displacement $\bar{\mathbf{u}}$; (center) the solid constituent deforms and acts with a surface stress \mathbf{t} on the fluid domain; (right) the fluid domain shrinks and fluid flux $\mathbf{q} \neq 0$ is induced.

ometries, which well approximate real fracture geometries, meshing quality diminishes and discretization is impossible without introducing highly deformed elements. A novel modeling approach is proposed to efficiently account for high-aspect-ratio conduits.

The aim is to derive a coupled set of equations governing pressure transport and solid deformation, respectively. Three approaches are considered that account for hydro-mechanical coupling. First a methodology based on coupling the Navier-Stokes equation and the Lamé-Navier equation is presented. A second approach is based on the well-known poro-elastic theory. A third approach is explicitly derived for high-aspect-ratio inclusions and is referred to as the *hybrid-dimensional* approach.

2.2 Navier-Stokes and Lamé-Navier equations

The following approach represents a straightforward implementation of a problem related to hydro-mechanical coupling. To distinguish between variables characterizing the fluid and the solid constituents, the indexes \mathbf{f} and \mathbf{s} are used, respectively.

The Navier-Stokes equation governs the flow of a compressible viscous fluid (Figure 2.3, left) and reads in general form [7]

$$\begin{aligned} \rho^{\mathbf{f}R} \left(\frac{\partial \mathbf{v}_{\mathbf{f}}}{\partial t} + \mathbf{v}_{\mathbf{f}} \cdot \text{grad } \mathbf{v}_{\mathbf{f}} \right) + \text{grad } p & \quad (2.1) \\ -\eta^{\mathbf{f}R} \text{div} \left(\left(\text{grad } \mathbf{v}_{\mathbf{f}} + \text{grad}^T \mathbf{v}_{\mathbf{f}} \right) - \frac{2}{3} \text{div} (\mathbf{v}_{\mathbf{f}}) \mathbf{I} \right) & = \mathbf{b}, \end{aligned}$$

where $\rho^{\mathbf{f}R}$ is the effective fluid density, $\mathbf{v}_{\mathbf{f}}$ represents the flow velocity, p is the fluid pressure, $\eta^{\mathbf{f}R}$ is the fluid viscosity, \mathbf{I} represents the second order unity

tensor, and \mathbf{b} represents body forces. Equation (2.1) enforces balance of momentum and is complemented by the equation for conservation of mass in its local form, the continuity equation [7]

$$\frac{\partial \rho^{fR}}{\partial t} + \operatorname{div} (\rho^{fR} \mathbf{v}_f) = 0. \quad (2.2)$$

The rock is modeled as a linear elastic material. Deformations \mathbf{u}_s of the solid are described by the Lamé-Navier equation [39]

$$\rho^{sR} \frac{\partial^2 \mathbf{u}_s}{\partial t^2} - (\lambda + \mu) \operatorname{grad} \operatorname{div} \mathbf{u}_s - \mu \operatorname{div} \operatorname{grad} \mathbf{u}_s = \mathbf{b}, \quad (2.3)$$

where ρ^{sR} is the effective density of the solid, λ is the first Lamé parameter, and μ is the second Lamé parameter (or shear modulus). In equations (2.1) and (2.3) the inertia terms, related to the first time derivative of the velocity and the second time derivative of the displacement, respectively, can be neglected for static and quasi-static investigations.

Hydro-mechanics are accounted for when coupling between equations (2.1) and (2.3) is correctly implemented. On the one hand, pressure changes affect the conduit volume by deforming the solid domain. The fluid pressure acting on the boundaries between fluid and solid can be accounted for as a stress boundary condition in the mechanical problem. The stresses applied at the boundaries of the solid domain induce the displacement \mathbf{u}_s . On the other hand, volume changes induced by solid deformation affect the fluid domain. For example, increase or decrease in volume available for the fluid leads to variations in the fluid velocity as well as in fluid density and pressure.

The Navier-Stokes equation does not introduce major assumptions to model the fluid domain, for example regarding the flow profile that develops along the thickness of the conduit. While the absence of major assumptions represents a great advantage in terms of generality of the modeling approach, adopting the Navier-Stokes equation limits its applicability to low-aspect-ratio conduits, cf. Figure 2.4. During the numerical solution procedure, a large amount of elements is needed to discretize the fluid domain along its width. Only a fine discretization correctly captures the developing fluid velocity profile. The requirement of having several elements along the conduit thickness adds complexity to the discretization procedure, which most of the times cannot be successfully performed for high-aspect-ratio geometries. In this thesis, focus is put on thin conduits, where the thickness of the fluid domain is several orders of magnitude smaller than its length. Therefore, this approach will not be further discussed in the following investigations.

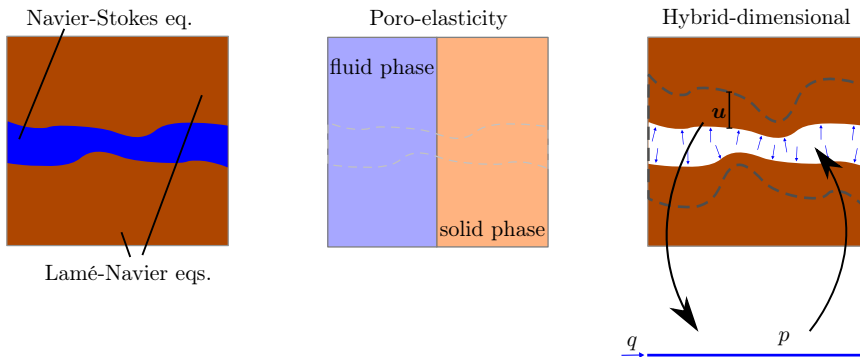


Figure 2.3: Modeling approaches to account for hydro-mechanical coupling: (left) the solid is described as a linear elastic material and the fluid flow is governed by the Navier-Stokes equation; (center) the fluid and solid constituents are accounted for with the poro-elastic equations; (right) in the hybrid-dimensional approach the fluid domain is reduced to a one-dimensional geometry. Fluid flow and solid deformation problems are solved separately. Coupling is achieved by exchange of fluid pressure and solid deformation between the two governing equations.

2.3 Poro-elastic theory

2.3.1 Poro-elastic-based approach

The hydro-mechanical problem induced by interaction between fluid flow and solid deformation can be modeled by the theory of poro-elasticity. The subject was first treated by Terzaghi [92] to describe one-dimensional consolidation, while the theory was generalized to three dimensions by Biot [12]. Later, the topic has been at the attention of several scientific contributions [e.g., 8, 78, 96, 102]. The quasi-static poro-elastic equations describe the fluid flow through a porous medium, solid deformation, and account for the hydro-mechanical coupling between fluid flow and solid matrix.

The poro-elastic theory is based on volume averaging of quantities [e.g., 25, 27, 28, 33]. A porous material with inhomogeneities at the length scale of the average pore size is treated in the poro-elastic equations as a homogeneous material. Description of a porous medium as an homogeneous material is a good approximation if the size of the analyzed domain and the typical length-scale of the physical phenomena are much larger than the average pore size.

A fully-saturated poro-elastic material is characterized by two phases, a solid and a fluid constituent. The solid phase is composed of grains that generate the solid structure. In general, the bulk modulus of the solid frame is much

smaller than the bulk modulus of the grains, $K_d \ll K^s$. Inhomogeneities at a larger scale, as for example fractures or fluid conduits (e.g., Figure 2.1, left) are not explicitly accounted for by the poro-elastic equations. The solid and the fluid domain can both be approximated as porous materials, governed by the same set of equations, with different material properties (Figure 2.3, center). The conduit can be described as a highly porous domain (e.g., 90% porosity), where the surrounding material can be modeled as a porous rock.

The derivation of the poro-elastic equations is based on the assumption that the materials composing the analyzed domain are isotropic and homogeneous. Furthermore, the solid constituent is modeled as a linear elastic material. The partial differential equation governing the mechanics of the solid phase is obtained imposing equilibrium to the porous material and reads

$$-\operatorname{div}(\boldsymbol{\sigma}_E^s - \alpha p \mathbf{I}) = \mathbf{b}, \quad (2.4)$$

where \mathbf{b} represents the body forces and $\boldsymbol{\sigma}_E^s$ is the Cauchy extra stress tensor of the solid phase. The solid displacement field \mathbf{u}_s is then evaluated by means of the linear elastic constitutive equations characterizing the solid phase.

The flow of the fluid constituent is described by Darcy's law, which relates the seepage velocity \mathbf{w}_f , i.e., the relative velocity of the fluid with respect to the solid velocity ($\mathbf{w}_f = \mathbf{v}_f - \mathbf{v}_s$), to the gradient of the fluid pressure p as

$$\mathbf{w}_f = -\frac{k^s}{\eta^{fR}} \operatorname{grad} p, \quad (2.5)$$

where k^s refers to the intrinsic permeability and η^{fR} represents the effective viscosity of the fluid. Equation (2.5), together with a constitutive equation for a barotropic fluid, is inserted into the fluid mass conservation equation to obtain the governing equation [102]

$$\frac{1}{M} \frac{\partial p}{\partial t} - \frac{k^s}{\eta^{fR}} \operatorname{div} \operatorname{grad} p + \alpha \operatorname{div} \left(\frac{\partial \mathbf{u}_s}{\partial t} \right) = 0. \quad (2.6)$$

Equations (2.4) and (2.6) represent the coupled set of governing equations derived in the poro-elastic theory. Equation (2.6) is coupled to (2.4) by the rate of change of the solid displacement \mathbf{u}_s . The Biot-Willis parameter $\alpha = 1 - K_d/K^s$ refers to the ratio of increment of fluid content in relation to changes in bulk volume. Biot's coupling coefficient M represents the storage modulus at a material point, i.e., the amount of fluid that must be added or removed in order to obtain a certain pressure variation. In equation (2.6), the inverse of M is $1/M = \phi/K^f + (\alpha - \phi)/K^s$. Specific storage capacity $1/M$ at a material point is related to the porosity ϕ , to the bulk modulus of the fluid K^f , as well as to the bulk modulus of the grains.

Investigation of porous fractured rock intrinsically introduces different scales at which physical processes take place. On the one hand, flow through a homogeneous porous material is related to the size of its pores. On the other

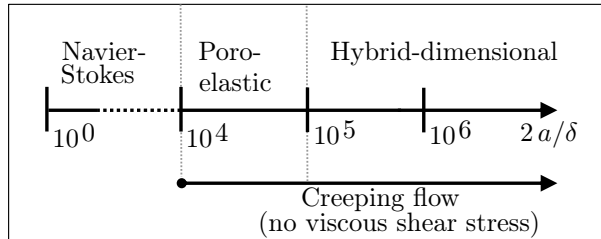


Figure 2.4: Feasibility of modeling approaches depending on the aspect ratio ($2a/\delta$) of the analyzed fracture. The hybrid-dimensional approach is derived to account for hydro-mechanical problems related to high-aspect-ratio fluid inclusions.

hand, fractures control fluid transport phenomena at characteristic lengths much larger than the pore size. In fractured domains, fluid conduits represent a preferential path for pressure transport and, therefore, their length often controls the range at which transport phenomena occur. Typically, the length of inclusions analyzed in reservoir engineering applications is $2a \sim 10^{-2} \dots 10^3$ m. Specific storage capacity is related to each material point and storage deriving from deformation of the fracture surfaces is not accounted for. To avoid such limitation, the coupling term $\alpha \operatorname{div}(\partial \mathbf{u}_s / \partial t)$ in equation (2.6) can be modified, in the fluid domain only, to account for deformations of the fracture surface instead of the solid deformations at each material point. In this investigation, the poro-elastic approach represents an alternative to the approach presented in the former section that is more feasible to analyze thin inclusions, because the set of governing equations are specifically derived to account for hydro-mechanical coupling. In addition, the poro-elastic equations can account for fluid mass exchange between the fracture domain and the surrounding porous rock, i.e., leak-off.

As for the former approach, the complexity of the fluid domain discretization procedure restricts the application of the poro-elastic approach in terms of aspect ratio of the analyzed conduits. Nevertheless, because the velocity profile is assumed, cf. Eq. (2.5), less elements are needed to discretize the fracture domain along its width. Therefore, with the poro-elastic approach higher-aspect-ratio geometries can be analyzed in comparison to the former approach, cf. Figure 2.4.

2.3.2 Diffusion-based approach

To obtain a simple diffusion equation one can rely on the well-known theory of poro-elasticity. A diffusion-based approach relies on the assumption that for some combinations of material parameters or applied boundary conditions the equation governing the fluid flow can be decoupled from the mechanical problem describing the surrounding rock. For the poro-elastic equations (2.4) and (2.6), decoupling occurs when the coupling term $\alpha \operatorname{div} \partial \mathbf{u}_s / \partial t$ in equation (2.6) vanishes, i.e., when the bulk volume of the analyzed domain remains constant or when $\alpha \rightarrow 0$. Furthermore, it has been shown [76] that if the poro-elastic equations (2.4) and (2.6) are reformulated in terms of mean stress $\sigma^m = \operatorname{tr} \mathbf{T}$ and fluid pressure p , where \mathbf{T} is the total stress, decoupling occurs for conditions of constant mean stress σ^m . In either case, equation (2.6) degenerates to a linear diffusion equation

$$\frac{1}{M} \frac{\partial p}{\partial t} - \frac{k^s}{\eta^f R} \operatorname{div} \operatorname{grad} p = 0. \quad (2.7)$$

The difference lies in the exact formulation of the storage modulus M . Due to the focus on high-aspect-ratio geometries intersecting the source at a normal angle, it is reasonable to assume that the flow mainly occurs in radial direction. Therefore, the radial component of equation (2.7)

$$\frac{1}{M} \frac{\partial p}{\partial t} - \frac{k^s}{\eta^f R} \left(\frac{\partial^2 p}{\partial r^2} + \frac{1}{r} \frac{\partial p}{\partial r} \right) = 0. \quad (2.8)$$

is analyzed. For this formulation the specific storage capacity $s_F = 1/M = \phi/K^f + (\alpha - \phi)/K^s$ is related to the fluid stiffness, as well as to the grain stiffness at each material point.

Linear diffusion equations are widely used to model pressure transport along fractures. One can rely on equation (2.8) and “simplistically” replace the local material and storage properties by bulk fracture properties. The diffusion equation governing fluid flow along a fracture then reads

$$\frac{\partial p}{\partial t} - D_F \frac{\partial^2 p}{\partial r^2} - \frac{D_F}{r} \frac{\partial p}{\partial r} = 0, \quad (2.9)$$

where the hydraulic diffusivity of the fracture $D_F = \delta_0 k / S_F \eta^f R$ is related to fracture permeability k , to the bulk fracture storage capacity S_F , and to the fracture aperture δ_0 , which is constant in time. For planar conduits the bulk storage capacity has two contributions [65, 66, 76]

$$S_F = \delta \beta_f + \frac{\partial \delta}{\partial p}, \quad (2.10)$$

where the first term is related to the fluid compressibility β_f and the second to the contribution from changes in fracture aperture δ caused by pressure variations. The fracture permeability $k = \delta^2/12$ is obtained by assuming a Poiseuille type of flow in the fracture, related to the aperture δ . Pressure dependence of storage capacity as well as fracture permeability are linked to deformation caused by pressure diffusion along the fracture. The contribution due to aperture changes is expressed by parametrization of the bulk storage capacity $S_F = \alpha_s \delta_0 \beta_f$ in multiples of the fluid compressibility. Equation (2.9) is reformulated as

$$\alpha_s \beta_f \frac{\partial p}{\partial t} - \frac{\delta_0^2}{12 \eta^f R} \frac{\partial^2 p}{\partial r^2} - \frac{\delta_0^2}{12 r \eta^f R} \frac{\partial p}{\partial r} = 0. \quad (2.11)$$

In the diffusion-based approach a single macroscopic value of S_F characterizes the storage properties of the fracture. The computational complexity is reduced in comparison to the approach above, as only a one-dimensional domain representing the fracture is modeled. Nevertheless, the derivation of equation (2.11) relies on a series of assumptions that constrain the applicability of the approach. Equation (2.11) is used for homogeneous materials where material parameters do not depend on pressure. Furthermore, storage related to local deformations of the fracture surface is not accounted for at each position r along the fracture, it is rather addressed by a bulk storage capacity characterizing the entire fracture domain.

2.4 Hybrid-dimensional approach

The hybrid-dimensional approach is a method derived to efficiently account for coupled problems related to high-aspect-ratio fluid conduits. Accounting for a two-dimensional domain, for example, the description of the fluid volume is reduced to a one-dimensional domain, cf. Figure 2.3 (right). Investigations involving a one-dimensional geometry allow for an efficient numerical solution procedure and avoid issues deriving from the discretization of narrow two-dimensional geometries.

For illustration, a three-dimensional solid domain with a horizontal fluid inclusion is analyzed, where axial symmetry is exploited (Figure 2.5). In the hybrid-dimensional approach, solid and fluid domains are modeled separately. The partial differential equation governing the fluid flow along a deformable inclusion is obtained enforcing balance of mass and balance of momentum on the fluid volume, while the solid constituent can be modeled by means of linear elasticity. Different coupled set of equations can be derived from basic conservation laws for specific heterogeneities. In this example, the geometry is naturally written in cylindrical coordinates (Figure 2.5). The solid domain is modeled as two-dimensional axisymmetric and the fluid is modeled in a one-dimensional axisymmetric domain. Following, the equation governing the fluid flow is derived.

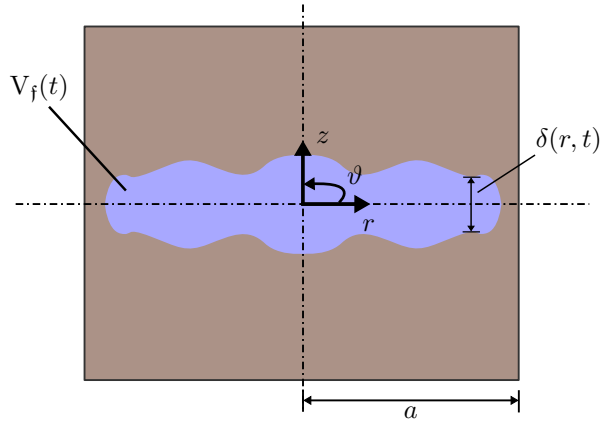


Figure 2.5: Generic fracture geometry written in cylindrical coordinates. Geometrical parameters used in the hydro-mechanical approach: the aspect ratio $2a/\delta$ of the conduit is related to the ratio of the fracture half-length a and the aperture δ . Aperture $\delta(r, t)$ varies in space and time. The fracture volume $V_f(t)$ changes in time due to hydro-mechanical coupling.

2.4.1 Conservation of fluid mass

The general form of mass conservation is satisfied in a fully-saturated conduit when the material time derivative

$$\frac{D}{Dt} \int_V dm^f = \frac{D}{Dt} \int_V \rho^{fR} dv = 0, \quad (2.12)$$

for every arbitrary fluid volume V in the fracture domain $V_f(t)$, that changes in time due to deformation (cf. Figure 2.5). The integral over the volume V is reformulated as a triple integral in the three cylindrical coordinates

$$\frac{D}{Dt} \int \int \int \rho^{fR} r dz d\phi dr = 0. \quad (2.13)$$

The hybrid-dimensional approach is developed to efficiently model fluid inclusions with high aspect ratio $2a/\delta$ between half-length a and aperture or width δ of the conduit. In high-aspect-ratio inclusions it is reasonable to assume that fluid flow mainly occurs in radial direction. The fluid density is assumed constant over the fracture height. Furthermore, the axial symmetry of the problem is exploited, thus equation (2.13) can be replaced by the line integral

$$\frac{D}{Dt} \int 2\pi \rho^{fR} \delta(r, t) r dr = 0. \quad (2.14)$$

The aperture $\delta(r, t)$ represents the aperture of the fracture normal to the radial direction and varies with the position along the fracture and with time. The

simplified one-dimensional integral (2.14) holds for every arbitrary interval dr along the fracture domain.

To solve equation (2.14), the integral is transformed to the undeformed configuration. This way, the integral is solved over a constant domain. The Jacobi transformation [45] is used to transform between the deformed and undeformed configuration. The Jacobian reads

$$J = \frac{l}{l_0} = \frac{\partial r}{\partial R}, \quad (2.15)$$

where l is a length and r is the position vector, both in the deformed configuration. Conversely, l_0 and R represent a length and the position vector in the undeformed configuration, respectively. It follows that

$$dr = J dR \quad \text{and} \quad \dot{J} = J \frac{\partial v_{fr}}{\partial r}, \quad (2.16)$$

where v_{fr} is the fluid velocity in radial direction.

Using Reynolds' transport theorem [45] in equation (2.14), the time-dependent domain of integration is transformed to the reference configuration. The material time derivative is computed and transformed back to the current configuration to give

$$2\pi \int \left[\left(\frac{D\rho^{fR}}{Dt} \delta + \rho^{fR} \frac{D\delta}{Dt} \right) r \right] dr + 2\pi \int \left[\rho^{fR} \delta \frac{Dr}{Dt} + \rho^{fR} \delta \frac{\partial v_{fr}}{\partial r} r \right] dr = 0. \quad (2.17)$$

According to the localization theorem [38], mass balance is locally satisfied when the integrand of equation (2.17) vanishes. Therefore, the local form of fluid mass balance in a high-aspect-ratio inclusion is obtained as

$$\left(\frac{D\rho^{fR}}{Dt} \delta + \rho^{fR} \frac{D\delta}{Dt} \right) r + \rho^{fR} \delta v_{fr} + \rho^{fR} \delta \frac{\partial v_{fr}}{\partial r} r = 0. \quad (2.18)$$

The velocity of the solid phase in radial direction is assumed to be negligible compared to the radial fluid velocity ($v_{sr} \ll v_{fr}$), thus the relative velocity of the fluid becomes $w_{fr} \rightarrow v_{fr}$. Using this approximation in equation (2.18) and writing out the material time derivatives, the condition for mass conservation in a deformable fracture filled with a compressible fluid is obtained:

$$\frac{\partial}{\partial t} (\rho^{fR} \delta) + \frac{\partial}{\partial r} (w_{fr} \rho^{fR} \delta) + \frac{w_{fr} \rho^{fR} \delta}{r} = 0. \quad (2.19)$$

The obtained equation enforces mass balance for the fluid domain, which means that for any change in fluid volume, fluid density and velocity are affected accordingly. Vice versa, for any variation in fluid velocity or density, the fluid volume is affected to ensure fluid mass conservation.

2.4.2 Balance of momentum

The balance of momentum for the fluid is evaluated assuming a Poiseuille-type of flow. Again, assuming that the fracture is characterized by a high aspect ratio and that the conduit's boundaries have small curvatures, the flow is approximated by that occurring between two parallel plates. Furthermore, the half-length a of the fluid inclusion has to be chosen large enough to avoid dominant effects of the fracture tip, cf. Figure 2.5.

The horizontal component of the fluid flow is driven by the pressure difference Δp in radial direction. Pressure gradients in the fluid domain can be triggered by the application of a fluid flux (e.g., Figure 2.1) or can be induced by fracture deformation (e.g., Figure 2.2). A small interval Δr of the fracture domain is analyzed, in which the aperture $\bar{\delta}$ is assumed constant. The equation for the velocity distribution in this interval along the fracture aperture reads [61]

$$w_{fr}(z) = -\frac{\bar{\delta}^2}{2\eta^{fR}} \frac{\Delta p}{\Delta r} \left[1 - \frac{z}{\bar{\delta}}\right] \frac{z}{\bar{\delta}}, \quad (2.20)$$

a parabolic velocity distribution of the fluid along the vertical direction z .

The fluid flow in the fracture is modeled as a one-dimensional axisymmetric process. The mean flow velocity is obtained integrating the velocity profile over the thickness. For infinitely small intervals with constant aperture the radial distribution of fluid velocity in the fracture becomes

$$w_{fr} = -\frac{\bar{\delta}^2}{12\eta^{fR}} \frac{\Delta p}{\Delta r} \approx -\frac{\delta^2(r,t)}{12\eta^{fR}} \frac{\partial p}{\partial r}, \quad (2.21)$$

i.e., a locally applicable Darcy's law. The permeability of the fracture is a result of the parallel plate approximation and depends on the fracture aperture δ at each point.

2.4.3 Equation governing fluid flow

The derived set of equations governing the fluid flow in the fracture domain comprises equation (2.19) and equation (2.21). In the hybrid-dimensional approach, the equation governing the fluid flow refers to a one-dimensional axisymmetric domain and is based on two principles: a) fluid mass conservation and b) conservation of fluid momentum. The latter is obtained introducing the assumption of fluid flow between parallel plates. Balance of mass and momentum are combined by inserting equation (2.21) in equation (2.19), which leads to

$$\frac{\partial (\rho^{fR} \delta)}{\partial t} - \frac{1}{r} \frac{\partial}{\partial r} \left[\frac{\delta^3 \rho^{fR} r}{12\eta^{fR}} \frac{\partial p}{\partial r} \right] = 0. \quad (2.22)$$

The fluid compressibility is introduced as

$$\beta_f = \frac{1}{\rho^{fR}} \frac{\partial \rho^{fR}}{\partial p}. \quad (2.23)$$

Equation (2.22) is rearranged in the form of a prototype one-dimensional convection-diffusion equation assuming constant viscosity

$$\begin{aligned} \frac{\partial p}{\partial t} + \frac{1}{12 \eta^{fR} r} \frac{\partial}{\partial r} \left(-\frac{r \delta^2}{\beta_f} \frac{\partial p}{\partial r} \right) - \frac{1}{12 \eta^{fR}} \left(\frac{\delta}{\beta_f} \frac{\partial \delta}{\partial r} \right) \frac{\partial p}{\partial r} \\ - \frac{\delta^2}{12 \eta^{fR}} \left(\frac{\partial p}{\partial r} \right)^2 = -\frac{1}{\beta_f \delta} \frac{\partial \delta}{\partial t}, \end{aligned} \quad (2.24)$$

consisting of a time-dependent term, a diffusion term, a convection term, an additional quadratic term, and a term at the right-hand side related to the fracture deformation velocity.

In case that fluid is injected in the fracture, the initial-boundary-value problem is obtained by complementing equation (2.24) with appropriate initial and boundary conditions

$$w_{fr}(r=0, t) = \bar{w} \quad 0 < t \leq t_{\text{end}}, \quad (2.25)$$

$$w_{fr}(a, t) = 0 \quad 0 < t \leq t_{\text{end}}, \quad (2.26)$$

where \bar{w} is a prescribed flux per unit area at the radius $r = 0$. Note that in equation (2.25) the flow velocity w_{fr} can be triggered imposing a boundary condition \bar{w} as well as imposing a pressure boundary condition \bar{p} . The set of equations defining the initial-boundary-value problem is closed with the initial conditions

$$p(r, t_0) = p_0 \quad 0 < r < a, \quad (2.27)$$

$$\delta(r=0, t_0) = \delta_0(r_w), \quad (2.28)$$

where p_0 and $\delta_0(r_w)$ are the initial pressure and aperture at equilibrium, respectively.

2.4.4 Solid deformation

To solve equation (2.24), the aperture values $\delta(r, t)$ along the fluid domain have to be updated according to the solid deformation caused by pressure transport. During numerical solution procedure, pressure solutions $p(r, t)$ from equation (2.24) are applied to the fracture surface in the model of the rock domain as a surface stress boundary condition, e.g., Figure 2.1 (center), (right). The displacements evaluated from the solution of the mechanical problem are added to the aperture δ in equation (2.24) for each iteration in time.

The mechanical part of the domain can be modeled using different approaches. The Lamé-Navier equation (2.3) can be used to model the solid domain and to obtain the deformation of the solid. As an alternative, analytical or semi-analytical solutions of solid deformation in a pressurized cavity can be used. Solutions to pressurized conduits with constant pressure [94] as well as with arbitrary pressure distributions [62, 89] allow for an efficient evaluation of the solid deformation.

2.4.5 Hydro-mechanical coupling with leak-off

In case that the rock domain is modeled as a porous material, in addition to solid deformation, hydro-mechanical coupling can include fluid mass exchange between the fluid and the porous domain, in short, leak-off. Mass exchange can be accounted for adding a source term q_L to the right hand side of equation (2.24).

Leak-off is a flux starting from the conduit and flowing into the surrounding porous domain. For simplicity, a fluid conduit with constant aperture $\delta(r)$ is analyzed (cf. Figure 2.6). The seepage velocity w_{fN} induced by leak-off, orthogonal to the fracture surface, is governed by Darcy's law formulated within the poro-elastic domain as

$$w_{fN}(r) = -\frac{k^s}{\eta_{fR}} \text{grad } p_{\text{rock}} \cdot \mathbf{n}, \quad (2.29)$$

at each position r along the fracture. In equation (2.29), p_{rock} refers to the pressure in the porous matrix, k^s is the intrinsic permeability of the surrounding material, and \mathbf{n} is the vector normal to the fracture surface, which has a positive sign when pointing outside the fracture domain. The source term q_L is evaluated from the seepage velocity as

$$q_L = \frac{w_{fN}}{\delta \beta_f}. \quad (2.30)$$

To obtain the seepage velocity and, therefore, the source term, the pressure gradient in the surrounding material can be evaluated by means of a semi-analytical solution of a diffusion equation [21] or numerically, if the surrounding domain is modeled as poro-elastic material. While a numerical evaluation of q_L requires the poro-elastic equations (2.4) and (2.6) to describe the surrounding porous rock, an analytical solution can be easily added to equation (2.24), independent of the modeling approach used for the solid domain. Analytical evaluation of leak-off is particularly interesting if used in combination with a semi-analytical solution to evaluate the rock deformation. The resulting hydro-mechanical coupled model relies on numerical treatment of the fluid domain only, while solid deformation and leak-off are efficiently evaluated analytically.

To analytically derive the source term q_L , one can assume that fluid infiltrates the porous rock at each position r as a one-dimensional diffusion phenomenon, orthogonal to the fracture surface (Figure 2.6). Exploiting vertical

2.5 Summary

To account for hydro-mechanical coupling between fluid flow and solid deformation, three approaches were presented. Each approach has its advantages and disadvantages (Table 2.1), related to the complexity of the method or to the specific field of application. An approach based on the Navier-Stokes equation (2.1) and the Lamé-Navier equation (2.3) represents the most direct way to describe a coupled problem. This approach is however not used in this thesis, due to the limitations related to the aspect ratio of the analyzed geometries. The poro-elastic approach shares the same limitations as the former approach, but limited to a lesser degree. Therefore, with the poro-elastic approach one can successfully account for geometries with higher aspect ratios than with the first approach. In the following chapters, the poro-elastic approach is used as a benchmark for the numerical results obtained with the hybrid-dimensional approach. With the latter methodology, initial-boundary-value problems are solved, independent of the aspect ratio of the analyzed fractures.

Table 2.1: Comparison of modeling approaches to capture hydro-mechanical coupling, e.g., for a three-dimensional problem where axial symmetry can be exploited.

Model	Navier-Stokes + Lamé-Navier	Poro-elastic theory	Hybrid-dimensional approach
Domain modeling	2-D axisymm.	2-D axisymm.	2-D axisymm. (solid) + 1-D axisymm. (flow)
Assumptions	Viscous fluid	Viscous fluid + Poiseuille-flow	1-D flow + Viscous fluid + Poiseuille-flow
Application	Low aspect ratio	Low aspect ratio	Independent of aspect ratio
Physical effects	No leak-off	Leak-off included	Leak-off can be included
Numerical effort	Computationally expensive	Computationally expensive	Efficient computation

Chapter 3

Numerical modeling of the hydro-mechanics of fractures

3.1 Introduction

Subsurface fluid flow is crucial for matter and heat transport in the earth but also for provision of liquid resources and temporary or permanent underground storage of fluids. For many years, the physical properties relevant for fluid flow have been determined from pumping experiments in wells and deep boreholes penetrating fluid reservoirs. Diffusion equations have proven very valuable in the analyses of these tests [e.g., 17, 46, 57]. Yet, some field observations cannot be explained even by employing extended forms of diffusion equations. For example, inverse water-level fluctuations in the vicinity of pumped aquifers (known as Noordbergum effect) have been documented [e.g., 9, 47, 51, 79]. This phenomenon is related to hydro-mechanical coupling, the interplay between temporal and spatial changes of fluid pressure and bulk stress or deformation in porous media.

Hydro-mechanical coupling is also evidenced by observations of natural processes at the earth's surface or at shallow depth. The outpouring of warm water along fault traces has been reported following earthquakes [e.g., 86]. Continuous monitoring of wells revealed a systematic correlation of level changes with seismic activity [15, 80] or with barometric loading of the fluid column [81], for example. Seismicity is believed to be triggered by pore-fluid-pressure changes related to natural precipitation [e.g., 43] but also by anthropological surface activities such as charging surface reservoirs [e.g., 24, 87] or injection of fluid into the underground [e.g., 56, 106].

In approaches resting on diffusion equations the coupling of deformation and fluid pressure is only accounted for by employing storage parameters, e.g., specific storage capacity, representing the property of a material point and as such closely related to the concept of representative volume elements (RVE).

The constitutive poro-elastic behavior of a material point is assumed to be correctly described by combinations of compressibilities of the pore space, the solid constituents, and the fluid appropriately weighted using porosity. Yet, the deformation of structures on length scales exceeding the size of RVE (e.g., hydraulic conduits such as joints and fractures) associated with changes in fluid pressure is not accounted for in conventional analyses based on diffusion equations.

Previously, various extensions of diffusion equations have been proposed accounting for non-constant but pressure-dependent hydraulic properties [e.g., 65, 67, 85, 104]. Yet, it remains questionable to which extent the non-local character of joint and fault deformation associated with pressure transients is appropriately reflected by these approaches.

In their seminal work, Rice & Cleary [78] derived a relation between spatial and time derivatives of strain and pore pressure for an isotropic material from a continuum mechanics perspective. When considering individual fluid conduits, e.g., joints and fractures or faults, their geometric features become central for the hydro-mechanical response [e.g., 62]. In particular, the pressure and stress-sensitive aperture of joints controls their stiffness and transmissivity [e.g., 5, 6] thus constituting the key element of the coupling.

The physical processes involved in fluid flow in deformable conduits are modeled and investigated to understand the importance of the coupling between fluid flow and rock deformation. Rather than analyzing the stress-permeability coupling by changing the far-field stresses [e.g., 69, 101], the hydro-mechanical behavior of fractures is investigated where the fluid flow is the deformation-driving phenomenon. Fracture propagation is not taken into account but only elastic deformation of the fracture is considered.

Modeling equations are derived relying on physically-motivated relations that avoid decoupling approximations, frequently used for analyses based on diffusion equations. Specifically, the coupled nature of the problem is addressed with two conceptually and technically differing approaches. The first modeling approach rests upon the well-established quasi-static poro-elastic theory [12]. In this framework, the derivation of the governing equations is straight forward, yet, the numerical solution procedure introduces technical difficulties related to discretization. The large aspect ratio of fractures causes the numerical models to have an extremely large number of degrees of freedom leading to computationally expensive solution procedures. To overcome this drawback, an alternative modeling procedure is developed, here addressed as *hybrid-dimensional approach*, with the aim to model fractures with realistic aspect ratios at reduced computational effort.

The objective of this study is to develop and test efficient numerical methods for the hydro-mechanical modeling of fractured materials. Observations that can be unanimously linked to the coupling between fluid flow in and deformation of hydraulic conduits, i.e., hydro-mechanical coupling, constitute an important element of this undertaking. The Noordbergum effect and inverse-pressure response (see recent papers by Murdoch & Germanovich [63] and by

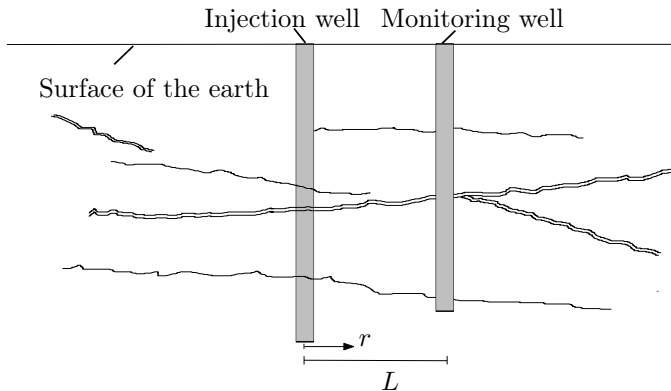


Figure 3.1: Experimental setup: injection borehole ($r = 0$) and monitoring borehole ($r = L$), intersecting fractured rock. The grey areas represent the boreholes.

Slack et al. [88]) are considered to constitute such critical observations and employ observations of the inverse-response during pumping tests in a jointed aquifer in the testing of the developed numerical schemes.

After providing background information, the two approaches are first outlined in detail and then the alternative formulations and their numerical solution procedures are investigated and compared. A dimensional analysis of the governing equation confirms that more processes than just diffusion take place during pumping operations, in particular along conduits characterized by high aspect ratios. The hybrid-dimensional approach is finally used to model critical observations from pumping tests that cannot be addressed by pressure diffusion alone.

3.2 Background and modeling approaches

3.2.1 Critical observations

Hydro-mechanical coupling is documented by a range of critical observations, such as the Noordbergum effect on field scale or the Mandel-Cryer effect on sample scale, that are often associated with counterintuitive fluid-pressure variations [e.g., 97]. One such critical observation was encountered during pumping operations involving an injection borehole and a monitoring borehole, both penetrating a jointed aquifer (Figure 3.1, for well configuration of the field experiment see Renner & Messar [75]). An inverse response in monitoring pressure was observed upon every change in boundary condition in the injection well [see also 88]. Just after injection was started, a sudden pressure drop was measured in the monitoring borehole, before the pressure started to increase due to

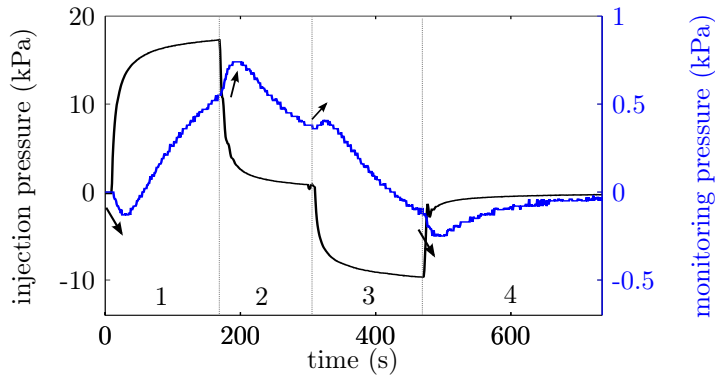


Figure 3.2: Experimental pressure transients recorded in injection (black line) and monitoring (blue line) boreholes during a sequence of 1) injection ($t \sim 20 - 170$ s), 2) pause ($t \sim 170 - 300$ s), 3) production ($t \sim 300 - 430$ s), and 4) pause ($t \sim 430 - 700$ s) of pumping. Arrows indicate the direction of inverse response to pumping.

pressure diffusion (Figure 3.2). Quasi-instantaneous pressure variations were also observed when pumping was stopped or just after production was started. This inverse response is clearly related to some physical mechanism other than diffusion. These critical observations are used to test the modeling approaches detailed in the following.

3.2.2 Basic concepts

Fracture geometry and deformation

The interpretation of field data recorded during fluid injection or production is crucial for unraveling and understanding the conduit structure in the rock surrounding a borehole. However, a model-free analysis of recorded pressure transients is not possible. In contrast, basic characteristics of conduits, e.g., type, number, and orientation, typically have to be specified a priori and can only be aimed for quantitatively constraining details of their properties. As a consequence, the configuration and number of existing hydraulically active fractures cannot be exactly retrieved from pressure-transient analyses but only equivalent systems can be identified (Figure 3.1). In the light of this ambiguity, a simple system is considered consisting of a single horizontal fracture since the main purpose of this study is to investigate basic effects. Furthermore, it is assumed that the injection well intersects the circular fracture in its center. Monitoring wells are assumed to be located at some distance from the fracture tip such that the flow field remains unaffected by end-effects.

An ellipsoidal geometry is prescribed to the model conduit expressed by an aperture δ and a radius a (please note the list regarding notation at the end of the paper), a geometry naturally written in cylindrical coordinates (Figure 3.3). The aperture is conceived as an effective hydraulic aperture that does not imply a specific mechanical state of the real fracture to be modeled. Mechanically open fractures (i.e., non-touching fracture surfaces) require a fluid pressure distribution along them capable of overcoming the normal stress on the fracture surfaces (for constant fluid pressure along the fracture, fluid pressure simply has to exceed normal stress). Yet, it has been long known that fractures maintain a finite hydraulic conductivity well below closure pressure [e.g., 40, 103]. This state may be addressed as hydraulically open but mechanically closed. Flow along the fracture remains well approximated by the cubic law -exactly valid for parallel plates- even when mechanical closure is reached [103]. The Poiseuille-type velocity distribution normal to the fluid flow, characteristic for flow between parallel plates, is well approximated by an effective permeability of $\delta^2/12$. Indeed, the cubic law is applicable to rough surfaces in contact when appropriately modifying the geometrical factor of $1/12$ using measures of fracture roughness [77]. The choice of an ellipsoidal shape is therefore simply intended to provide an analytical description of the corresponding effective hydraulic aperture that specifically avoids singularities due to vertices. Alternatives, such as linearly tapered fracture geometry or parallel fracture surfaces terminated by a circular cap, could equally well be used in principle.

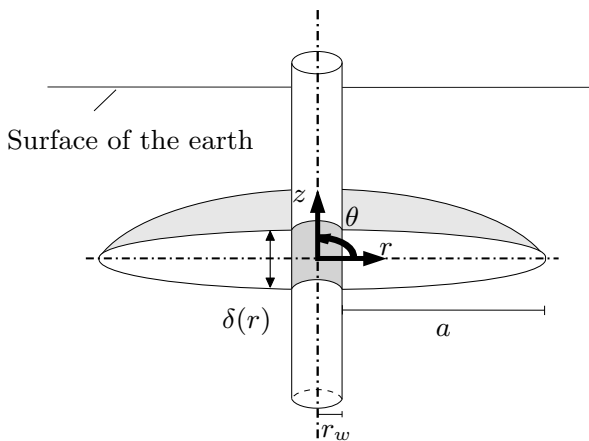


Figure 3.3: Borehole intersecting a single horizontal fracture modeled by elliptical geometry.

Since the aperture associated with the model fracture is perceived to represent an effective hydraulic aperture maintained by contact of local asperities on the fracture surfaces rather than a real continuous opening, bulk stresses on the conduit are also not explicitly modeled or tracked. In the numerical

models, mechanical equilibrium is guaranteed by restricting the displacements on some of the boundaries of the model space (Figures 3.4, 3.5). Stresses are a consequence of these restrictions but are not quantitatively evaluated here. Local stresses on the fracture surfaces are not an explicit feature of the modeling but the prescribed initial aperture with the specific value $\delta(r_w, t_0)$ at the intersection with the borehole ($r = r_w$, where $r_w \ll a$) is considered to result from an unspecified current global stress state. Fluid pressures along the fracture encountered during the modeling remain below about 100 kPa, i.e., on an order of magnitude that is small compared to typical stresses of most but the shallowest depths of investigation.

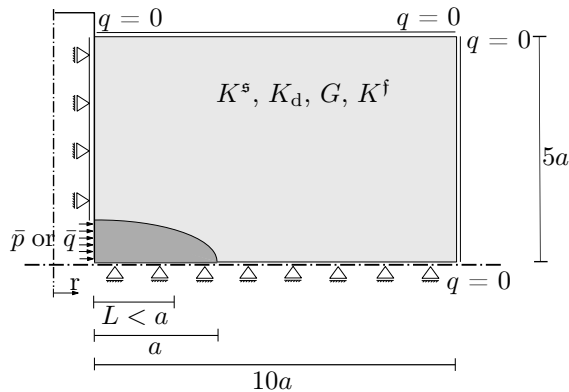


Figure 3.4: Boundary value problem solved with the poro-elastic approach. Pressure is monitored at the injection borehole ($r = r_w$) and at a monitoring borehole ($r = L < a$).

Furthermore, in this study the focus is put on long and thin features as typically encountered in geoscience applications where conduits exhibit apertures of well below a few millimeters and lengths in the range of several meters to tens of meters. Thus, it is assumed that $\delta \ll a$, that fluid flows mainly in radial direction in the conduit, and that the effect of changes in conduit length on fluid flow are negligible compared to those of changes in width. Obviously, horizontal displacements become crucial when investigating propagating fractures.

While ample experimental evidence suggests that the hydraulic conductivity (or permeability) of real fractures is well approximated by the cubic law, the storage properties of fractures are fairly complex and in fact their non-local character causes the hydro-mechanical coupling, the very subject of this study. A hydraulic conduit in a deformable material exhibits a sensitivity to the changes in the stress state of the surrounding material frequently addressed by normal and tangential stiffness that quantify the changes in aperture with changing stress state. Normal stiffness (or storage) is closely related to the stress or pressure dependence of transmissivity [e.g., 64]. Conversely, changes

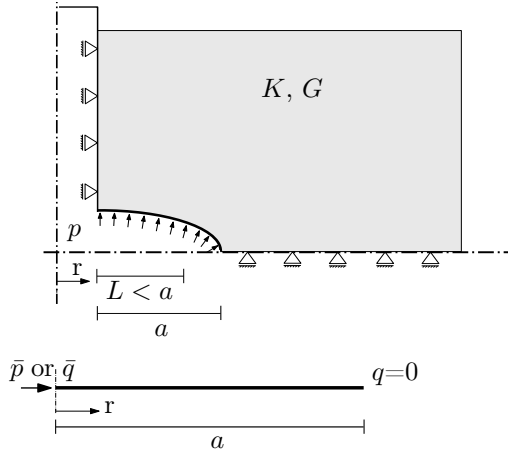


Figure 3.5: Boundary value problem solved with the hybrid-dimensional approach. Pressure is monitored at the injection borehole ($r = r_w$) and at a monitoring borehole ($r = L < a$).

in conduit volume may also be caused by the fluid pressure distribution in it, a relation giving rise to a contribution to storage capacity beyond the compressibility of the fluid. The presented modeling approach does not intend to belittle the role of asperities and surface roughness per se, but approximating the hydraulic conduit's mechanical behavior by that of an elliptical fracture with an effective aperture that gives the “right” conductivity (whichever way this effective aperture had to be determined for a real fracture) provides a simple means of investigating the effect of the bulk deformability of the conduit on fluid flow. The sensitivity of the hydro-mechanical behavior to the exact shape and the characteristics of contacts will have to be subject of further work (but see recent paper by Murdoch & Germanovich [63] and Slack et al. [88]).

Here, pressure p is evaluated relative to an unspecified initial state p_0 before injection. The pressure gradient imposed by injection drives the fluid flow along the fracture. The transient pressure acting on the fracture surface deforms the neighboring rock. The change in fracture geometry alters the permeability of the fracture in turn affecting the distribution of the pressure $p(r, t)$. In general, an increase in pressure causes dilatation of the fracture, thus increasing the effective permeability and contributing to the conduit storage capacity.

The solution of the elastic problem of an internally pressurized elongated cavity [e.g., 89] reveals a non-local and non-unique relation between pressure and deformation adding complexity to the solution procedure [e.g., 29]. The displacement of the fracture surface at any point does not just depend on the pressure applied to that point of the surface, but also on the pressure distribution along the entire fracture surface. Conversely, a pressure load on a point of the surface causes the deformation of the entire structure (Figure 3.6). Due

to the non-local character of deformation, the storage capacity of the fracture cannot be quantified by a single material parameter in the modeling equations but it is rather the result of the hydro-mechanical coupling between the fluid flow and the rock deformation. At a single material point in the fracture domain, specific storage capacity is represented by the fluid compressibility alone in the hybrid-dimensional approach and by conventional expressions involving in addition frame modulus and grain modulus in the poro-elastic approach.

Fluid flow

The hydraulic part of the coupled problem consists of the flow of a compressible (isothermal compressibility $\beta_f = 1/K^f$, where K^f is the bulk modulus of the fluid), viscous (dynamic viscosity η^{fR}) fluid along the fracture domain (here the notation for theory of mixtures as given by Ehlers & Bluhm [33] is followed). The large aspect ratio of fractures causes the fluid to predominantly flow in radial direction. A Poiseuille-type velocity distribution [e.g., 61] is assumed for hydraulically transmissive fractures with low contact area. Integration of such a parabolic velocity profile along the aperture yields the radial component of the (relative) fluid velocity

$$w_{fr} = -\frac{\delta^2(r, t)}{12\eta^{fR}} \frac{\partial p}{\partial r}. \quad (3.1)$$

The proportionality factor of $1/12$ in equation (3.1) reflects the parallel plate approximation and can be altered to account for rough and closed fractures [e.g., 77]. The simplification to a flow between two parallel plates is applied for each position r of the fracture domain leading to a local permeability of

$$k(r, t) = \frac{\delta^2(r, t)}{12}, \quad (3.2)$$

a reasonable assumption considering the large extension of the fracture in the horizontal plane as well as its high aspect ratio (see Section 2.4.2 for a detailed derivation). Due to the quadratic dependence on aperture, permeability k , as a local property of the fracture, is strongly sensitive to deformation.

3.2.3 Poro-elastic approach

In the first approach, the well-established theory of linear poro-elasticity [12] is used. The quasi-static poro-elastic equations describe fluid flow in porous materials, deformation of the solid phase, and account for the coupling between the hydraulic and the mechanical problem. The ellipsoidal fracture domain and the surrounding matrix are modeled as two different homogeneous and isotropic porous materials, each obeying the following set of partial differential equations with different material parameters

$$\begin{aligned}
-\operatorname{div}(\boldsymbol{\sigma}_E^s - \alpha p \mathbf{I}) &= \mathbf{b} \quad \text{and} \quad (3.3) \\
\frac{1}{M} \frac{\partial p}{\partial t} - \frac{1}{\eta^f R} \operatorname{div}(k^s \operatorname{grad} p) + \alpha \operatorname{div}\left(\frac{\partial \mathbf{u}_s}{\partial t}\right) &= 0. \quad (3.4)
\end{aligned}$$

The sets of equations in the different domains are coupled on the interface, i.e., the fracture surface, by continuity conditions for displacement and flux. These are enforced during the numerical solution procedure with the commercial Finite Element (FE) solver Comsol Multiphysics 4.3 (www.comsol.com). A slight modification is introduced in equation (3.4) with respect to the conventional formulation [12, 78] by allowing for a non-constant intrinsic permeability k^s of the porous material, i.e., k^s remains within the divergence operator. The Cauchy extra stress tensor $\boldsymbol{\sigma}_E^s(\mathbf{u}_s)$ represents Terzaghi's effective stress [93] where \mathbf{u}_s represents the elastic displacement of the solid skeleton. Here the engineering-sign convention is followed, according to which the extra stresses of the solid phase are defined as negative for compression and fluid pressure p is defined as positive. The term to the right-hand side of equation (3.3) represents body forces \mathbf{b} . The Biot-Willis parameter $\alpha = 1 - K_d/K^s$ is related to the ratio of the frame bulk modulus K_d (drained modulus) and the grain's average bulk modulus K^s . The inverse of Biot's coupling coefficient M , which represents the specific storage capacity at a material point, reads

$$\frac{1}{M} = \frac{\phi}{K^f} + \frac{\alpha - \phi}{K^s}. \quad (3.5)$$

The set of poro-elastic equations is solved in the fracture domain and in the porous matrix for different material properties. It is assumed that the porosity $\phi \sim 1$ in the fracture domain and that K_d of the surrounding matrix is much larger than K_d of the fracture domain. For these assumptions, the storage at a material point is only related to the fluid bulk modulus ($M \rightarrow K^f$).

The local permeability k^s at a material point in the fracture is assumed so high that the fluid velocity is controlled by the geometry of the conduit structure, i.e., the relevant permeability is controlled by the aperture as quantified in equation (3.2). The relative fluid velocity \mathbf{w}_f in the fracture, when described by Darcy's law, reads

$$\mathbf{w}_f = -\frac{k(r, t)}{\eta^f R} \operatorname{grad} p. \quad (3.6)$$

The deformation of the fracture surface is evaluated by solving equation (3.3) and prescribing the permeability at each position r along the fracture domain. This way, permeability variations depend on the fracture surface deformation that in turn is affected by the entire pressure distribution. It is however assumed that permeability is constant in the vertical direction inside the fracture domain.

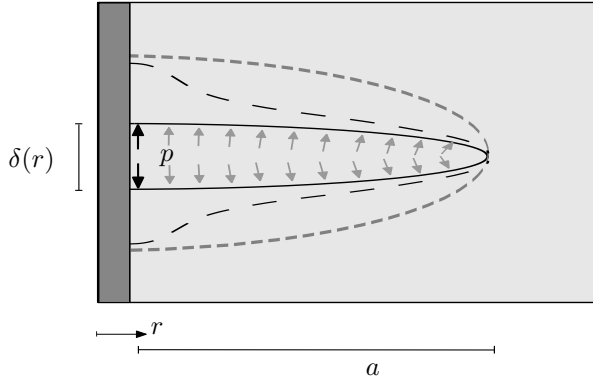


Figure 3.6: Non-local character of fracture deformation due to local pressure changes (black arrows and long-dashed line); fracture deformation due to constant pressure distribution (grey arrows and short-dashed line).

Besides the effect of fracture deformation on permeability, an additional coupling term ($\alpha \operatorname{div} \partial \mathbf{u}_s / \partial t$ in equation 3.4) results from the deformation of the fracture surface. The velocity of the solid $\mathbf{v}_s = \partial \mathbf{u}_s / \partial t$ at the fracture surface represents the velocity of deformation of the fracture in all directions. Since the deformation in vertical direction is responsible for most of the volume changes in the fracture domain, vertical deformation of the fracture surface causes most of the hydro-mechanical coupling effects.

It is assumed that leak-off, i.e., fluid flow from the fracture to the surrounding matrix, does not occur to isolate the effects of fracture deformation. For this purpose, the surrounding rock is considered impermeable, $k_{\text{rock}}^s = 0$, and it becomes linear elastic within this assumption. The possibility to account for leak-off of fluid into the matrix is however intrinsically implemented in the poro-elastic approach and leak-off driven by the difference in pressure in the fracture and in the surrounding rock can be easily modeled by varying the permeability of the surrounding matrix. Furthermore, the peculiarities of the stiffness of a closed fracture related to the mechanical behavior of the contact asperities [e.g., 62, 63] may be addressed by varying the mechanical properties assigned to the fractured domain.

3.2.4 Hybrid-dimensional approach

An alternative approach to the poro-elastic method, here addressed as hybrid-dimensional approach, is now described that allows for geometries with high aspect ratios. In contrast to the poro-elastic approach, the governing equations are explicitly derived for the fluid flow in the fracture imposing equilibrium conditions in the fluid phase with respect to a deformable fracture embedded

in a deformable rock matrix. The mechanical problem of the surrounding rock is separately treated within linear elastic theory. Fluid flow and fracture deformation are solved in a coupled way by means of the FE solver Comsol Multiphysics. The hydraulic problem along the fracture is modeled as a one-dimensional axisymmetric process. The dimensional reduction constitutes the major difference to the poro-elastic approach.

Again, local fracture permeability is related to local aperture, which is found by solving the three-dimensional elastic problem. The field variable δ appears in both, the hydraulic and the mechanical problem, thus constitutes the coupling variable. The mechanical and hydraulic models are coupled in Comsol Multiphysics by applying the transient pressure distribution in the fracture as a load on the rock matrix in the mechanical model. The resulting displacements of the fracture boundary are added to the aperture values characterizing the fracture transmissivity in the hydraulic model.

Balance of mass and of momentum

First, the balance equation for mass is derived for a compressible fluid in a single horizontal deformable fracture (cf. Section 2.4.1). Mass conservation for the fluid results in a relation between the injected fluid volume, changes in fluid density and fluid velocity, and variations in fracture volume. The conservation of mass is satisfied in the fluid-filled fracture when

$$\frac{\partial}{\partial t} (\rho^{fR} \delta) + \frac{1}{r} \frac{\partial}{\partial r} (r w_{fr} \rho^{fR} \delta) = 0 \quad (3.7)$$

where ρ^{fR} is the (real) effective density of the fluid. An additional mass exchange (leak-off) between the fracture domain and the surrounding matrix can be accounted for by adding a right-hand side/source term but is not referred to at this stage to isolate the effect of fracture deformation.

Balance of momentum (see Section 2.4.2 for a detailed derivation) yields a constitutive equation that links the average fluid velocity w_{fr} in radial direction with the pressure gradient as in equation (3.1), i.e., Darcy's law. The permeability is prescribed as in equation (3.2) depending on the local aperture of the fluid-filled fracture.

Governing equations

Balance of mass (Eq. 3.7) and balance of momentum (Eq. 3.1), applied to the fluid, lead to the nonlinear storage equation (see Section 2.4.3)

$$\begin{aligned} \frac{\partial p}{\partial t} + \frac{1}{12 \eta^{fR} r} \frac{\partial}{\partial r} \left(-\frac{r \delta^2}{\beta_f} \frac{\partial p}{\partial r} \right) - \left(\frac{\delta}{12 \eta^{fR} \beta_f} \frac{\partial \delta}{\partial r} \right) \frac{\partial p}{\partial r} \\ - \frac{\delta^2}{12 \eta^{fR}} \left(\frac{\partial p}{\partial r} \right)^2 = -\frac{1}{\beta_f \delta} \frac{\partial \delta}{\partial t}, \end{aligned} \quad (3.8)$$

complemented by the initial condition for the pressure $p(r, t_0) = 0$. At the intersection of the borehole with the fracture, a pressure $p(r_w, t) = \bar{p}$ or a flux boundary condition $q(r_w, t) = \bar{q}$ can be prescribed. In addition, a no-flux boundary condition has to be enforced only at the fracture tip $q(a + r_w, t) = 0$ since a one-dimensional flow model is used. The associated mechanical problem is solved using the pressure distribution in the fracture to evaluate fracture deformation.

In order from left to right, the governing equation (3.8) comprises a time-dependent pressure term, a diffusion and a convection term, a nonlinear/quadratic term, and a term at the right-hand side. The diffusivity coefficient $C_D = \delta^2/12 \eta^{fR} \beta_f$ and the convection coefficient $C_C = \delta(\partial\delta/\partial r)/12 \eta^{fR} \beta_f$ are non-constant parameters related to the aperture and to the aperture gradient, respectively. Depending on the relative size of the two parameters, the fluid flow is diffusion dominated or convection dominated. The term to the right-hand side is proportional to the variation of the aperture with time and accounts for most of the hydro-mechanical effects. By means of a simple sensitivity study, it was found that changes in diffusivity coefficient C_D and in convection coefficient C_C caused by fracture deformation can be neglected, in comparison to effects caused by the term to the right-hand side. The latter introduces additional physical effects that are investigated in Section 3.3.2 by means of a dimensional analysis and in Section 3.4.3 by means of numerical solutions.

3.3 Analysis of the modeling equations

The two apparently disparate modeling approaches are seen as treating the same fundamental problem of a deformable conductive slit. At face value, the hybrid-dimensional and the poro-elastic approach treat open and closed fractures, respectively. Yet, the models underlying the two approaches are seen as equivalent systems for which conductivity and flow field are captured “correctly” in the sense that the used relations (Eqs. 3.4, 3.8) comply with experimental findings [e.g., 103]. The two employed numerical approaches share the notion that a planar conduit (joint, fracture, or fault) may exhibit considerable hydraulic conductivity even when it is mechanically closed, i.e., the conduit experiences a normal stress that exceeds the fluid pressure along it and thus the opposing conduit surface are locally in contact. Upon this mechanical closure the conduit deformation is controlled by two players: the bulk conduit structure and the local contacts. It is assumed that the two contributions can be superposed and that principal results can be gained from restricting to the contribution of the global conduit structure to its deformability.

3.3.1 Comparison of the modeling equations

Equation (3.8) is analyzed for the hybrid-dimensional approach and is compared to equation (3.4) for the fracture domain only. In contrast to the hybrid-

dimensional approach, the poro-elastic approach is solved for a two-dimensional axisymmetric fracture domain. Nevertheless, due to the high aspect ratio of the fracture, fluid flow develops primarily in radial direction and, therefore, pressure gradient variations in the vertical direction could be neglected. The poro-elastic equation (3.4) was reformulated to facilitate a direct comparison of the two modeling approaches (Table 3.1). Both equations comprise a time-dependent pressure term, a diffusion term with the same diffusion coefficient, a quadratic term, and a term related to fracture volume changes. In the hybrid-dimensional approach a term proportional to the aperture gradient appears, representing convective processes although the flow is simplified to a one-dimensional case. In the derivation of the governing equations (see Section 2.4), the flow is assumed to be one-dimensional but a second dimension, namely the fracture aperture δ , is taken into account in the fluid mass conservation (Eq. 2.14). The aperture variations along the fracture cause the convective effects. Such a convection-related term does not explicitly appear in the governing equation of the poro-elastic approach as convective effects are a result of solving the poro-elastic equations (3.3, 3.4) in the “heterogeneous” structure composed of two different media.

A further difference between the two modeling approaches is the coupling term (Table 3.1). In both equations, it is related to the velocity of the rock deformation and accounts for fracture volume changes. However, the coupling of the elastic deformation is proportional to the gradient $\partial v_{sz}/\partial z$ of the solid velocity in the poro-elastic approach, whereas the hybrid-dimensional approach only approximates the gradient with v_{sz}/δ , where $v_{sz} = \partial\delta/\partial t$ (Table 3.1).

Due to the similarities in the structure of both governing equations, a generic partial differential equation is identified that is characterized by a time-dependent term, convection-diffusion terms, quadratic effects and a hydro-mechanical coupling term. This generic governing equation is investigated by a dimensional analysis using equation (3.8) as an explicit example. Analyzing equation (3.4) instead would yield the same general conclusions.

3.3.2 Dimensional analysis

A quantitative evaluation of the occurring physical effects is now performed by introducing characteristic scales and by non-dimensionalizing the governing equation. Physical dimensions are eliminated from equation (3.8) by substituting characteristic values $\tilde{\Psi}$ to arrive at the following non-dimensional variables Ψ^*

$$\delta = \delta^* \tilde{\delta}, \quad (3.9)$$

$$r = r^* \tilde{r}, \quad (3.10)$$

$$t = t^* \tilde{t}, \quad \text{and} \quad (3.11)$$

$$p = p^* \tilde{p}, \quad (3.12)$$

Table 3.1: Comparison of the governing equation (3.8) and the radial component of equation (3.4).

Model	Transient	Diffusion	Convection	Quadratic	Coupling
Poro-elastic	$\frac{\partial p}{\partial t}$	$+\frac{1}{12\eta^f r} \frac{\partial}{\partial r} \left(-\frac{r \delta^2}{\beta_f} \frac{\partial p}{\partial r} \right)$	-	$-\frac{\delta^2}{12\eta^f r} \left(\frac{\partial p}{\partial r} \right)^2$	$\frac{1}{\beta_f} \frac{\partial v_z}{\partial z}$
Hybrid-dimensional	$\frac{\partial p}{\partial t}$	$+\frac{1}{12\eta^f r} \frac{\partial}{\partial r} \left(-\frac{r \delta^2}{\beta_f} \frac{\partial p}{\partial r} \right)$	$-\left(\frac{\delta}{12\eta^f r \beta_f} \frac{\partial \delta}{\partial r} \right) \frac{\partial p}{\partial r}$	$-\frac{\delta^2}{12\eta^f r} \left(\frac{\partial p}{\partial r} \right)^2$	$\frac{1}{\beta_f} \frac{\partial \delta}{\partial t}$

where $\tilde{r} = a$ denotes the characteristic scale in horizontal direction. A characteristic fracture aperture $\tilde{\delta}$ may be gained from exploiting the analytical solution of a fracture deformed by a constant pressure \tilde{p} [94]

$$\tilde{\delta} = \frac{4(1-\nu^2)}{\pi E} \tilde{p} \tilde{r} := \frac{1}{\tilde{E}} \tilde{p} \tilde{r}. \quad (3.13)$$

Equation (3.13) is used to reduce the set of characteristic values by expressing the characteristic pressure \tilde{p} as a function of the characteristic aperture $\tilde{\delta}$, the characteristic stiffness \tilde{E} , and the characteristic length \tilde{r} , i.e., $\tilde{p} = \tilde{\delta} \tilde{E} / \tilde{r}$. In addition, a characteristic time \tilde{t} is chosen representing the finite rise time of the boundary condition applied at the borehole, i.e., the finite time needed to reach a constant flow rate or pressure. During pumping operations, the transient behavior of the pressure distribution around a borehole is strongly affected by the finite time needed to realize the boundary condition. Relating \tilde{t} to a characteristic diffusion time is inappropriate due to the important effects of the “instantaneous” hydro-mechanical coupling on the pressure transient in high-aspect-ratio fractures.

The governing partial differential equation (3.8) is reorganized and written in terms of the introduced quantities as

$$\begin{aligned} A \frac{r^*}{\delta^{*2}} \frac{\partial p^*}{\partial t^*} - \frac{\partial}{\partial r^*} \left(r^* \frac{\partial p^*}{\partial r^*} \right) - 3 \frac{r^*}{\delta^*} \frac{\partial \delta^*}{\partial r^*} \frac{\partial p^*}{\partial r^*} \\ - B r^* \left(\frac{\partial p^*}{\partial r^*} \right)^2 = -C \frac{r^*}{\delta^{*3}} \frac{\partial \delta^*}{\partial t^*}. \end{aligned} \quad (3.14)$$

The dimensionless numbers in equation (3.14) are defined as

$$A = \frac{12 \eta \tilde{r}^2 \beta_f}{\tilde{\delta}^2 \tilde{t}} = \frac{\text{transient}}{\text{diffusion}}, \quad (3.15)$$

$$B = \frac{\tilde{\delta} \beta_f \tilde{E}}{\tilde{r}} = \frac{\text{quadratic}}{\text{diffusion}}, \text{ and} \quad (3.16)$$

$$C = \frac{12 \eta \tilde{r}^3}{\tilde{\delta}^3 \tilde{E} \tilde{t}} = \frac{\text{coupling}}{\text{diffusion}}, \quad (3.17)$$

where A scales the time dependence of p , B scales nonlinear diffusion effects, and C represents the transient effects caused by hydro-mechanical coupling, all with respect to diffusion phenomena. To efficiently investigate the different limits of equation (3.14), parameter combinations are analyzed for which some phenomena dominate over other phenomena.

First of all, convective effects (represented by the third summand in equation 3.14) are of importance only in the region near the fracture tip. Due to the elliptical shape of the fracture, the aperture gradient $\partial \delta^* / \partial r^*$ is negligible

along the entire fracture, apart from the region near the fracture tip (Figure 3.3). Furthermore, the quadratic term of equation (3.14), scaled by the dimensionless number B , is inversely proportional to the aspect ratio of the conduit, while A and C are proportional to the square and the cube of the aspect ratio, respectively. Therefore, B can be neglected for high-aspect-ratio fractures ($\tilde{\delta} \ll a$). Furthermore, relative to A and C , that scale with fluid viscosity and the inverse of the characteristic time, the quadratic term becomes negligible for fluids with high viscosity and processes with short characteristic times.

For configurations comprising a high-aspect-ratio fracture, a viscous fluid, and a fracture of large extension, equation (3.14) can be reduced to

$$A \frac{r^*}{\delta^{*2}} \frac{\partial p^*}{\partial t^*} - \frac{\partial}{\partial r^*} \left(r^* \frac{\partial p^*}{\partial r^*} \right) = -C \frac{r^*}{\delta^{*3}} \frac{\partial \delta^*}{\partial t^*}, \quad (3.18)$$

which holds for all points in the fracture apart from the fracture tip. The obtained reduced equation represents a transient diffusion equation with a hydro-mechanical coupling term to the right-hand side.

For high aspect ratios in equation (3.18), pressure transient effects are comparable to diffusive effects ($A \sim 1$). Furthermore, the larger the aspect ratio is, the more pronounced the effects due to hydro-mechanical coupling effects. Equation (3.18) can be further reduced to the transient diffusion equation

$$A \frac{r^*}{\delta^{*2}} \frac{\partial p^*}{\partial t^*} - \frac{\partial}{\partial r^*} \left(r^* \frac{\partial p^*}{\partial r^*} \right) = 0. \quad (3.19)$$

when a rigid fracture is investigated ($\tilde{K} \rightarrow \infty$) and/or for low-aspect-ratio fractures. The solution of the diffusion equation permits only positive pressure time derivatives for injection procedures. Inverse-pressure responses (Figure 3.2) are not covered.

The configurations analyzed in the numerical examples comprise compressible fluids, deformable rocks and/or conduits with large aspect ratios (Tables 3.2, 3.3). For these cases, diffusion phenomena as well as hydro-mechanical coupling effects are significant and non-local effects are captured.

3.4 Numerical modeling

3.4.1 Model configuration and solution schemes

Due to discretization issues during the numerical solution procedure (performed in Comsol Multiphysics), the poro-elastic approach cannot be used to solve the fluid flow in a fracture with an aspect ratio $a/\delta \geq 10^5$ (Figure 2.4). Discretization of the narrow geometry of the fracture domain considerably increases the computational effort and, for $a/\delta \geq 10^5$ a mesh without highly distorted elements could not be obtained. On the contrary, in the hybrid-dimensional

Table 3.2: Parameters used for the numerical examples with a low-aspect-ratio fracture ($a/\delta = 2 \times 10^4$).

Input		$a = 100$ m	
		$\bar{p} = 20$ kPa	
		$\delta(r_w, t_0) = 5$ mm	
Poro-elastic	input	$K^s = 33.3$ GPa	grain
		$K_d = 8$ GPa	skeleton
		$G = 15.4$ GPa	skeleton
	calculated	$K^f = 2.2$ GPa	fluid
		$\phi = 0.01$	
		$k_{\text{rock}}^s = 10^{-19}$ m ²	
		K_{eff}	
		$G_{\text{eff}} = G$	
Hybrid-dimensional	input	$K = 29.4$ GPa	
		$G = 15.4$ GPa	

approach meshing the fracture domain is independent of the fracture aperture. Below, conditions that can be handled by both approaches are chosen first, i.e., $a/\delta < 10^5$, and the numerical solutions are presented. The solution obtained with the well-established theory of poro-elasticity constitutes a benchmark for the output of the hybrid-dimensional approach with its inherent approximations. Subsequently, high-aspect-ratio fractures ($a/\delta \geq 10^5$) are investigated using only the hybrid-dimensional approach.

The symmetry of the geometry in vertical direction and the rotational symmetry of the problem around the borehole are exploited and only a quarter of the problem is modeled in both, the poro-elastic approach (Figure 3.4) and the hybrid-dimensional approach (Figure 3.5). For the mechanical problem, symmetry is introduced by constraining the edge on the axis of symmetry with regards to vertical displacements. Furthermore, the horizontal displacements due to fracture deformation are neglected and, therefore, the borehole wall is assumed fixed in radial direction; this way the storage effects of the borehole are neglected. While neglecting borehole storage effects may seem simplistic, it allows us to investigate and isolate effects due to fracture deformation. As an initial condition the pressure $p(r, t_0) = p_0 = 0$ is prescribed.

The direct comparison of results from the two approaches requires compatibility between the poro-elastic and the elastic parameters describing the environment of the fracture. The material parameters in the poro-elastic approach have to be transformed to effective elastic parameters K_{eff} and G_{eff} that can be directly compared to the elastic parameters K and G , employed in the hybrid-dimensional approach (Table 3.2). For the effective bulk modulus Gassmann's effective low-frequency result [35, 59] is calculated

$$K_{\text{eff}} = \frac{\phi(1/K^s - 1/K^f) + 1/K^s - 1/K_d}{(\phi/K_d)(1/K^s - 1/K^f) + (1/K^s)(1/K^s - 1/K_d)}. \quad (3.20)$$

The effective shear modulus G_{eff} of the fluid saturated porous material is assumed to be identical to the shear modulus of the dry rock [35].

3.4.2 Results for a fracture with low aspect ratio ($a/\delta = 2 \times 10^4$)

A fracture with an initial aperture $\delta(r_w, t_0) = 5$ mm and half-length $a = 100$ m is modeled, prescribing further characterizing material parameters and boundary conditions as summarized in Table 3.2. The skeleton bulk modulus prescribed for the matrix refers to deformation on the scale of the analyzed fracture length and, therefore, falls significantly below typical bulk modulus values for intact rocks. A pressure boundary condition is applied at the borehole.

Both the poro-elastic approach and the hybrid-dimensional approach yield a decrease of the fluid pressure along the fracture at all times (Figure 3.7). The largest relative deviation

$$DEV = \left| \frac{p_{\text{PE}} - p_{\text{HD}}}{p_{\text{PE}}} \right|, \quad (3.21)$$

between the two numerical solutions $p_{\text{PE}}(r, t)$ and $p_{\text{HD}}(r, t)$ for the poro-elastic approach (subscript PE) and the hybrid-dimensional approach (subscript HD), respectively, occurs in the vicinity of the borehole (Figure 3.7). However, deviations are small with maximum values in the range of 1 to 2 %.

For comparison, the pressure transient for a rigid fracture ($\partial\delta/\partial t = 0$) was evaluated (Figure 3.7). In this case, convection and diffusion of fluid pressure is much faster than the pressure evolution according to the coupled solutions; the pressure $\bar{p} = p(r_w, t)$, prescribed as the boundary condition at the borehole, is reached throughout the fracture within two seconds. In contrast, the pressure along the fracture is still evolving after five seconds when taking hydro-mechanical effects into account (Figure 3.7). The small fracture deformation caused by the modest applied pressure variations ($\Delta p = 20$ kPa) greatly affects the pressure transient. Furthermore, the transient pressure distribution was evaluated along a deformable fracture, accounting for permeability changes due to fracture deformation but neglecting the hydro-mechanical coupling term on the right-hand side of equation (3.8). The effects of permeability changes alone do not cause noticeable modifications of the pressure transient, but the obtained numerical solution overlaps with the solution for a rigid fracture (Figure 3.7).

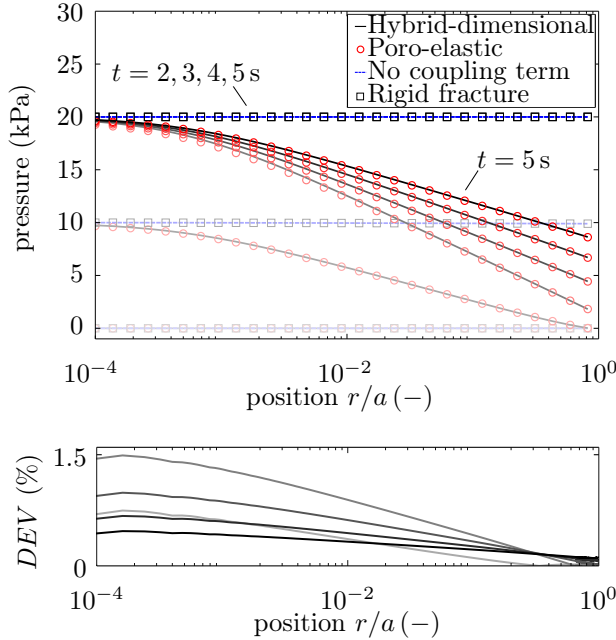


Figure 3.7: Pressure transient along a fracture (for its characteristics see Table 3.2) (top) and deviation between solutions of the poro-elastic approach (Eqs. 3.3, 3.4) and hybrid-dimensional approach (Eq. 3.8) (bottom) ($t = 0 - 5$ s).

3.4.3 Results for a fracture with high aspect ratio ($a/\delta = 2 \times 10^5$)

The fracture investigated was characterized by an initial aperture $\delta(r_w, t_0) = 500 \mu\text{m}$ and half-length $a = 100$ m. In contrast to the previous example, the fluid flow was induced by a flux boundary condition applied at the borehole (Test a in Table 3.3). The evaluation focused on the pressure transient (Figure 3.8, top) at the injection point as well as at a monitoring point at a finite distance $L = 20$ m from the injection point (Figure 3.5).

After injection is initiated, an inverse-pressure response is noted at the monitoring point. There, pressure values first decrease below the initial value (Figure 3.8, bottom). The subsequent increase in pressure represents pressure diffusion along the fracture related to fluid injection but the early behavior of the pressure transient is caused by the very fast (controlled by the propagation velocity of elastic waves) elastic deformation of the fracture due to which its aperture increases along its entire length and therefore fracture volume increases. The non-local character of the elastic deformation affects the fracture almost instantaneously everywhere, even when the transient pressure front is still in the vicinity of the borehole (Figure 3.8, top). As a consequence of this

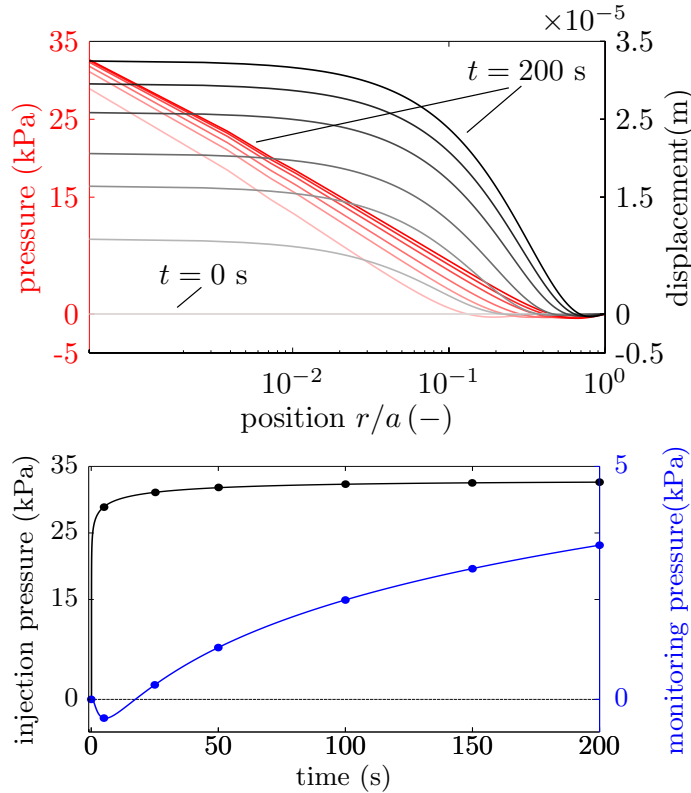


Figure 3.8: Results for a simulation of a high-aspect-ratio fracture using the hybrid-dimensional approach: (top) pressure transient (red line) and rock deformation (black line) along the fracture domain ($t = 0, 5, 25, 50, 100, 150, 200$ s, identified by the circular markers in the bottom figure) with aspect ratio $a/\delta = 2 \times 10^5$; (bottom) pressure evolution at borehole (black line) and at a distance of $L = 20$ m (blue line).

volume increase, the fluid pressure and density in the far field decrease. When the pressure front diffuses further along the fracture, pressure values start to increase.

The sudden pressure drop, referred to as “inverse response to pumping”, is one of the critical observations caused by hydro-mechanical effects. This phenomenon is documented by experimental data (Figure 3.2) and, in Section 3.4.4, it is shown that the numerical models quantitatively match field observations for realistic parameters. Similar inverse-pore-pressure effects have been investigated in poro-elastic initial-boundary-value problems, cf. Mandel-Cryer effect [97].

3.4.4 Quantitative modeling of critical observations

During previously reported field tests [see 75], pressure was recorded at the injection borehole and at monitoring boreholes (Figure 3.1). Numerical solutions for the transient pressure in the fracture obtained from the hybrid-dimensional approach are compared to the experimental data to find a set of input parameters of the initial-boundary-value problem for which modeling results match the observations. The numerical modeling simply used the pumping protocol of the field-test rates as boundary condition.

The pressure transients at the injection borehole and at one of the monitoring boreholes determined by the hybrid-dimensional approach qualitatively fit the experimental data during all pumping phases (Figure 3.9). The “inverse response to pumping” in the monitoring borehole is captured when injection is started, pumping stopped, and production started, i.e., at any variation in the applied boundary condition at the borehole. Sudden pressure changes near the borehole cause deformation along the entire fracture. During fluid injection, a sudden volume increase is accommodated by a sudden pressure drop in the monitoring well. When production is started, a localized pressure drop near the borehole causes the aperture to decrease at all points in the fracture and therefore, generates a sudden pressure increase in the monitoring well.

A simple trial and error approach complemented by a sensitivity study yield a representative set of parameters for which the computed results quantitatively match the field data (Test b in Table 3.3). The obtained geometrical constraints (i.e., fracture length a and aperture δ) for the effective fracture are of reasonable order of magnitude and so is the constraint on the elastic properties of the surrounding rock. The obtained parameters are a fracture length $a = 100$ m, an initial fracture aperture $\delta(r_w, t_0) = 600$ μm at the borehole intersection, and a bulk modulus of the linear elastic material surrounding the fracture $K = 1.4$ GPa. The bulk modulus, which represents the deformation behavior of a jointed rock mass on the scale of tens of meters, is expected to fall significantly below typical modulus values for rock-forming minerals or intact rocks particularly for the shallow depths of the examined wells. In support of this notion, estimates

Table 3.3: Parameters used for the numerical examples with high-aspect-ratio fractures ($a/\delta > 1 \times 10^5$).

	Test a	Test b
a (m)	100	100
K (GPa)	8.3	1.4
G (GPa)	3.8	0.65
\bar{q} (l/min)	24	24
$\delta(r_w, t_0)$ (mm)	0.5	0.6
K^f (GPa)	2.2	2.2
L (m)	20	20

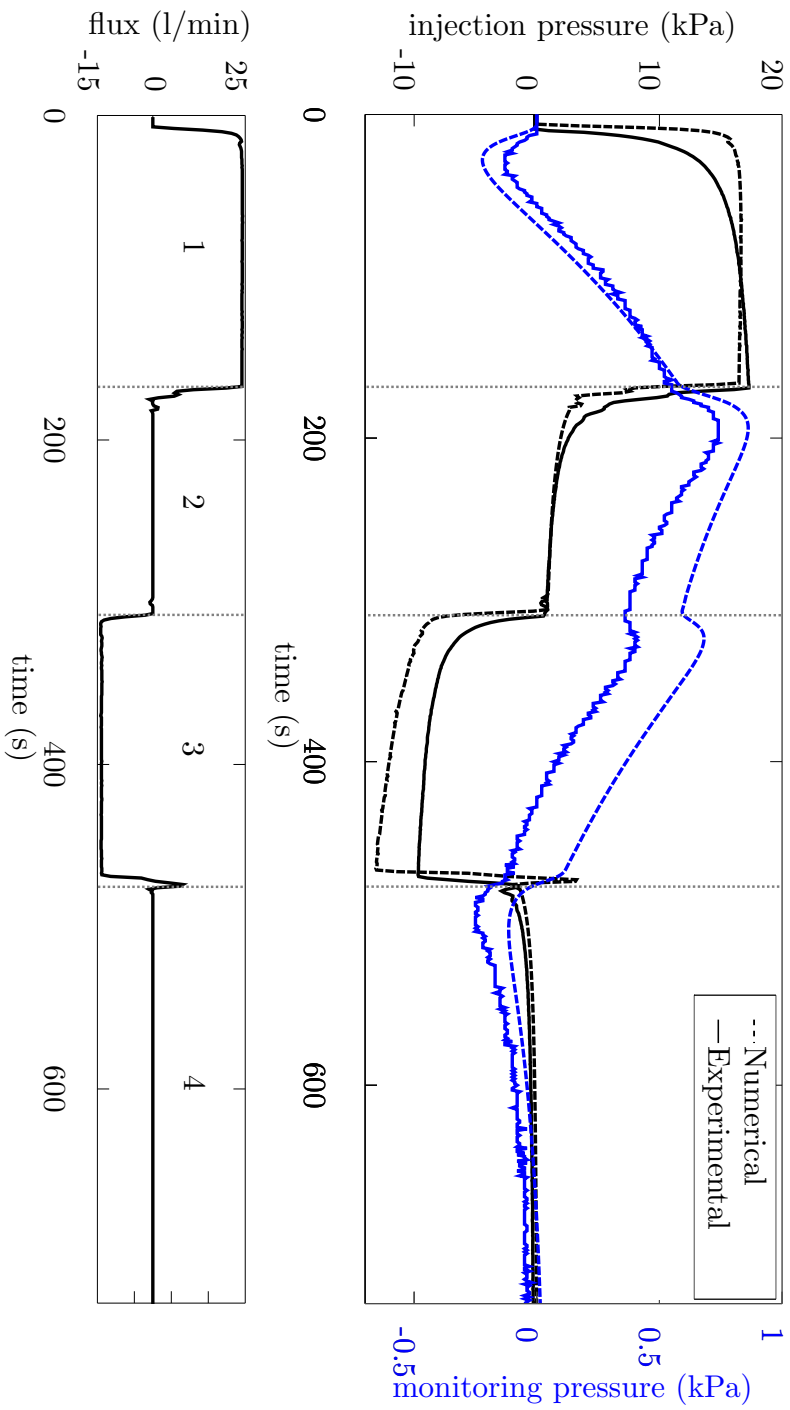


Figure 3.9: Pressure evolution at the injection borehole (black lines) and at monitoring borehole (blue lines) at 20 m distance: comparison of numerical solutions (dashed lines) and field data (solid lines). The vertical dashed lines separate sequences of 1) injection, 2) pause, 3) production, and 4) pause. The numerical simulation considered a high-aspect-ratio fracture ($a = 100$ m, $\delta = 600\mu\text{m}$) surrounded by linear elastic rock material ($K = 1.4$ GPa, $G = 0.65$ GPa).

of the rock mass modulus (following Hoek & Diederichs [44]) derived based on classification (see for example Bieniawski [11]) of drill cores of the tested wells range from approximately 1 GPa to about 10 GPa at most.

In addition to implementing an automated fitting routine, an improved fitting of the experimental data could likely be obtained by accounting for further physical processes, e.g., fluid leak-off and well storage. Loss of fluid mass from the fracture volume towards the neighboring matrix may account for some of the quantitative differences between the recorded and modeled pressure transients at both, the injection and monitoring borehole. However, the aim is to demonstrate that the counterintuitive pressure transient can in principle be explained by hydro-mechanical coupling without additional phenomena.

3.5 Discussion

The presented approaches rely on the assumption that the fluid flow is controlled by the aperture distribution along the fracture. In both approaches contact between the fracture surfaces is neglected. The applicability of the approach is limited by the validity of the cubic law employed for the description of the flow problem. While the cubic law still holds for fractures that are mechanically closed it is not applicable to fractures with large contact areas compared to the entire fracture surface or fractures approaching a percolation limit by other contact characteristics. Despite the differences in the derived governing equations (Eqs. 3.3, 3.4 vs. Eq. 3.8) numerical solutions obtained with the hybrid-dimensional approach closely match the ones of the poro-elastic approach considered an appropriate benchmark (Figure 3.7). The hybrid-dimensional approach is well suited for the investigation of fluid conduits characterized by high aspect ratios, inaccessible by the poro-elastic approach due to meshing problems. In particular for high-aspect-ratio inclusions, it was concluded that parameters characterizing the bulk properties of the conduit, e.g., the storage capacity of the fracture, cannot be accounted for by a scalar representing a macroscopic property but the coupling between changes in conduit volume and pressure along it varies with time and is non-local.

The hybrid-dimensional approach can be used to investigate several different problems involving hydro-mechanical coupling in addition to the ones presented. The approach models fluid flow in long and narrow fractures, avoiding the discretization issues associated with such narrow geometrical domains. Though the analysis lent towards fluid flow caused by injection procedures in a well, it is applicable to flow induced by fracture-volume changes due to changes in the bulk stress state, such as “squirt flow” [e.g., 59] or “fracture flow” (cf. Chapter 5), as well. The macroscopic properties of representative elementary volumes containing one or more high-aspect-ratio fractures can now be systematically investigated with respect to their distribution, density or orientation at modest computational expenses and almost unrestricted in terms of aspect ratio. Nevertheless, when generalizing the hydro-mechanical coupled problem

to non-horizontal fractures, axial symmetry is lost and gravity forces cannot be neglected in the derivation of the equation governing the fluid flow. These assumptions fail also for cases with multiple intersecting fractures, in which, additionally, mass exchange between the fractures has to be accounted for in the fluid mass conservation.

The hybrid-dimensional approach is a tool to constrain effective properties of fractured materials and thus may build the basis for more complex investigations accounting for multiple fractures and aiming at their significance for the pressure response. In the field of reservoir engineering, effective properties of the rock surrounding a borehole can be inferred by numerically modeling of field data recorded during pumping operations, in particular critical observations as the inverse-pressure response. Application of different injection-production patterns allows for further characterization of the fractured rock. By means of optimization techniques, the numerical results can be fitted to field data and an “ideal” set of parameters characterizing the fractured rock can be obtained.

Further development of the hybrid-dimensional approach can consist in including a loss of fluid mass from the fracture domain, i.e., leak-off. In addition, the assumption of Poiseuille flow can be abandoned for closing fractures with high contact areas. A different flow rule has to be implemented in the derivation of the governing equations. Accounting for contact between asperities on the fracture surface leads to a more complex behavior of the deformation of the fracture than in this study and, therefore, to investigations towards additional effects caused by hydro-mechanical coupling.

3.6 Conclusions

In this study of the hydro-mechanical behavior of a single deformable fracture in the subsurface, attention was focused on fluid pressure as the driver for fracture deformation perturbing fluid flow. Two approaches describing the coupled hydro-mechanical problem of fluid injection from a borehole into surrounding rock containing a hydraulically open and deformable fracture were derived and compared. The first approach was based on Biot’s poro-elastic equations and both, the surrounding rock and the fracture domain, were modeled as porous materials. This approach, consider a benchmark for hydro-mechanical problems, showed limitations when trying to solve problems with fractures characterized by large aspect ratios. Therefore, a hybrid-dimensional approach that overcomes these limitations was derived, for which the governing equation was gained by enforcing balance of mass and momentum of the fluid specifically for the assumed ellipsoidal geometry of the fracture. In both approaches, contact between fracture asperities was not explicitly treated but it was relied on the validity of the cubic law for fractures with touching surfaces. The two approaches yield closely matching results when applied to the same problem. For a high-aspect-ratio fracture, an initial-boundary-value problem was presented and solved with the hybrid-dimensional approach alone. The performed dimen-

sional analysis revealed the role of different physical phenomena for differing test cases in dependence of the choice of material and geometrical properties. For the cases investigated, i.e., high-aspect-ratio fracture and water as injected fluid, the governing equation takes the form of a convection-diffusion equation with transient effects due to hydro-mechanical coupling that specifically captures the non-local fracture deformation caused by the pressure transient along the single fracture. Due to the non-local character of coupling, a single storage capacity parameter for the conduit is insufficient to fully capture critical observations such as inverse-pressure response. The hybrid-dimensional approach quantitatively models field observations including the inverse-pressure response. Neglecting the effects of fracture deformation yields strongly different numerical results.

Chapter 4

The imprint of hydro-mechanical effects in periodic pumping tests

4.1 Introduction

Pressure transients induced by injection into or production from wells during pumping operations have since long been analyzed to understand and describe geometric and hydraulic properties of the surrounding rock material [e.g., 34, 57]. Characterization of the subsurface's conduit structure is essential to understand fluid transport and thus is related to solutes, suspended solids, and heat carried along with it. Knowledge of the characteristic material and geometric parameters of the rock surrounding the wells, as well as of the occurring physical phenomena, is crucial during management of water resources as well as during exploration of oil and gas reservoirs. When interpreting data from pumping operations the challenge is to predict long term flow rates, for example over years (fresh water supply, hydrocarbon production, CO₂ sequestration) or centuries (geothermal energy provision), using the information obtained from short term experiments, for example by pressure perturbations lasting from some seconds to few hours.

Pumping tests in wells typically yield pressure values measured at the injection borehole and in cases also at one or more monitoring boreholes. The pressure transient is the result of hydraulic and mechanical processes whose balance depends on various geometric and material properties of the rock surrounding the wells. The pumping protocol also strongly affects to which extent processes are activated. In addition to conventional pulse or step testing [e.g., 49, 50, 91], harmonic [74] or non-harmonic [75] periodic successions of single frequency or multi frequency pumping signals were imposed [e.g., 19, 75].

Pumping tests have been employed in field experiments, theoretical investigations, and numerical approaches. Modeling of the pressure transients can be used as a predictive tool that allows the operator for characterization of reservoirs surrounding a well [e.g., 3, 20] and, as an extension, allows for sensitivity studies of flow characteristics with respect to various geometric and material parameters. Numerical hydro-mechanical analyses accounting for pressure-sensitive media have been performed [e.g., 62, 65, 95]. Pulse testing procedures were numerically modeled to fit field data and allow for parameter identification [18].

In this work, numerical modeling of periodic pumping tests is presented to understand the implications of hydro-mechanical coupling on the pressure transient. Inverse-pressure response constitutes a prominent example of the importance of hydro-mechanical effects [cf. 36, 88, 98]. Synthetic data are produced employing two different models that describe the induced fluid flow. The hybrid-dimensional approach (cf. Chapters 2, 3) is used to account for hydro-mechanical coupling. This method relies on basic conservation laws and does not introduce a priori assumptions on the fracture-storage capacity.

Storage capacity as a variable characterizing a fracture has been analyzed for well tests [63]. The limitations of introducing the concept of storage capacity as a macroscopic property of the fracture are investigated. The numerical solutions of an approach accounting for a simplified fracture-storage capacity [76] (cf. Section 2.3.2) are compared to fully coupled results. Pressure transients are qualitatively analyzed in the time domain. Relying on fast Fourier transformation (FFT) pressure records are quantitatively studied in the frequency domain. With the aim to estimate equivalent hydraulic parameters in mind, the sensitivity of the pressure transients to geometric and material parameters is investigated for both modeling approaches.

4.2 Background and modeling approaches

4.2.1 Configuration of the wells and the fracture

Pumping procedures are investigated involving periodic injection of fluid into and production from a vertical well. Pressure is monitored in the pumping well and at distances $L_i = 5 \dots 550$ m from the injection point, cf. Figure 4.1. All boreholes are assumed to intersect a single horizontal ellipsoidal fracture of half length a , where $a \gg r_w$, through which fluid flow is induced. The material surrounding the fracture is considered as a poro-elastic medium [12]. Yet, fluid mass exchange between the fracture and the surrounding rock, i.e., leak-off, is “inhibited” by assigning a permeability of $k^s = 10^{-22}$ m² to the porous material. A low rock permeability is used to isolate effects induced by pressure transport phenomena along the fracture, e.g., diffusion or hydro-mechanical coupling effects. A periodic fluid-flow transient, consisting of a succession of injection, no-pumping, production, and no-pumping, was applied at the injection borehole with periods $T = 37, 370$, and 3700 s. The choice of

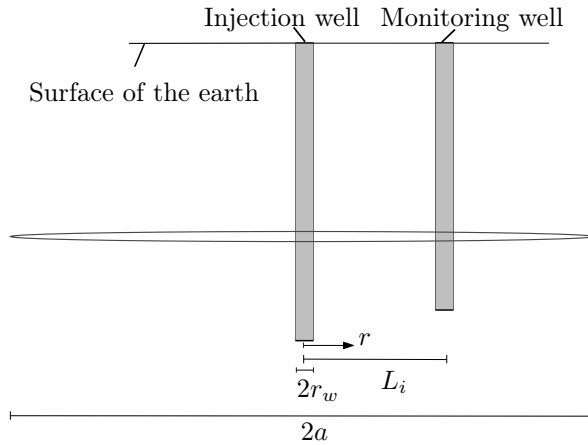


Figure 4.1: Analyzed configuration: injection well (with radius r_w) and monitoring wells (at distances $5 < L_i < 550$ m) intersecting a single ellipsoidal fracture of length $2a$.

material parameters, geometric properties, and injection boundary conditions (Table 4.1) is based on fitting of field data performed in Section 3.4.4.

4.2.2 Modeling

Hybrid-dimensional approach

Previously, a subsurface-fluid flow model (cf. Chapter 3) was developed to interpret and analyze data records obtained during field tests [75]. The hydro-mechanical problem of fluid injection in a deformable conduit is accounted for by a hybrid-dimensional approach. A fully coupled set of equations was derived from basic conservation laws for a specific heterogeneity, i.e., a horizontal fracture modeled as an ellipsoid. In Chapter 3 it was shown that this approach provides numerical approximations that are very similar to Biot's equations used to model a poro-elastic slit in poro-elastic matrix.

Fluid flow along the fracture is addressed as a one-dimensional axisymmetric process with the governing equation (2.24). The governing equation (2.24) was derived imposing equilibrium conditions in the fluid phase with respect to a deformable inclusion surrounded by a rock matrix. The surrounding material is referred to as a two-dimensional axisymmetric domain, cf. Figure 4.2. Mechanical deformation as well as fluid flow through the porous rock are modeled by means of the poro-elastic equations (2.4) and (2.6).

The set of governing equations comprising equation (2.24) and the poro-elastic equations (2.4), (2.6) is complemented by the boundary conditions for the pressure and the solid displacement. On the boundaries of the one-

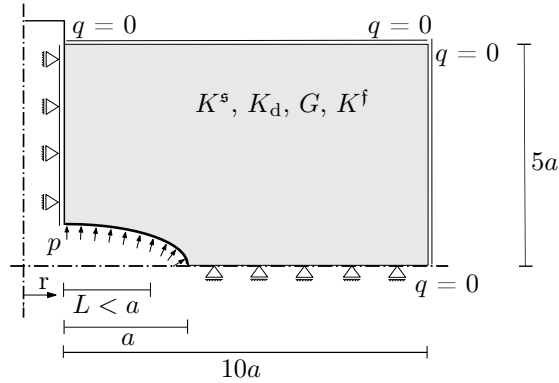


Figure 4.2: Geometry and initial-boundary-value problem of the surrounding rock material: two-dimensional axisymmetric poro-elastic domain.

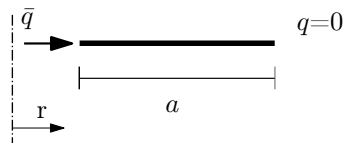


Figure 4.3: Geometry and initial-boundary-value problem related to fluid flow: one-dimensional axisymmetric domain of the fracture.

dimensional axisymmetric domain a flux boundary condition $q(r_w, t) = \bar{q}$ and a no-flux boundary condition $q(a, t) = 0$ are applied at the injection point and the fracture tip, respectively (Figure 4.3). The pressure $p(r, t)$ along the fracture is coupled to the fracture surface of the porous rock domain (Figure 4.2), while the porous rock displacement is coupled to the aperture of the fracture, cf. δ in equation (2.24). At the boundaries of the two-dimensional axisymmetric domain, representing the far field, undrained boundary conditions are applied and, according to symmetry, vertical displacement is fixed at the lower edge. The injection and monitoring boreholes are not accounted for in the one-dimensional axisymmetric domain and, therefore, borehole storage effects are not modeled. Pressure transients at the wells are obtained as data read outs at predefined distances along the modeled fracture domain.

Diffusion-based approach

As an alternative to a fully coupled hydro-mechanical treatment of the problem, pressure transport along a deformable conduit can be addressed by the simple

Table 4.1: Parameters used for the simulation of periodic pumping tests.

Periodic pumping		
Pumping	$T = 370$ s	
	$\bar{q} = \pm 24$ l/min	
Fracture	$a = 1000$ m	
	$\delta_0(r_w) = 640$ μm	
Surrounding rock (hybrid-dimensional)	$K^s = 14$ GPa	grain
	$K_d = 1.4$ GPa	skeleton
	$G = 0.65$ GPa	skeleton
	$K^f = 2.2$ GPa	fluid
	$\phi = 0.02$	
	$k^s = 10^{-22}$ m ²	
Storage multiplier (diffusion-based)	$\alpha_s = 10^5$	

diffusion equation (2.7), cf. Section 2.3.2. A diffusion-based approach relies on the assumption that for some combinations of material parameters or applied boundary conditions the equation governing the fluid flow can be decoupled from the mechanical problem describing the surrounding rock.

The hybrid-dimensional approach is considered to yield the full behavior and diffusion equations to be intrinsically correct only for undeformable materials. In this work, a diffusion-based approach is used to investigate which apparent fracture-storage capacity were needed to closely match the basic characteristics of the fully coupled response.

Analytical solution for periodic radial flow

As a comparison to the numerical models, analytical solutions of the diffusion equation (2.11), which governs radial fluid flow in a homogeneous medium, are used in the frequency domain for periodic boundary conditions at the injection well. Analytical solutions for sinusoidal injection pressure signals and no-flux boundary conditions at $r = a$ were derived [75]. The periodic pressure transients at the injection borehole as well as at the monitoring boreholes, transformed in the frequency domain, are characterized by a phase φ_i for the imposed period T and an amplitude A_i . Phase differences $\Delta\varphi_i$ and amplitude ratios A_i/A_0 between signals at monitoring wells and the injection borehole are interpreted to describe the occurring physical phenomena along the fracture.

Analytical solutions of the diffusion-based approach provide characteristic lines in the phase-shift amplitude-ratio domain, to which numerical results can be conveniently compared. The analytical solution weakly depends on the monitoring distance r . With increasing distance, the characteristic line in the

phase-shift amplitude-ratio domain shift downwards. For illustration, in this investigation the analytical solution for $r = 5$ m is used, i.e., 100 times the well radius r_w .

4.2.3 Processing and analysis of numerical data

The use of periodic signals allows one to employ fast Fourier transform (FFT) analysis to identify the phase shift $\Delta\varphi_i = \varphi_i - \varphi_0$ of the pressure transient $p_i(t)$ at the monitoring boreholes with respect to the pressure $p_0(t)$ at the injection borehole. Analysis in the frequency domain provides phase shift between two signals within a common period. In cases, when the phase shift $\Delta\varphi$ exceeded one period, potential ambiguities were avoided checking the signal by eye. The amplitude reductions A_i/A_0 between the pressure amplitude A_i at the monitoring boreholes and the amplitude A_0 at the injection borehole were also evaluated by means of the FFT analysis.

Before transformation to frequency domain, pressure records were post processed to eliminate transient non-oscillatory effects within the first pumping cycles. In some cases a tapered cosine window was used to ensure that the pressure transient started and ended with identical values. The phase shifts $\Delta\varphi_i$ and amplitude ratios A_i/A_0 are used to analyze pressure transients along the single fracture for the hybrid-dimensional approach and the diffusion-based approach with the aim to characterize the hydro-mechanical response during periodic pumping procedures. The analytical solution provides characteristic lines in the dimensionless amplitude-ratio phase-shift domain, to which numerical results are compared.

4.3 Results

Synthetic data were produced for periodic pumping tests employing a) the hybrid-dimensional and b) the diffusion-based approach. Pressure transients are qualitatively compared in the time domain but an extensive quantitative comparison is restricted to the frequency domain (relying on FFT of pressure records).

First, the pressure transients are separately analyzed in the pumping and monitoring wells, and the sensitivity of the maximum pressure reached in the monitoring borehole p_{\max} to geometric and material properties (Table 4.2) is investigated. For the diffusion-based approach, the sensitivity of the storage multiplier α_s , needed to fit the simple diffusion results to the fully coupled ones, is analyzed with respect to variations in input parameters. Finally, an interference analysis is performed, comparing pressure values at the injection and monitoring wells.

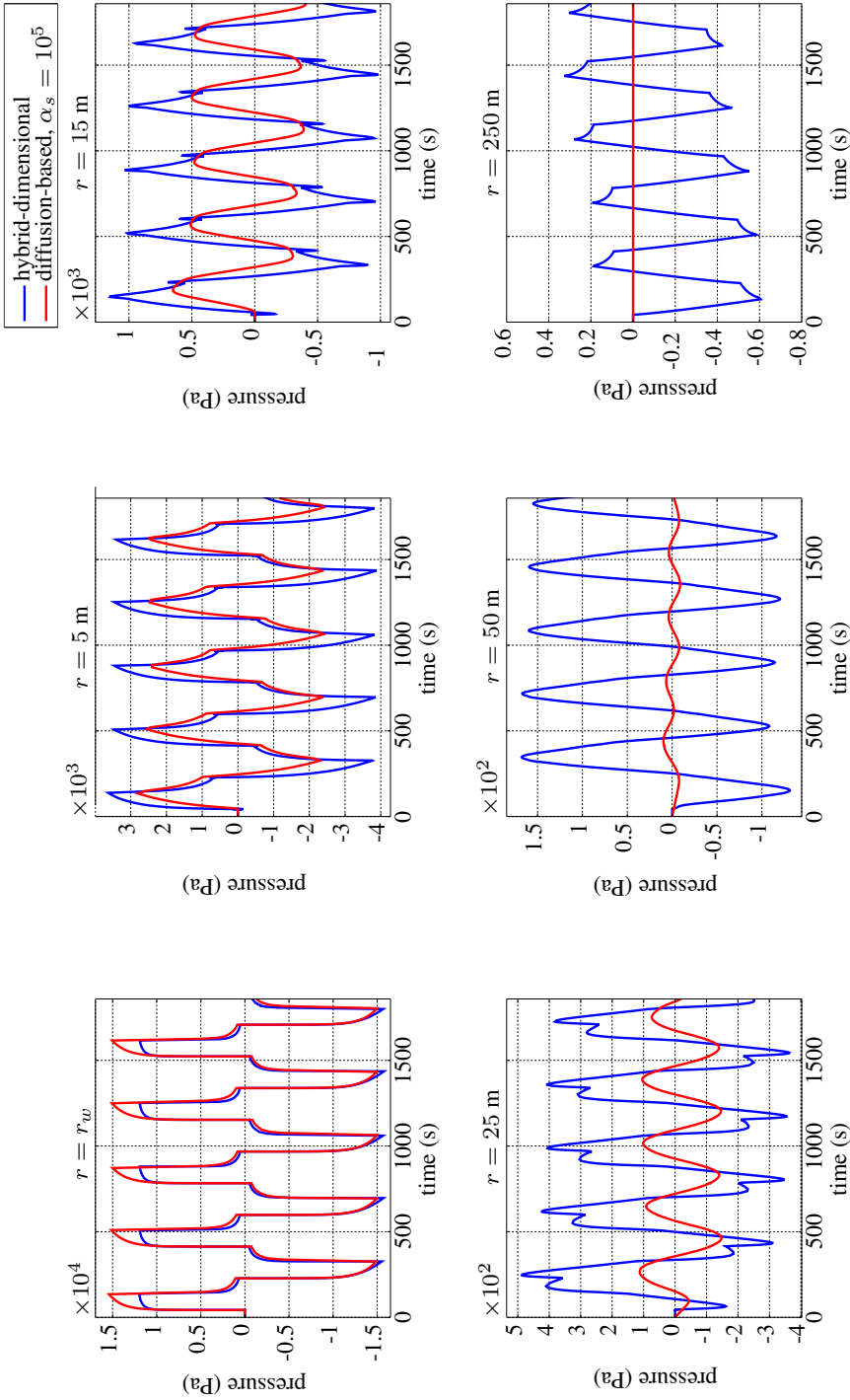


Figure 4.4: Transient pressure at injection borehole and monitoring boreholes at $r = 5, 15, 25, 50, \text{ and } 250 \text{ m}$. Solutions of the hybrid-dimensional approach with full hydro-mechanics (blue line) and with the diffusion-based approach ($\alpha_s = 10^5$) (red line). Pumping period $T = 370 \text{ s}$, initial aperture $\delta_0(r_w) = 640 \text{ }\mu\text{m}$, and fracture half length $a = 1000 \text{ m}$.

Table 4.2: Ranges of parameters used for the sensitivity analyses.

p_{\max}	
Aperture	$\delta_0(r_w) = [0.1 \dots 5]$ mm
Drained bulk modulus	$K_d = [0.8 \dots 250]$ GPa
Storage multiplier (diffusion-based)	$\alpha_s = [10^4 \dots 10^{7.5}]$
Inverse response	
Aperture	$\delta_0(r_w) = [0.2 \dots 1]$ mm
Drained bulk modulus	$K_d = 1.4$ GPa
Half-length	$a = 1000$ m
Aperture	$\delta_0(r_w) = 0.3$ mm
Drained bulk modulus	$K_d = [0.7 \dots 142]$ GPa
Half-length	$a = 1000$ m

4.3.1 Pressure analysis in the time domain

Pumping well

The fully coupled approach yields a peculiar asymmetry in the pressure transient at the injection well (Figure 4.4). Pressure excursions from the initial pressure remain smaller during injection than during production. The asymmetric pressure profile suggests that the mechanical response of the fracture is sensitive to the type of the applied procedure, i.e., if mass is added to or removed from the fracture domain.

Depending on the combination of $\delta_0(r_w)$ and K_d , pressure values at the injection borehole reach $p_{\max} \sim 10^2$ Pa (for large apertures and soft rock) or $p_{\max} \sim 10^6$ Pa (for thin fractures and stiff rock), cf. Figure 4.5. On the one hand, pressure is strongly sensitive to fracture aperture. Changes of $\delta_0(r_w)$ affect fracture permeability as well as the relative importance of hydro-mechanical coupling phenomena to diffusion processes. On the other hand, pressure values are weakly sensitive to K_d for large apertures, but for $\delta_0(r_w) < 1$ mm.

The diffusion-based approach can approximate the transient obtained with the fully coupled hydro-mechanical model well when α_s is chosen correctly, but for the asymmetry of the pressure profile between injection and production phases. In a simple diffusion problem, pressure p_{\max} reached at the injection borehole is caused by the flux boundary conditions applied and depends on the fracture transmissivity and on bulk storage capacity. In contrast, the hydro-mechanical approach explicitly accounts for local changes in aperture. For the chosen combinations of apertures and rock bulk moduli (Table 4.2, top) the

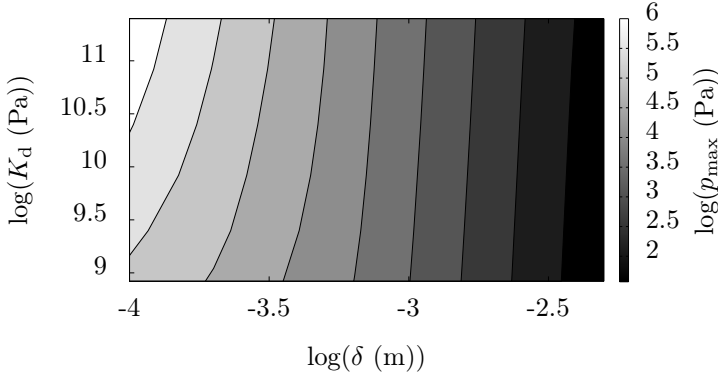


Figure 4.5: Contour of logarithm of pressure p_{\max} at monitoring borehole for combinations of initial aperture $\delta_0(r_w)$ and dry modulus K_d from 0.1 to 5 mm and from 0.8 to 250 GPa, respectively.

storage multiplier that leads to a match between pressure transients obtained with the hybrid-dimensional approach and with the diffusion-based approach varies by over three orders of magnitude, from $\alpha_s \sim 10^4$ to $\alpha_s \sim 10^{7.5}$ (Figure 4.6). The storage multiplier strongly depends on the rock stiffness, independent of the chosen initial aperture $\delta_0(r_w)$. In a weaker way it also depends on fracture aperture.

Monitoring wells

The fully coupled approach yields pressure transients that are dominated by oscillations caused by inverse response for large monitoring distances ($r > 0.05a$), where in general pressure decreases. At $r = 15$ m, inverse response is a short pressure perturbation taking place shortly after any change in injection boundary condition, superposed on pressure oscillations driven by diffusion. At $r = 50$ m, contributions from hydro-mechanical coupling are larger than oscillations caused by diffusion. At distances $r > 130$ m, pressure variations are uniquely caused by inverse-pressure response and oscillations caused by pressure diffusion alone can be neglected, cf. Figure 4.4.

The fit of the diffusion-based approach by choosing α_s is limited to the pressure transient at the pumping well only. Pressure transients are monitored at 5, 15, 25, 50, and 250 m. For the solutions of the diffusion-based approach amplitude reduction is more pronounced than for the solutions of the hybrid-dimensional approach. Clearly, the diffusion-based approach fails to capture hydro-mechanical coupling effects that take place along the fracture, e.g., inverse response. However, also the penetration depth of the diffusion pressure front is limited and, in comparison to the coupled problem, pressure amplitude decreases faster.

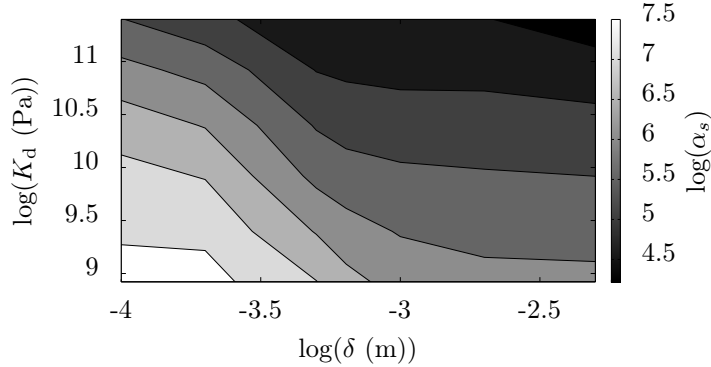


Figure 4.6: Contour of logarithm of storage multiplier α_s for combinations of initial aperture $\delta_0(r_w)$ and dry modulus K_d from 0.1 to 5 mm and from 0.8 to 250 GPa, respectively.

Sensitivity of inverse response to fracture aperture and stiffness

Pressure inverse response is a prominent evidence of the importance of hydro-mechanical effects during pumping operations. In the following, the relation of inverse response to different values of $\delta_0(r_w)$ and of rock drained bulk modulus K_d is investigated. Instead of a flux boundary condition, that corresponds more closely to field experiments, a pressure boundary condition $\bar{p} = 20$ kPa is applied at the injection point to more conveniently compare the pressure transients along the fracture, cf. Figure 4.7.

With increasing aperture and constant fracture length (see Table 4.2 (bottom) for parameters used), inverse response quantitatively diminishes, vanishing for very wide fractures (Figure 4.7, top). For the latter case, the hydro-mechanical coupling becomes negligible because the relative magnitude of the fracture deformation decreases with increasing aperture. The additional storage caused by fracture deformation vanishes and pressure transport processes are faster compared to conduits with higher aspect ratio.

The inverse response to pumping quantitatively decreases for stiffer surrounding rocks, its magnitude is inversely proportional to K_d (see Table 4.2 (bottom) for parameters used). For $K_d = 0.7$ GPa, pressure values drop to $p = -4$ kPa (20% of \bar{p}) before diffusion effects take place, while for an ideally rigid fracture no inverse response occurs.

The duration of inverse response is related to the magnitude of the pressure drop, but it is also related to the drained bulk modulus of the rock. For $K_d < 1.4$ GPa, the duration of inverse response is proportional to the stiffness. For $K_d > 1.4$ GPa, the inverse response vanishes more rapidly with increasing stiffness (Figure 4.7, bottom). For the chosen input parameters (Table 4.2, bottom), the duration of inverse response has a maximum around $K_d \sim 1.4$ GPa.

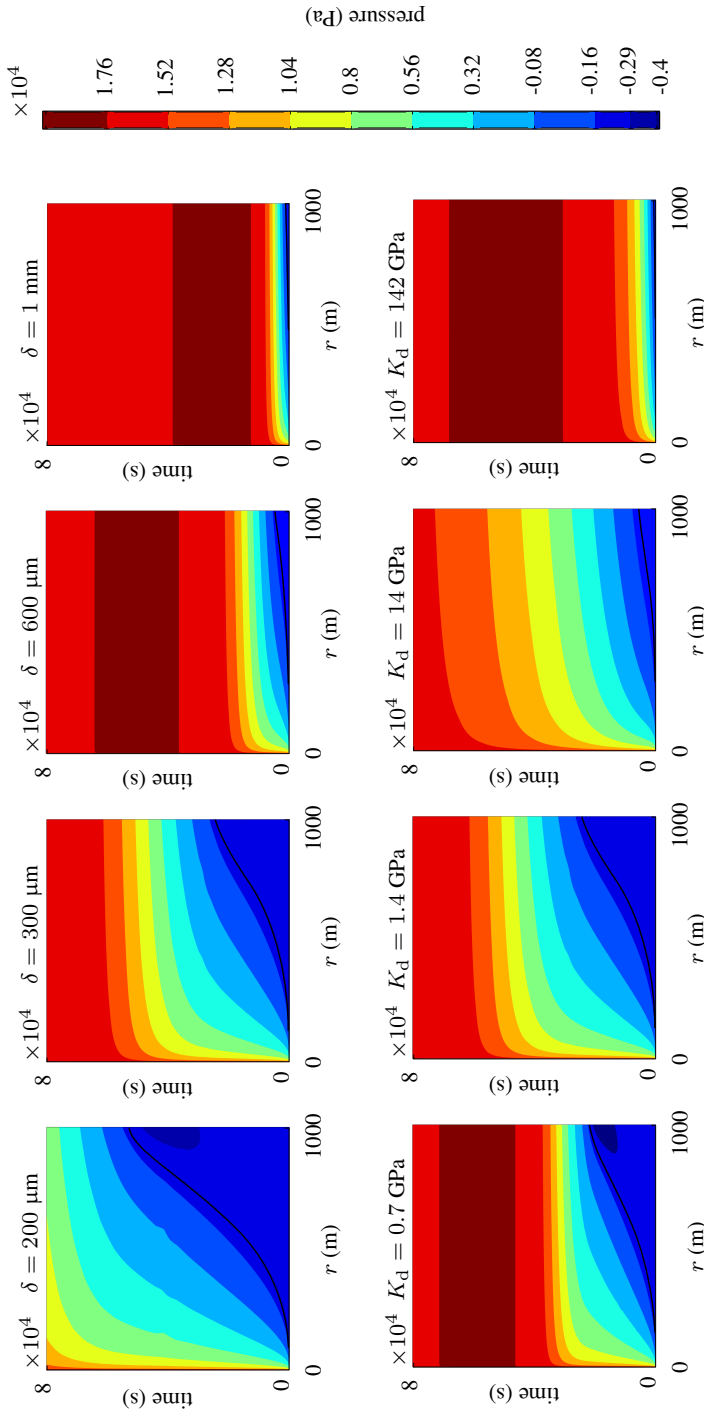


Figure 4.7: Contour of pressure p in the fracture (horizontal axis) along the time domain $t = 0 \dots 8 \times 10^4$ s (vertical axis). Pressure transport is induced by the pressure boundary condition $p(r_w) = \bar{p}$ at the injection well: (top) for $\delta_0(r_w) = 0.2 \dots 1$ mm and $K_d = 1.4$ GPa; (bottom) for $\delta_0(r_w) = 0.3$ mm and $K_d = 0.7 \dots 142$ GPa. The black contour line ($p = 0$) identifies the end of the inverse response. If pressure transport is very fast, pressure redistribution occurs after \bar{p} is reached throughout the domain and the pressure at steady state $p_{\text{eq}} < \bar{p}$.

Time t_{eq} needed to reach a steady state is not directly proportional to K_d . The duration of the inverse response affects the pressure propagation along the fracture. For the given pressure boundary condition \bar{p} at the injection well, a steady state is attained when the prescribed pressure \bar{p} is reached throughout the entire fracture length. On the one hand, for $K_d > 14$ GPa, t_{eq} is proportional to the stiffness. Along rigid fractures a steady state solution is reached much faster than for deformable fractures. Hydro-mechanical coupling effects, which slow down the diffusion process, diminish for large stiffness values. On the other hand, t_{eq} is inversely proportional to the stiffness for $K_d < 1.4$ GPa. Along weak fractures, pressure transport is facilitated by large deformations, which increase the fracture transmissivity. Time t_{eq} reaches a maximum for $1.4 < K_d < 14$ GPa, where pressure transport is slowest (Figure 4.7, bottom).

4.3.2 Pressure analysis in the frequency domain

Phase shift between the pressure signals at the injection borehole and the monitoring wells increases with increasing monitoring distance r up to 90 m, i.e., 9% of the fracture length, while amplitude ratio decreases. The diffusion-based approach yields $\Delta\varphi = 0.11$ to 1.56 cycles and $A_i/A_0 = 0.18$ to 4.5×10^{-6} . The fully coupled calculations yield $\Delta\varphi = 0.052$ to 1.1 cycles and $A_i/A_0 = 0.25$ to 7×10^{-4} , cf. Figure 4.8 (top). For larger distances, i.e., $90 \text{ m} \leq r \leq 550 \text{ m}$, only the fully coupled approach gives significant pressure perturbations resolved by Fourier analysis. At $r = 550 \text{ m}$ phase shift and amplitude ratio were 0.69 and 5.1×10^{-6} , respectively.

Solutions obtained using a diffusion-based approach refer to a simple diffusion equation and thus follow the analytical solution. The latter is independent of pumping period, fracture length and aperture, but weakly depends on the distance of the monitoring boreholes. Here, the analytical solution for $r = 5 \text{ m}$ is used (Figure 4.8, top). For larger monitoring distances the analytical solutions shift downwards. With increasing phase shift, the results of the diffusion-based approach slightly deviate from the analytical solution. The small deviations at distances $r > 25 \text{ m}$ are in agreement with the weak dependence of the analytical solution on monitoring distance.

Numerical results of the fully coupled solution closely follow the analytical solution only for small phase shifts $\Delta\varphi_i$ and amplitude ratio values (Figure 4.8, top). With increasing amplitude reduction, results of the hybrid-dimensional approach deviate from the analytical solution and exhibit larger phase shifts and larger amplitude ratios in comparison to the diffusion-based approach. For $\log(A_i/A_0) < -3$, phase shift values converge to $\Delta\varphi \sim 0.69$ whereas amplitude ratios keep decreasing.

Three domains can be identified for which differences among the ratio of diffusion and hydro-mechanical phenomena are observed. These regions can be visualized along the spatial domain of the fracture (Figure 4.8, bottom). The position $r^* = r/L_{\text{diff}}$ is normalized with respect to the diffusion length $L_{\text{diff}} = \sqrt{DT}$, with $D = \delta^2/(12\eta^{\text{fR}}\beta_{\text{f}})$. In the vicinity of the injection borehole

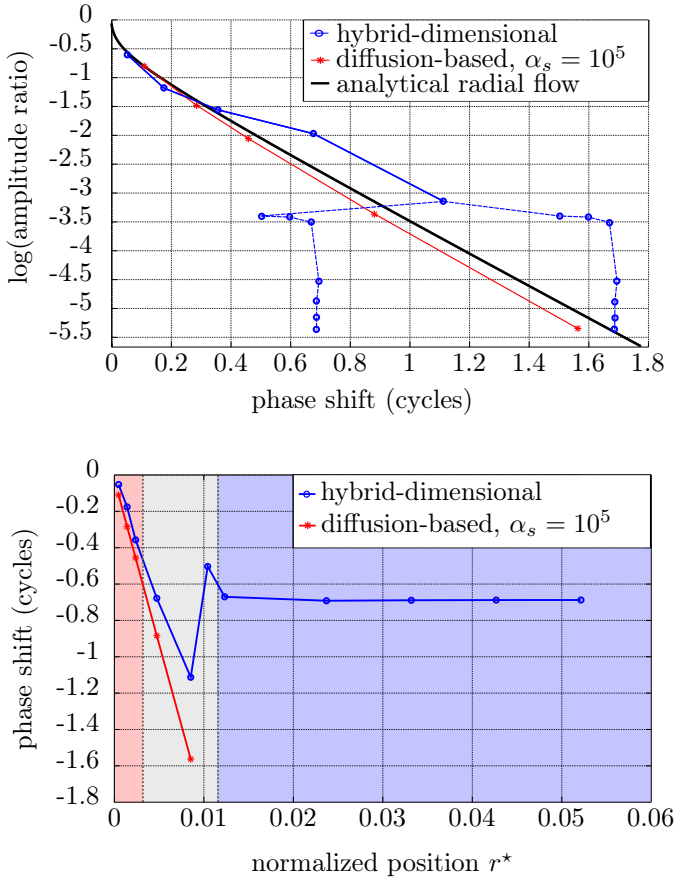


Figure 4.8: Periodic pumping test with period $T = 370$ s, $\delta_0(r_w) = 0.64$ mm, and $a = 1000$. From left to right the markers identify $r = 5, 15, 25, 50, 90$ m. (top) Logarithm of amplitude ratios A_i/A_0 vs. phase shifts $\Delta\varphi_i$ of the transient pressure in the monitoring boreholes with respect to the pressure in the injection borehole. Amplitudes and phase shifts are larger in the hydro-mechanical model, as a result of inverse response. The jump in phase shift and convergence to $\Delta\varphi \sim 0.69$ are also caused by hydro-mechanical coupling. The blue dotted line represents phase shift values at $r = 110 \dots 550$ m with and without accounting for a jump in phase shift; (bottom) phase shift against distance r^* , normalized with respect to the diffusion length. In the vicinity of the injection well diffusion dominates (red domain). For larger distances diffusion and inverse response coexist (gray domain). At larger distances, transient pressure is a response to hydro-mechanical coupling only (blue domain).

($r^* \sim 0 \dots 0.025$), phase shift is related to the diffusing pressure signal only. Phase shift values of either numerical approach and the analytical solution are comparable. Further away ($r^* \sim 0.025 \dots 0.01$), hydro-mechanical coupling effects become larger and affect the phase shift values. In this region of the fracture, measured phase shifts are the result of the sum of both diffusion and hydro-mechanical processes, which are characterized by the same frequency. In the vicinity of $r^* \sim 0.09$ (at $r \sim 90$ m), as diffusion effects vanish, very fast pressure variations in the first period of pumping become visible. At $r^* \sim 0.09$, during the data post processing, these effects are captured by the FFT analysis and a jump of one cycle occurs in the phase values. With increasing distance from the injection borehole ($r^* \geq 0.01$) phase shift values are related to the hydro-mechanical response only and converge to $\Delta\varphi \sim 0.69$.

Influence of pumping period on phase shifts and amplitude ratios

Results of the diffusion-based approach lie near the analytical solution of radial flow, independent of the pumping period T (Figure 4.9, top). In contrast, solutions of the fully coupled problem depend on the applied period T and are not restricted to characteristic lines in the dimensionless amplitude-ratio phase-shift domain (Figure 4.9, bottom). Different pumping periods trigger different pressure profiles along the fracture, characterized by distinct diffusion lengths. For $T = 37$ s, pressure penetration depth along the fracture is smaller than for $T = 370$ or $T = 3700$ s. The region dominated by diffusion is also small. Therefore, the domain characterized by inverse response begins closer to the injection borehole in comparison to large period injections, cf. Figure 4.9 (bottom).

The relative sizes of the three domains of Figure 4.8 (bottom) vary depending on the diffusion characteristics as well as on the hydro-mechanical coupling effects. Phase shifts and amplitude ratio values for all pumping periods follow the same pattern as in Figure 4.8 (bottom) but, depending on pumping period T , phase shift values converge to the pure hydro-mechanical response closer to or farther from the injection well. For small pumping periods, amplitude reduction is large and phase shifts at the monitoring wells converge near to the injection point. For $T = 37$ s, the phase shift induced by inverse response occurs at $r = 90$ m and is $\Delta\varphi \sim 0.69$. Phase shift induced by inverse response only is quantitatively equal to the one obtained with pumping period $T = 370$ s (Figure 4.8), with the difference that for $T = 370$ s convergence of $\Delta\varphi$ occurs at $r = 120$ m.

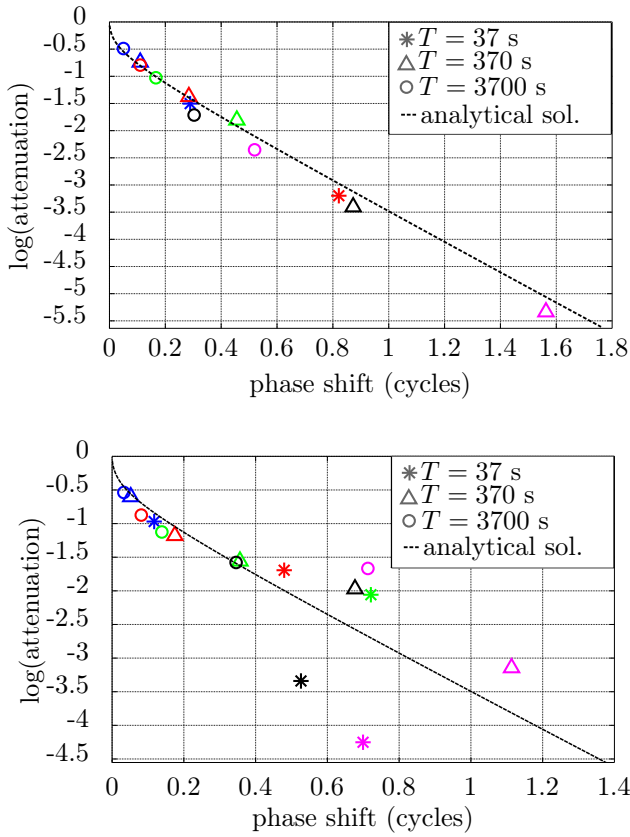


Figure 4.9: Amplitude ratio vs. phase shift at monitoring boreholes at positions $r = 5$ m (blue), $r = 15$ m (red), $r = 25$ m (green), $r = 50$ m (black), and $r = 90$ m (magenta) for different pumping periods ($T = 37, 370$, and 3700 s), obtained with (top) the diffusion-based approach and (bottom) the hybrid-dimensional approach.

4.4 Discussion

Periodic pumping tests and, in particular, interference analysis of the pressure transients are useful procedures to analyze pressure transport processes along a deformable conduit. In addition to geometrical and material properties, pumping protocol strongly affects to which extent hydraulic and mechanical processes are activated. Inverse response to pumping, for example, only occurs when flux at the injection well is changed. Application of a periodic signal at the injection well replicates inverse response various times for each cycle. Hydro-mechanical effects can easily be perceived by direct comparison of pressure values obtained with the hybrid-dimensional approach to diffusion-based results in the time domain (Figure 4.4). Analysis of data in the time domain provides further insight in the quantitative evaluation of hydro-mechanics.

By means of signal analysis procedures, the periodicity of the pressure signals was exploited. Fast Fourier transform analysis was used to analyze pressure transients up to small responses, which could not be discerned by analyzing the signals in the time domain. In the amplitude-ratio phase-shift domain, results from parametric sweep or from different models can be easily visualized and compared.

4.4.1 Mechanical response of the fracture

The pressure profiles provided by the hybrid-dimensional approach are asymmetric (Figure 4.4), in particular at $r = r_w$. During injection, smaller pressure variations occur in comparison to the production phase. The fracture appears to respond mechanically in different ways during injection and production, due to the non-local property of deformation. For positive fracture deformations (during pressure increase), the fracture appears less stiff than for diminishing fracture aperture. A similar asymmetry is evident also in records of field experiments [75].

Asymmetry in pressure profiles does not seem to be related to fracture geometry, it is rather connected to the presence of hydro-mechanical coupling effects. When fracture transmissivity is high and pressure distribution during injection is constant along the fracture, asymmetry in the pressure transient does not appear. Asymmetry only occurs if hydro-mechanical effects take place, e.g., inverse response, which occurs in thin fractures. Unlike pressure diffusion in a rigid conduit, hydro-mechanical effects seem to occur in different ways when injection or production is performed. During injection, hydro-mechanical coupling effects are larger than during production. As a result of the increased storage in the injection phase, occurring pressure variations are smaller in comparison to the production phase.

4.4.2 Hydro-mechanically induced phase shift

At large distances from the injection well, pressure oscillations are induced by fracture deformation only. At first glance, the inverse response suggests a phase shift $\Delta\varphi = 0.5$, opposite to the phase of the pressure at the injection well. As a result of the non-local property of deformation, inverse response effects are however of opposite phase at each position r . Any pressure acting on the fracture surface causes deformation at all points in the fracture domain. The phase shift $\Delta\varphi \sim 0.69$ of pressure oscillations caused by inverse response results from the sum of phase shifts $\Delta\varphi_i$ of pressure values acting at all points in the fracture, weighted by pressure amplitude and distance. For the limit case of an incompressible fluid, pressure diffusion is instantaneous and phase shift induced by inverse response is $\Delta\varphi = 0.5$. Further analyses can provide understanding of the relation of the hydro-mechanically induced phase shift to geometrical characteristics of the fracture as well as to material parameters of the solid rock and of the fluid.

4.4.3 Quantification of hydro-mechanical coupling

The storage multiplier is a quantitative index of the storage capacity of the fracture related to fracture deformation (Figure 4.6). For $\alpha_s = 1$, only storage related to fluid compressibility is accounted for. Higher values of α_s characterize soft and thin fractures, which deform easily and for which deformation is relatively large with respect to the initial aperture. For this configuration, the fracture-storage capacity is several orders of magnitude larger than storage deriving from fluid compressibility alone. On the contrary, stiff fractures with large apertures are characterized by a low storage capacity. Nevertheless, for a relatively wide fracture, e.g., $\delta = 5$ mm, in a relatively stiff rock, e.g., with a drained modulus of $K_d = 250$ GPa, the storage multiplier $\alpha_s \sim 10^4$ suggests that effects other than diffusion cannot be neglected. While specific investigation of wide fractures is not the scope of this work, by means of dimensional analysis (cf. Section 3.3.2) it was shown that phenomena other than diffusion or hydro-mechanical coupling dominate for configurations involving rigid and/or wide fractures and fluids other than water.

On the one hand, the expanded diffusion-based approach represents a useful tool to approximate hydro-mechanics in deformable conduits. On the other hand, reducing the fracture-storage capacity to a single value representing the entire domain is a strong assumption. By means of the diffusion-based approach, only the pressure transient at the injection well can be fitted (Figure 4.4). Hydro-mechanical effects caused by spatial and temporal changes of the fracture-storage capacity, e.g., inverse-pressure response, are neglected and pressure transients at monitoring boreholes cannot be matched. With this observation in mind, particular caution is needed for practitioners, for example in relation to induced seismicity analyses, when a diffusion-based approach is used to model the pressure records from a single well. While numerical results

from a diffusion-based approach match fairly well the signal at the injection borehole, predictions may totally fail regarding the pressure distribution in the subsurface.

4.4.4 Influence of pumping period on hydro-mechanics

Numerical results obtained with the hybrid-dimensional approach in the amplitude-ratio phase-shift domain depend on the chosen pumping period (Figure 4.9, bottom). Results obtained at monitoring points near the injection well lie near diffusion-based solutions. At intermediate distances, pressure oscillations caused by diffusion start to fade. The inverse-pressure response effect increases in importance and results in the amplitude-ratio phase-shift domain deviate from the analytical solution. At distances exceeding the pressure penetration depth associated with diffusion, pressure oscillations are uniquely triggered by hydro-mechanical coupling.

Based on the three regions (Figure 4.8, bottom), characteristic patterns of phase shifts and amplitude ratio values characterize the fully coupled results. The relative size of the characteristic domains depends on the pressure penetration depth along the fracture and, therefore, on the pumping period. Accounting for the fractures with identical geometrical and material properties, a larger or smaller pumping period results in a larger or smaller domain along the conduit, which is dominated by diffusion. Deviation from the analytical solution or convergence to a phase shift value occur differently depending on T (Figure 4.9, bottom).

Whereas the position in the fracture where diffusion vanishes depends on the pumping period, the value to which phase shifts converge seems to be independent of T . For both, $T = 37$ s and $T = 370$ s, $\Delta\varphi$ converges to $\Delta\varphi \sim 0.69$ (Figure 4.8, top, Figure 4.9, bottom). For $T = 3700$ s, pressure penetration depth caused by diffusion is larger than the monitored distances and the region dominated by inverse response only is not captured by the numerical results.

4.5 Conclusions

Understanding the role of hydro-mechanics is essential for the interpretation of pressure transients during well testing. Periodic pumping tests were simulated considering a vertical injection well intersecting a single horizontal deformable fracture. Pressure transients along the fracture were monitored at the injection point as well as at monitoring boreholes positioned along the fracture domain. Modeling was addressed using two methods, the hybrid-dimensional approach and the diffusion-based approach. To illustrate the relevance of hydro-mechanical coupling for flow in a deformable conduit, results of coupled models were investigated and compared to non-coupled models and analytical solutions. The diffusion-based approach, which is based on a simpli-

fied storage capacity concept, fails to capture the hydro-mechanical response of the fracture and fits the hydro-mechanical results only at a single point at a time. Analyses of results were performed in the time domain, but extensive comparison and post processing was evaluated in the frequency domain using FFT. Phase shifts and amplitude ratios between pressure signals at the monitoring and injection points were used to analyze and compare the numerical results.

Results indicate that hydro-mechanical effects strongly affect the pressure transient, in particular at large monitoring distances in comparison to the penetration depth of diffusion. A prominent evidence of the importance of hydro-mechanical effects is described by the concept of inverse-pressure response to pumping. With increasing distance, phase shifts and amplitude ratio values deviate from diffusion-based analytical solutions and phase shifts converge to constant values, caused by inverse response only. Unlike for simple diffusion, the behavior of the results of the coupled problem in the amplitude-ratio phase-shift domain depends on the pumping period, which affects the pressure penetration depth from the injection well along the fracture domain. Using the hybrid-dimensional approach, it was shown that pressure transients in a deformable conduit strongly depend on the initial fracture aperture and, for small apertures, also greatly rest on the stiffness of the surrounding material. Hydro-mechanical effects are more important for soft fractures and for conduits with high aspect ratios.

Chapter 5

On attenuation associated with fracture flow

5.1 Introduction

Characterization of heterogeneous materials can be performed by means of effective properties related to a homogeneous, continuous medium. With the modeling tools derived in the former chapters, investigations of heterogeneous materials and the related physical processes that occur within their domains can be efficiently performed. Sensitivity analyses with respect to geometrical and material parameters allow for interpretation of transient responses of the analyzed domains and, therefore, to characterization of their effective properties. Following, a unit cell is analyzed where solid to fluid coupling is induced. Deformations applied on the solid domain induce fluid fluxes within fluid-filled conduits that are embedded in the unit cell.

Acoustic waves propagating in fluid saturated rocks are attenuated by a number of mechanism, for example local fluid flow related to inhomogeneity in the pore space [55, 59]. Inhomogeneous distributions of rock-matrix properties as well as of hydraulic properties induce heterogeneous effective stresses and fluid pressure distribution, causing fluid flow on the length scale of the heterogeneities. In a fractured material, fluid flow/redistribution may occur in a single conduit or between conduits when the material volume is stressed [83, 84].

Real rocks comprise voids of vastly different geometry. Often the term *pore* is reserved for isometric voids on grain scale. The term *fracture* is used to address a second prototype of void that typically has one dimension falling significantly short of the other two, i.e., fractures constitute elongated features with a high aspect ratio, i.e., the longest dimension is several orders of magnitude larger than the shortest dimension. Their long dimension can vary from grain scale to way beyond it. In the current terminology, the term *fracture*

flow identifies the attenuation that is related to fluid flow along thin inclusions only. The term *attenuation* identifies the loss of energy dissipated by flow mechanisms.

The term *squirt flow* [1, 22, 32, 58] denotes local flow of a viscous fluid in individual cracks or between single grains, extending Biot's approach and related attenuation mechanisms. Pressure diffusion and resulting viscous attenuation induced by local flow or squirt-type mechanisms have been analyzed at a scale related to the characteristic length of the conduits for low-aspect ratio geometries [13, 41, 72, 83], i.e., the ratio of length and aperture is $2a/\delta < 10^3$. Natural or stimulated fractures in reservoir rocks exhibit large aspect ratios and resemble thin and elongated inclusions rather than isometric pores. The physics of attenuation due to fluid flow in such high-aspect ratio conduits have not been investigated yet.

Following, fluid flow is numerically investigated that is induced by elastic deformation of inclusions that are much larger than the average pore size of a porous rock. A two-dimensional prototype cell is employed that comprises two fractures intersecting each other at a normal angle, hosted in a homogeneous porous matrix. The numerical implementation allows one to independently study the effects of flow within a fracture, between fractures, and between fractures and porous matrix, often addressed as leak-off. The dissipative flow mechanisms lead to time dependence of the deformation. The different mechanisms are actually associated with characteristic times varying with the properties of pores and fractures. The observed deformation evolution is quantified by the frequency dependence of inverse quality factors, i.e., measures for attenuation. An improved understanding of the role of attenuation due to flow in fractures with realistic aspect ratios provides new directions for the interpretation of field data, for example estimation of fracture parameters from seismic data [4], or analysis of fracture connectivity [10, 73, 83].

5.2 Modeling approach

A simple two-dimensional unit cell is analyzed that consists of a fractured poro-elastic rock sample with two intersecting elliptical fractures [73, 82, 83]. The porous rock matrix and the conduit are saturated with a compressible, viscous pore fluid (dynamic viscosity $\eta^f R$ and compressibility β_f , Table 5.1). In contrast to previous investigations [e.g., 82, 83], the hydro-mechanical phenomena are investigated for high-aspect-ratio features, i.e., $\delta_h, \delta_v \ll L$ (Figure 5.1). The half length $a = 5$ cm applies for both fractures and the unit cell size is $L = 2.2 a$. The length of the fracture is approximately two orders of magnitude larger than the typical length scale of the pores in the matrix. The horizontal and vertical fractures are modeled as an ellipse and as a half ellipse, respectively. The vertical fracture intersects the horizontal one at its center.

Uniaxial compression is imposed by a vertical displacement boundary condition $\bar{u}_y = 10^{-3} L$ applied at the top edge of the unit cell. The displacement

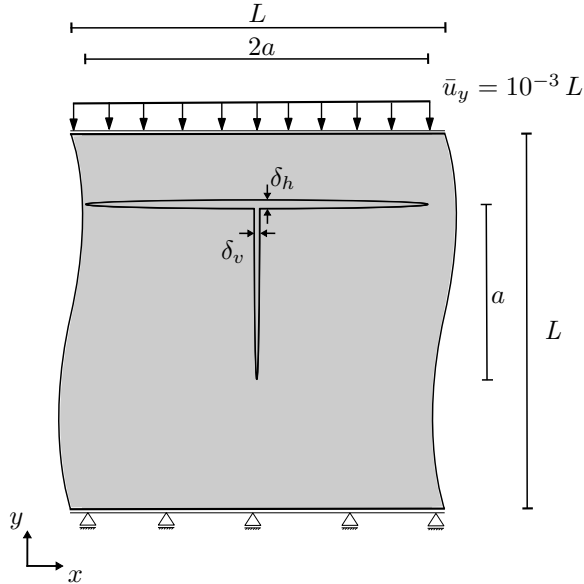


Figure 5.1: Geometry of the unit cell: two-dimensional poro-elastic rock containing two interconnected fractures. Displacement \bar{u}_y is imposed on the top edge. The bottom edge is constrained with respect to vertical displacement and is undrained ($q = 0$). At the left and right edges periodic boundary conditions are applied with respect to both, horizontal displacements and fluid flux.

boundary condition is enforced linearly in a time span $t_{\text{appl}} = 10^{-8}$ s while the total simulation interval is $t = [0, 10^8]$ s. Vertical displacements are fixed on the lower edge. In addition, no-flux boundary conditions are applied on the top and bottom edge. Furthermore, periodic boundary conditions are used for the pore pressure and the solid displacements on the left and right edge of the unit cell [48].

Through hydro-mechanical coupling, the deformation-induced pressure gradients trigger fluid flow phenomena within the conduits and leak-off from the conduits towards the surrounding porous rock, causing effective attenuation in the investigated rock sample. The vertical compression of the horizontal fracture induces fluid flow into the vertical one. Fluid flow along the fractures is affected by the fracture transmissivity as well as by deformation of the conduit through hydro-mechanical coupling effects [98]. Leak-off of fluid towards the matrix is controlled by the permeability of the surrounding rock.

Hydro-mechanical coupling in the rock domain of the unit cell is studied solving Biot's quasi-static poro-elastic equations (2.4), (2.6) [12]. To solve the time-dependent set of poro-elastic equations, the quasi-static Finite Element Method (FEM) is used in a displacement-pressure formulation [e.g., 71, 105]. Since this investigation focuses on fractured poro-elastic domains, the poro-

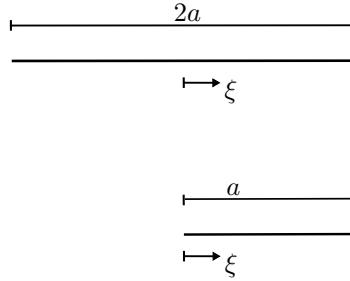


Figure 5.2: One-dimensional domains of the two interconnected fractures: (top) horizontal fracture; (bottom) vertical fracture.

elastic modeling framework is extended by the previously presented hybrid-dimensional approach [98] that allows for an efficient numerical solution of hydro-mechanical, coupled problems of fluid-filled fractures with large aspect ratios, i.e., $2a/\delta > 10^3$. The viscous fluid flow in the deformable conduits is accounted for by a one-dimensional approach leading to the governing equation

$$\begin{aligned} \frac{\partial p}{\partial t} + \frac{1}{12\eta^{\text{fR}}} \frac{\partial}{\partial \xi} \left(-\frac{\delta_i^2}{\beta^{\text{f}}} \frac{\partial p}{\partial \xi} \right) - \left(\frac{\delta_i}{12\eta^{\text{fR}}\beta^{\text{f}}} \frac{\partial \delta_i}{\partial \xi} \right) \frac{\partial p}{\partial \xi} \\ - \frac{\delta_i^2}{12\eta^{\text{fR}}} \left(\frac{\partial p}{\partial \xi} \right)^2 = -\frac{1}{\beta^{\text{f}}\delta_i} \frac{\partial \delta}{\partial t} + q_{\text{L}}, \end{aligned} \quad (5.1)$$

where δ_i with $i \in \{h, v\}$ represents the aperture of the fracture in the analyzed unit cell with local coordinate ξ , cf. Figures 5.1, 5.2. The apertures $\delta_i(\xi, t)$ and the fluid pressure $p(\xi, t)$ are evaluated with the poro-elastic equations (2.4), (2.6) and equation (5.1), respectively, and are used as coupling variables between the one-dimensional fracture flow process and the two-dimensional poro-elastic problem. The modeling equation (5.1) comprises, in order from left to right, a transient term, a diffusion, a nozzle (convection), a quadratic, and a hydro-mechanical coupling term. The source term q_{L} accounts for mass exchange between the fracture volume and the poro-elastic domain, induced by leak-off effects. In the performed simulations, the influence of the quadratic, i.e., nonlinear, term remains negligible and is therefore not further discussed in the numerical approach.

In each discrete time step of the numerical simulation, total and effective stresses, fluid pressure, displacements, and seepage velocities are calculated inside the unit cell. Following the methodology described in [71], volume averaged stresses and strain rates are calculated in a post-processing step and, applying Fourier transform, the complex vertical stiffness $M(f) = \bar{\sigma}_{yy}/\bar{\varepsilon}_{s,yy}$ relates the Fourier-transformed averaged total stress $\bar{\sigma}_{yy}(f)$ to the Fourier-transformed averaged strain $\bar{\varepsilon}_{s,yy}(f)$ of the rock matrix [68]. The inverse quality factor $Q^{-1} := \text{Im}(M)/\text{Re}(M)$ is evaluated to describe the characteristics of the dissi-

pative effects in a compact way. The frequency-dependence of complex stiffness $M(f)$, and of $Q(f)$, allows one to analyze the characteristic frequencies f_c , i.e., frequencies where intrinsic attenuation Q^{-1} has peaks (inverse characteristic relaxation times).

The numerical results are first obtained analyzing a unit cell with moderate aspect ratios to qualitatively validate the hybrid-dimensional approach coupled with the poro-elastic approach. Thus, three cases are investigated: a) fracture flow in an impermeable elastic rock, b) leak-off from undeformable fractures and permeable poro-elastic rocks, and c) fracture flow coupled with leak-off from deformable fractures and poro-elastic rocks. The obtained results are compared to the ones presented by Rubino et al. [83]. The maximum initial aperture of the vertical fracture is $\delta_v = 10 \mu\text{m}$. The resulting aspect ratio is $AR = 2a/\delta_v = 10^4$, Rubino et al. [83] analyzed moderate ratios $AR \approx 800$. In case a), an impermeable rock is analyzed, therefore an artificially small permeability $k_s = 10^{-30} \text{ m}^2$ is chosen, cf. material and geometrical parameters in Table 5.1. As a consequence, only fracture flow takes place, leading to a single attenuation process resulting in an inverse quality factor with a single maximum at characteristic frequency $f_{c,\text{ff}} \sim 10^2 \text{ Hz}$ (Figure 5.3). In the following, this frequency is denoted as the characteristic frequency of fracture flow. This characteristic frequency depends on fracture transmissivity, cf. [83], as well as on fracture stiffness [98]. In comparison to deformable conduits, fluid flow through stiff fractures results in a faster pressure-redistribution process, which is related to a higher characteristic frequency.

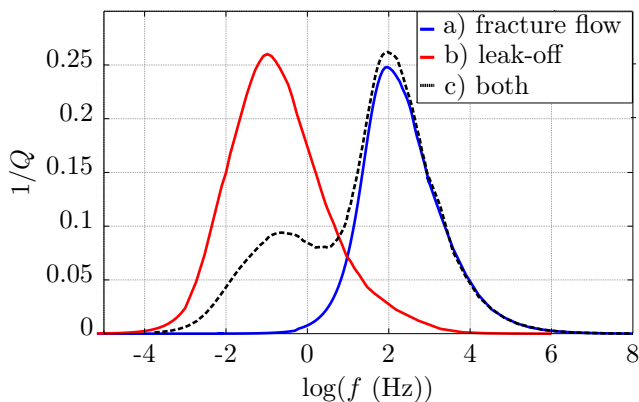


Figure 5.3: Inverse quality factor for a) fracture flow (blue line, $k_s = 10^{-30} \text{ m}^2$), b) leak-off only (red line, $k_s = 10^{-18} \text{ m}^2$, undeformable fractures), and c) for both processes (black dashed line).

In case b), undeformable fractures, i.e., with $\delta_v(t) = \text{const.}$ and, therefore $\partial\delta_v/\partial t = 0$, are analyzed that are embedded in a weakly permeable rock with

$k^s = 10^{-18} \text{ m}^2$. Leak-off of fluid from the fractures in the porous matrix constitutes the only remaining attenuation process. The characteristic frequency of leak-off $f_{c,lo}$ depends on matrix permeability k^s of the surrounding rock [e.g., 83]. The absolute values of peak attenuation $1/Q$ for fracture flow and leak-off are comparable, though with different characteristic frequencies (Figure 5.3).

For case c), deformable fractures are investigated in a permeable poro-elastic rock, thus both formerly mentioned attenuation phenomena occur. The two extreme values in the inverse quality factor are related to the characteristic frequencies of the occurring phenomena. An analysis of the behavior of the inverse quality factor in the frequency region between the peaks is presented in Section 5.3.5.

5.3 Results

5.3.1 Influence of aspect ratio on attenuation

For some combinations of fracture transmissivity, fracture stiffness, and rock permeability, attenuation due to fracture flow is quantitatively similar or larger than attenuation occurring at the pore scale. To concentrate on the physics of attenuation caused by fracture flow in thin conduits, leak-off is neglected ($k^s = 10^{-30} \text{ m}^2$). The aperture of the vertical fracture is varied from $\delta_v = 5 \text{ }\mu\text{m}$ to $\delta_v = 500 \text{ }\mu\text{m}$, resulting in aspect ratios $AR = 2 \times 10^4$ and $AR = 2 \times 10^2$, respectively. The lower the aperture δ_v the lower the characteristic frequency $f_{c,ff}$, cf. Figure 5.4. For high-aspect-ratio fractures attenuation induced by fracture flow is observed at seismic frequencies ($f < 10^2 \text{ Hz}$). Increasing aspect ratio, attenuation related to fracture flow increases too (Figure 5.4).

5.3.2 Influence of fracture deformation on attenuation

Fracture flow is intrinsically related to fracture deformation and consequently hydro-mechanical coupling. Comparing an undeformable fracture to an investigation including hydro-mechanical coupling, the flow process along the deformable fracture results in a faster attenuation process involving less fluid mass (Figure 5.5). For the chosen geometrical and material properties (Table 5.1 with $\delta_v = 10 \text{ }\mu\text{m}$), the characteristic frequency of fluid flow in an undeformable fracture is approximately two orders of magnitude higher than the one for a deformable fracture. Deformable fractures cause attenuation that exceeds the one associated with undeformable fractures by two orders of magnitude (Figure 5.5).

5.3.3 Characteristic frequencies and amplitudes

Modeling fracture flow with a simple diffusion equation overestimates the characteristic frequency and underestimates the amplitude of $1/Q$ by various orders

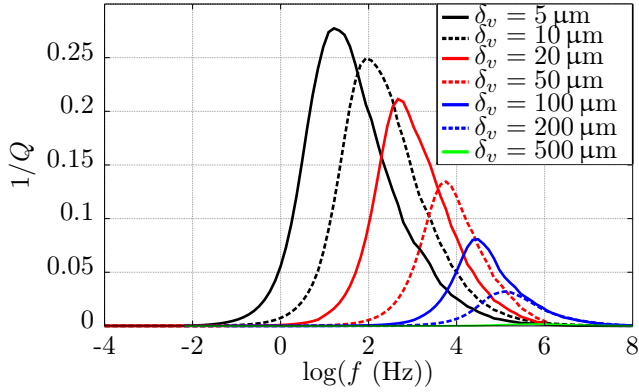


Figure 5.4: Effect of vertical fracture aperture δ_v on characteristic frequency and attenuation. Inverse quality factor $1/Q$ for fracture flow only. Sweep over different apertures $\delta_v = 5$ to $500 \mu\text{m}$, impermeable matrix.

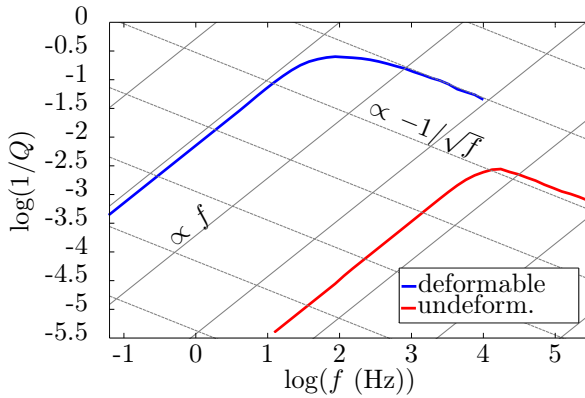


Figure 5.5: Inverse quality factor for a deformable (blue line) and an undeformable (red line) vertical fracture in an impermeable rock matrix. Vertical fracture aperture $\delta_v = 10 \mu\text{m}$, approximated by $k^s = 10^{-30} \text{m}^2$.

of magnitude, cf. Figures 5.5-5.7. The characteristic frequency $f_{c,\text{ff}}$ relates fracture flow to a characteristic diffusion time $t_{c,\text{ff}}$. Due to the hydro-mechanical coupling effects on fluid transport, $t_{c,\text{ff}}$ cannot be estimated from the scaling relation for a simple diffusion process [23]. The governing equation (5.1) covers physical processes beyond diffusion. The characteristic frequency of fracture flow $f_{c,\text{ff}}$ is compared with results of a simple diffusion model and with estimations proposed by Rubino & Holliger [82] and Gurevich et al. [42], for different aspect ratios ($\delta_v = 5 \dots 500 \mu\text{m}$), cf. Figure 5.6. On the one hand,

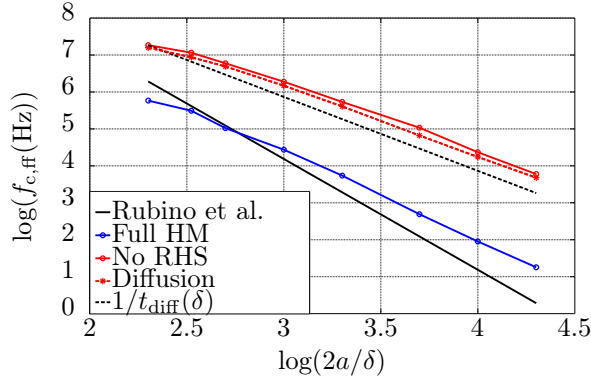


Figure 5.6: Characteristic frequencies for different values of dimensionless parameter $\log(2a/\delta_v)$ (sweep for $\delta_v = 5$ to $500 \mu\text{m}$, impermeable matrix) for the full hydro-mechanical coupled problem (blue line), neglecting coupling effects (red line), and assuming simple diffusion (red dashed line). Characteristic frequencies from simple diffusion time (black dashed line) and estimated fracture flow characteristic frequencies proposed by Gurevich et al. [42], Rubino & Holliger [82] (black line).

characteristic frequencies obtained for different aspect ratios lie near the predicted frequencies presented by Gurevich et al. [42], Rubino & Holliger [82] for apertures $\delta_v \sim 10^{-4}$ m. For smaller apertures, the estimated and the calculated frequencies diverge, but remain in the same order of magnitude. On the other hand, the characteristic time for pressure diffusion in the fracture $t_{\text{diff}} = (2a)^2/D$, where hydraulic diffusivity $D = \delta^2/(12\eta^{\text{fR}}\beta_{\text{f}})$, does not allow for estimation of $t_{\text{c,ff}}$ or finally $f_{\text{c,ff}}$.

Nevertheless, the true characteristic frequency can be approximately matched by a diffusion-based approach (cf. Section 2.3.2). A simple diffusion equation governing fluid flow along a fracture is obtained [76] in the form

$$s_{\text{F}} \frac{\partial p}{\partial t} - \frac{\delta_v^2}{12\eta^{\text{fR}}} \frac{\partial^2 p}{\partial \xi^2} = 0, \quad (5.2)$$

where s_{F} represents the specific fracture storage capacity [76]. For planar conduits the specific storage capacity $s_{\text{F}} = \beta_{\text{f}} + \partial \ln \delta_v / \partial p$ has two contributions [65, 66, 76], one deriving from the fluid compressibility β_{f} and one from relative changes in fracture aperture δ_v caused by pressure variations. Here, the contribution due to aperture changes are expressed by parametrization of the storage capacity $s_{\text{F}} = \alpha_s \beta_{\text{f}}$ in multiples of the fluid compressibility. Storage is entirely accounted for by a single macroscopic storage capacity. The larger the storage deriving from hydro-mechanical coupling, the larger the factor α_s .

Choosing α_s appropriately the characteristic frequencies observed for full hydro-mechanical coupling can be matched by modeling calculations based on

Table 5.1: Material parameters applied in the numerical investigation.

Domain	Parameter	
Fractures	$a = 5$ cm	
	$\bar{u}_y = L \times 10^{-3}$ m	
	$\delta_h(t_0) = 100$ μm	
	$\delta_v(t_0) = 5 \dots 500$ μm	
Surrounding rock	$K^s = 36$ GPa	grain
	$K_d = 16$ GPa	skeleton
	$G = 16$ GPa	skeleton
	$K^f = 2.3$ GPa	fluid
	$\phi = 0.01$	
	$k^s = 10^{-30}$ m ²	impermeable
	$k^s = 10^{-18}$ m ²	permeable

the diffusion equation (5.2). The relation between fracture aperture δ_v and α_s is well approximated with the power law $\alpha_s \approx \delta^{-1.1} c_1$, where c_1 is a generic constant that depends on the chosen material and geometrical parameters. By means of this relation, experimental data of attenuation characteristics can be easily approximated with the diffusion equation (5.2) to obtain the value of α_s and finally an estimation of the geometrical properties of the analyzed rock domain.

While it was clearly pointed out in Section 5.3.2 that hydro-mechanical coupling is crucial when investigating attenuation in fractured poro-elastic domains, it is still open to which extent other terms in equation (5.1) affect the amplitude of the inverse quality factor as well as the characteristic frequency $f_{c,\text{ff}}$. In addition to the results obtained in case of coupled hydro-mechanical processes, numerical results are evaluated for an undeformable fracture. Neglecting hydro-mechanical coupling in the simulations, the characteristic frequencies shift towards the frequency values approximated by a simple diffusion model with s_F solely controlled by fluid compressibility, i.e., $s_F = 1$. The effects of the nonlinear, i.e., quadratic term in equation (5.1) can be neglected for the analyzed test cases. Furthermore, hydro-mechanical coupling, nonlinear effects, as well as nozzling term are neglected. The nozzling term is proportional to the pressure gradient as well as to the aperture gradient and is eliminated when modeling the vertical fracture with a rectangular shape, cf. Figure 5.8. The fracture flow process in the vertical conduit results in a simple transient diffusion process. The resulting characteristic frequencies are slightly lower than the ones obtained accounting for the nozzling term. The difference in attenuation between the hydro-mechanical problem and the undeformable fracture solution varies with the aperture δ_v , cf. Figure 5.7. The difference is large for smaller aperture values, and diminishes with increasing apertures δ_v .

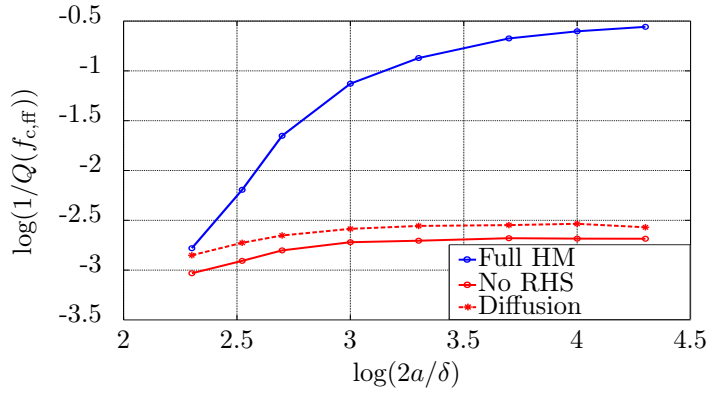


Figure 5.7: Comparison of full hydro-mechanical results, diffusion and convection, and simple diffusion: amplitude of $\log(1/Q)$ at the characteristic frequency $f_{c,ff}$ vs. dimensionless parameter $\log(2a/\delta_v)$.

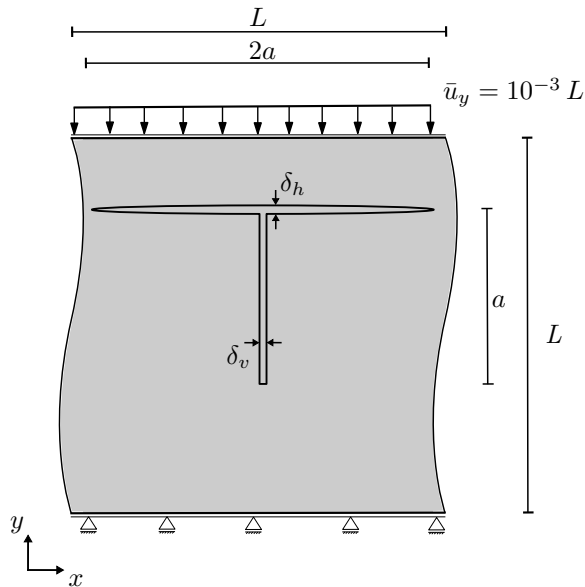


Figure 5.8: The vertical fracture is modeled with a rectangular geometry to neglect nozzling/convective effects.

5.3.4 Sensitivity of fracture flow to fracture intersection angle

Fracture flow in the vertical conduit is uniquely triggered by fluid mass exchange, induced from the horizontal fracture. The intersection point, as well as the intersection angle γ between the horizontal and the vertical fractures (Figure 5.9) are parameters that strongly affect the characteristics of fracture flow. Depending on the angle γ , different attenuation as well as characteristic fre-

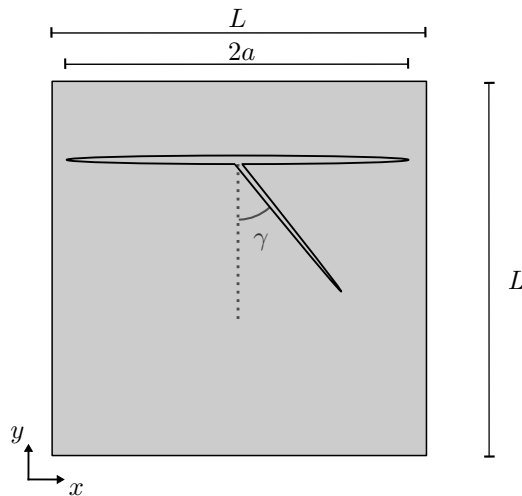


Figure 5.9: Vertical fracture intersecting the horizontal fracture with angle γ .

quency values are obtained, cf. Figure 5.10. The angle $\gamma = 0^\circ$ is assumed when the two fractures intersect orthogonally. For increasing values of γ , both, attenuation values decrease and reach their minimum value approaching $\gamma = 90^\circ$. For $\gamma = 90^\circ$, the two fractures degenerate to a single horizontal inclusion, thus no fracture flow is induced. Interestingly, for increasing values of γ , the critical frequency of fracture flow also decreases.

5.3.5 Slope of the inverse quality factor

The characteristic slopes of the inverse quality factor for pure diffusion [54] are well known. In the low-frequency limit, i.e., in the frequency range preceding the maximum value of the inverse quality factor, attenuation is proportional to the first power of f while in the high-frequency limit $1/Q \propto -f^{-1/2}$. However, when various transport processes take place simultaneously, the behavior of

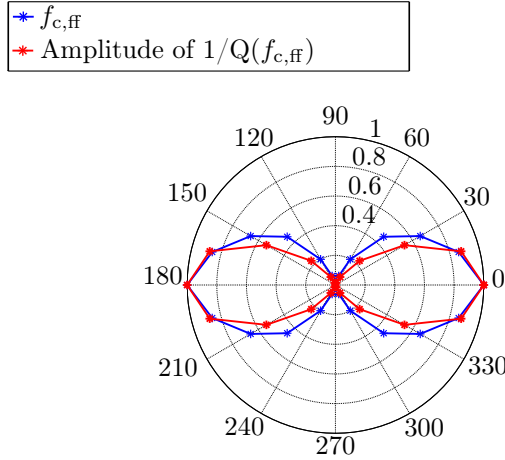


Figure 5.10: Polar plot of the normalized attenuation (red line) and characteristic frequencies $f_{c,ff}$ (blue line) for different intersecting angles $\alpha = 0 \dots 70^\circ$. A unit cell with $\delta_h = 100 \mu\text{m}$ and $\delta_v = 10 \mu\text{m}$ is analyzed.

attenuation, in particular in the frequency band between the maximum values, is not clearly understood. Investigations [14, 41] have proposed that for problems of superimposed attenuation effects different scaling laws apply, for example $1/Q \propto f^{1/2}$ in the intermediate frequency range, but this relation seems not to be universally valid. Following, attenuation is analyzed for 1) fracture flow only, 2) leak-off only, and 3) leak-off and fracture flow in a unit cell with $\delta_h = 100 \mu\text{m}$ and $\delta_v = 10 \mu\text{m}$ (for other parameters used see Table 5.1).

In case 1) an extreme configuration is represented, where an artificially impermeable rock ($k^s = 10^{-30} \text{m}^2$) is analyzed. Leak-off is neglected choosing an extremely low permeability value and only fluid flow along the vertical fracture occurs. Therefore, attenuation is characterized by a single maximum $f_{c,ff} \sim 10^2 \text{Hz}$, related to fracture flow. The inverse quality factor agrees with the characteristic behavior for pure diffusion at both, the low-frequency and high-frequency limits. In the low-frequency limit dimensionless attenuation $1/Q \propto f$ and is well approximated in a logarithmic plot by the generic line

$$\log \frac{1}{Q} = \log f + \log c_1. \quad (5.3)$$

In the high-frequency limit $1/Q \propto -f^{-1/2}$. This behavior is described by the line

$$\log \frac{1}{Q} = \log f^{-\frac{1}{2}} + \log c_2. \quad (5.4)$$

To maintain generality, the parameters c_1 and c_2 are not specified with numerical values and identify the intersection of the each line with the y-axis.

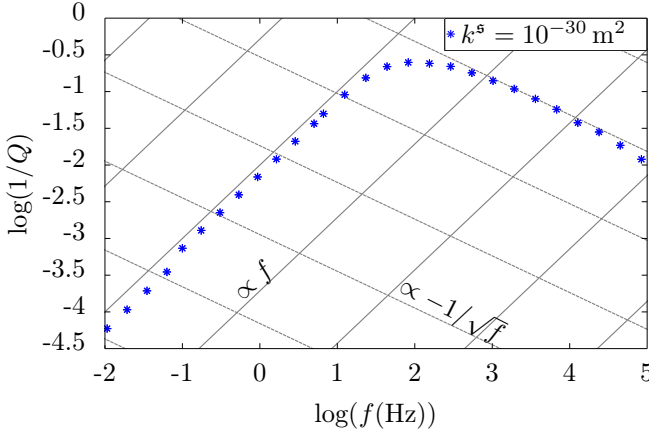


Figure 5.11: Dimensionless attenuation for an artificially impermeable rock ($k^s = 10^{-30} \text{ m}^2$). The low permeability inhibits leak-off effects and only fracture flow is induced. The single maximum of $1/Q$ is related to fracture flow. The slopes of $1/Q$ before and after the characteristic frequency $f_{c,\text{ff}}$ are proportional to f and $-f^{-1/2}$, respectively.

In case 2), a rock matrix is investigated, characterized by a permeability $k^s = 10^{-15} \text{ m}^2$. The diffusion time of leak-off is much larger than the one of fracture flow, therefore, attenuation exhibits one maximum value only, related to leak-off, cf. Figure 5.12. Pressure gradients generated by the displacement applied to the unit cell are dissipated by fluid flow through the porous rock alone. As in case 1), the behavior of the inverse quality factor can well be described in the low-frequency and high-frequency limits by means of equations (5.3) and (5.4), respectively.

For case 3), a weakly permeable rock matrix is analyzed, $k^s = 10^{-20} \text{ m}^2$. By decreasing the rock permeability, in comparison to case 1), the characteristic diffusion time for leak-off phenomena is increased, therefore, slower phenomena, as for example fracture flow, also take place. The two occurring phenomena, i.e., flow in the vertical fracture and leak-off, are characterized by the two extreme values of the inverse quality factor, cf. Figure 5.13. The characteristic frequency $f_{c,\text{lo}} \sim 10^{-3} \text{ Hz}$ is smaller compared to $f_{c,\text{lo}}$ in case 2), due to the reduced intrinsic permeability k^s . The second extreme value of attenuation is $f_{c,\text{ff}} \sim 10^2 \text{ Hz}$, related to fracture flow. The behavior of the inverse quality factor in the low-frequency, i.e., $f < f_{c,\text{lo}}$, and high-frequency limits, i.e., $f > f_{c,\text{ff}}$, is identical as in the former examples. Low-frequency and high-frequency limits are well described with equations (5.3) and (5.4), respectively.

In the frequency band between the local maxima, the behavior of attenuation results from the combination of the decreasing slope at $f > f_{c,\text{lo}}$ and the increasing slope for $f < f_{c,\text{ff}}$. The transition between two extreme values is

well described by the sum of equations (5.3) and (5.4), i.e.,

$$\log \frac{1}{Q} = \log f + \log f^{-\frac{1}{2}} + \log (c_1 c_2). \quad (5.5)$$

Depending on the hydraulic and material properties of the analyzed unit cell, the transition zone between two attenuation maxima varies in size and is the result of superimposing the decreasing trend and the increasing slope of the smaller and larger characteristic frequencies, respectively.

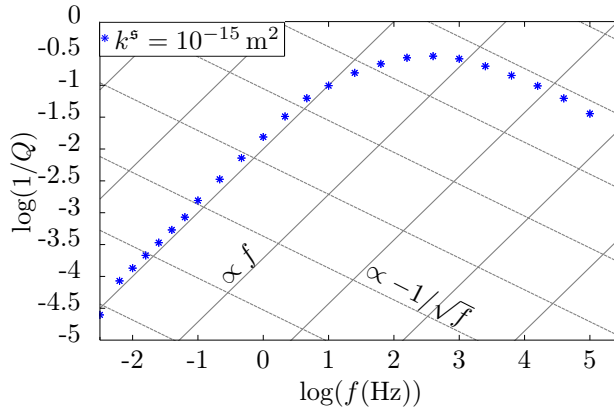


Figure 5.12: Dimensionless attenuation for a permeable rock ($k^s = 10^{-15} \text{ m}^2$). The relatively high permeability allows for a fast re-equilibration of induced pressure gradients and inhibits the development of fracture flow. The single maximum of $1/Q$ is related to leak-off. The slopes of $1/Q$ before and after the characteristic frequency $f_{c,10}$ are proportional to f and $-f^{-1/2}$, respectively.

5.4 Discussion

In all presented cases, a unit cell with interconnected fractures was investigated. Fracture deformation as well as fluid mass exchange between the fractures are essential for the investigation of deformation-induced fracture flow. In the investigated unit cell, the horizontal fracture has the role of a fluid storage domain. Thus, storage capacity is essential for fluid mass exchange and, therefore, for fracture flow in the vertical crack. The fractures were assumed to intersect orthogonally. Effects of variations in intersection angle are investigated in Section 5.3.4. If the two fractures do not intersect, the inter-fracture flow mechanism does not take place and attenuation is only related to local fracture flow phenomena. Fracture deformation still occurs but no fluid exchange takes place between the fractures. Attenuation related to fracture flow is negligible compared to leak-off effects [83].

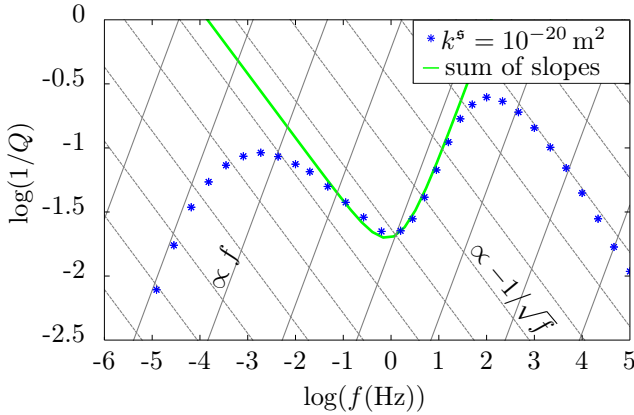


Figure 5.13: Dimensionless attenuation for leak-off and fracture flow. The characteristic frequencies of leak-off and fracture flow are $f_{c,lo} \sim 10^{-3}$ and $f_{c,ff} \sim 10^2$, respectively. The behavior of $1/Q$ in the intermediate frequency band is well described by the sum of decreasing trend for $f > f_{c,lo}$ and the increasing trend for $f < f_{c,ff}$.

In contrast, both, leak-off and fracture flow take place when mass exchange between the fractures is possible. Attenuation related to both processes varies with the fracture aperture δ_v and the intrinsic permeability k^s . The characteristic frequencies $f_{c,ff}$ and $f_{c,lo}$, at which the extreme values of attenuation occur, remain unaltered compared to their individual occurrence, meaning that the inherent time scales of fracture flow and leak-off do not influence each other (Figure 5.2). On the contrary, the maximum amount of attenuation related to leak-off is affected by the presence of fracture flow. In case c), where both, fracture flow and leak-off take place, fracture flow, depicted by the higher characteristic frequency, occurs over a shorter time interval than the leak-off process depicted by the lower characteristic frequency. The characteristic frequency $f_{c,lo}$ depends only on permeability of the surrounding rock. In this case, the higher the permeability of the surrounding rock, the faster the process. The characteristic frequency $f_{c,ff}$ mainly depends on the aperture of the fracture and, due to hydro-mechanical coupling effects, on the stiffness of the fracture; stiffness of the fracture is related to stiffness of the surrounding material or fracture storage capacity. The larger the aperture, the faster the flow process [98].

In comparison to case a), where only fracture flow occurs, the intrinsic permeability of the rock $k^s = 10^{-18} \text{ m}^2$ analyzed in case c) is large enough to allow us for leak-off to take place and small enough to allow to distinguish the two characteristic attenuation phenomena, depicted in the extreme values of the inverse quality factor. The chosen permeability value is realistic for

several crystalline basements. When fluid flow in the fracture and leak-off occur simultaneously, the former process only takes place if it occurs faster than leak-off. Pressure gradients generated by the induced deformation are first dissipated along the fracture by fluid flow and the remaining pressure gradients are dissipated by leak-off (smaller peak in leak-off in Figure 5.3). On the contrary, if $f_{c,lo} \gg f_{c,ff}$, i.e., in case of a high permeable surrounding rock matrix, all pressure inhomogeneities are dissipated by leak-off and fluid flow along the fracture is negligible.

Neglecting leak-off, it was shown that attenuation related to fracture flow increases in magnitude with increasing aspect ratio of the vertical fracture. Therefore, fracture flow attenuation effects are larger in domains containing high-aspect ratio inclusions, which better approximate the geometry of real fractures. Furthermore, accounting for hydro-mechanical coupling is crucial for a correct description of fracture flow.

For an undeformable fracture the transport phenomena in the vertical fracture are much faster in comparison to the hydro-mechanical coupled results. Thus, the characteristic frequency is larger when rigid fractures are investigated than for deformable fractures. Also, attenuation (amplitude of $1/Q$) is largely underestimated for rigid fractures in comparison to deformable fractures. For an undeformable fracture, specific storage capacity deriving from fracture deformation is neglected. For identical pressure variations, specific storage in an undeformable fracture is related to fluid compressibility only and, thus, less fluid mass is accommodated in comparison to a deformable fracture. A lower mass exchange between the horizontal and the vertical fractures results in a reduction of dimensionless attenuation (Figure 5.5). Attenuation differences between the hydro-mechanical problem and the undeformable fracture solution depend on the aperture δ_v , cf. Figure 5.7. Deviations are large for smaller aperture values, and diminish with increasing apertures δ_v , suggesting that, while hydro-mechanical coupling can be ignored for very wide fractures, it cannot be neglected when investigating high-aspect ratio inclusions.

5.5 Conclusions

Attenuation effects, i.e., loss of deformation energy, was investigated in a two-dimensional unit cell containing interconnected fractures embedded in a homogeneous poro-elastic matrix. The analyzed attenuation effects were related to fracture flow in the vertical fracture and leak-off of fluid from the fractures towards the surrounding rock. Fracture flow was induced by deformation of the horizontal fracture, which triggered fluid mass exchange between the horizontal and the vertical fracture. Using a hybrid-dimensional approach, particularly apt for large-aspect-ratio conduits, fluid flow in the fractures was modeled as a one-dimensional process, while description of the fluid flow at the pore scale was performed by means of the theory of poro-elasticity. Leak-off and fracture flow are related to distinct characteristic frequencies. The inherent time scales

of fracture flow and leak-off do not influence each other. On the contrary, the magnitude of attenuation for leak-off and fracture flow is affected by coupled processes. The faster process, i.e., the one with the higher characteristic frequency, dissipates the pressure gradients in the unit cell before the slower process could become active. Thus, the faster process is characterized by a higher value of attenuation than the slower process.

The contribution of fracture flow to attenuation in the seismic frequency range increases in magnitude for high-aspect ratio inclusions. To correctly account for fracture flow, hydro-mechanical coupling effects cannot be neglected. Simple diffusion problems largely overestimate the critical frequency of fracture flow. Furthermore, neglecting hydro-mechanical coupling, attenuation related to fracture flow is quantitatively underestimated. Deviation between attenuation values resulting from a simple diffusion model and a fully coupled one increases with increasing aspect ratio of the vertical fracture, thus suggesting that hydro-mechanical effects are crucial in investigations related to fluid flow along thin inclusion.

Conclusions

The scope of this work was to model and numerically investigate the flow of a compressible viscous fluid along a single compliant conduit, such as a joint or a fracture. Fractures typically have one dimension that is significantly smaller than the other two and are well represented by elongated geometries with a large aspect ratio. Though many investigations have been performed in this research area, this work focused on geometries characterized by a high-aspect-ratio, previously unexplored.

In Chapter 2, various modeling approaches were introduced with the objective to develop and test numerical methods for the hydro-mechanical modeling of fractured materials. To efficiently solve initial-boundary-value problems involving high-aspect-ratio geometries, the hybrid-dimensional approach was derived in Chapters 2 and 3. The hybrid-dimensional approach consists of a fully coupled set of equations derived from basic conservation laws for specific geometrical heterogeneities, i.e., a horizontal fracture modeled as an ellipsoid. This method is based on the reduction of the dimensions at which fluid flow in thin conduits is modeled. Two-dimensional axial symmetric models were analyzed, where the fluid flow along a single fracture was reduced to a one-dimensional axisymmetric process. This simplification allows to describe inclusions independent of their aspect ratio.

In Chapter 3 modeling equations as well as numerical results from the hybrid-dimensional approach were compared to the ones obtained using the well-known poro-elastic approach, considered to constitute a benchmark. Numerical results of the two approaches for a low-aspect ratio geometry were compared to validate the output of the newly developed methodology. Furthermore, by means of a dimensional analysis the role of different physical phenomena for differing model configurations was revealed. For high-aspect-ratio fractures filled with water, transport of fluid along the fracture is the results of diffusion and convection processes, together with transient effects due to hydro-mechanical coupling, specifically related to the deformation of the fracture induced by pressure variations. To understand the magnitude of hydro-mechanical coupling effects in real applications, field recordings related to well pumping experiments were modeled. The hybrid-dimensional approach quantitatively modeled the pressure transients obtained during the field experiments and successfully captured observations related to hydro-mechanical

coupling, i.e. inverse-pressure response. It was shown that neglecting the effects of fracture deformation yielded strongly different results.

Based on the material and geometrical properties obtained from fitting numerical results to field data, further investigations of the effects of hydro-mechanics in deformable fractures were performed in Chapter 4. For an efficient analysis of well tests, periodic pumping procedures were simulated. On the one hand, periodic variations of the applied boundary conditions stimulated the hydro-mechanical response of the fracture. On the other hand, application of a periodic signal as a boundary condition allowed for an extensive data analysis in the frequency domain by means of Fourier transform. The phase shift and attenuation of pressure signals between an injection well and several monitoring boreholes was analyzed. It was shown that the response of deformable fractures to fluid injection exhibits a complex pattern in the phase shift-attenuation domain, which cannot be approximated by simple diffusion-based approaches.

Effects related to hydro-mechanical coupling were also quantitatively investigated in the frequency domain for fluid flow induced by deformation, cf. Chapter 5. Attenuation effects in a unit cell containing interconnected fractures were investigated. Attenuation related to fracture flow as well as to leak-off was analyzed in relation to the characteristic time scales of each process. The behavior and the interaction between each fluid flow phenomenon was investigated. While the characteristic time scale is not affected, the magnitude of attenuation of each physical process is strongly affected by attenuation related to other occurring phenomena. This understanding allows for a better interpretation of field data and, therefore, for a more robust characterization of fractured rock domains. Furthermore, it was shown that attenuation due to flow induced along a fracture quantitatively increases with increasing aspect ratio of the analyzed fracture geometry, confirming the results of investigations presented in Chapter 4.

Various investigations for different configurations and domain sizes were performed. By means of a dimensional analysis, cf. Chapter 3, a general understanding of various physical processes was obtained. Fitting field data, cf. Chapter 3, investigating periodic pumping procedures, cf. Chapter 4, or analyzing deformation-induced attenuation phenomena, cf. Chapter 5, provided an insight in the hydro-mechanics of fluid flow through fractured material pointing in the same direction. Main findings of this thesis can be summarized by the following points:

- hydro-mechanical coupling effects become crucial when high-aspect-ratio geometries are investigated. As the aspect ratio increases, the hydro-mechanical coupling effects have a greater influence;
- neglecting hydro-mechanical coupling terms causes the numerical results to largely deviate from a correct estimation of flow processes and, therefore, provides a biased characterization of material and geometrical properties of fractured rock domains;

- some critical observations, e.g., the inverse pressure-response, can only be reproduced by means of modeling equations that not only account for coupling, but also specifically account for the non-local property of fracture deformation.

The hybrid-dimensional approach was developed to investigate hydro-mechanical effects in fractured rock as well as to provide simulation results that best reproduce the pressure transients in real fractured rock. The presented modeling approach represents a tool to constrain effective properties of fractured rocks. Geometrical properties of a single fracture and material parameters of the surrounding rock were obtained by fitting numerical results to field data, cf. Chapter 3. Fitting was performed adjusting the input parameters based on the sensitivity of the numerical results to geometrical and material parameters. By means of optimization techniques, numerical results can be fitted to field data with respect to various input variables to obtain an “ideal” set of geometrical and material parameters characterizing the fractured rock. Among others, a genetic algorithm can be used to minimize the deviation between numerical results and data recorded during field experiments. Genetic algorithms are gradient-free methods, meaning that the sensitivity of the pressure transient to input parameters is not needed. Therefore, this approach can be easily applied as an extension to this investigation. Adopting an automated fitting procedure, more complex scenarios can be simulated, in which various fractures with different characteristics are accounted for. Data fitting can be performed not only with respect to fracture geometry and rock parameters, but also with respect to fracture number, orientation, connectivity, and distribution.

A different equation governing fluid flow in the hybrid-dimensional approach should be derived, that accounts for flow in a vertical fracture. In the latter case, in addition to differences in fracture orientation and geometry, body forces related to gravity should not be neglected. Understanding the differences in equations governing fluid flow in a horizontal and in a vertical fracture, a unified modeling equation can be obtained that accounts for fracture inclination and correctly described the two extreme cases, i.e., horizontal or vertical fracture.

Finally, open fractures were investigated, where contact between asperities was neglected. The hybrid-dimensional approach can be extended to account fracture behavior after closure, that is when the first asperities from opposite fracture surfaces come in contact. When fractures with large contact areas are investigated, the cubic law might fail to correctly describe the fracture permeability. Exploration towards alternative formulations of fracture flow might be needed. Accounting for stresses and permeability changes induced by contact of fracture asperities provides a comprehensive model that captures more complex behavior of fracture deformation in comparison to the presented approach and, therefore, might lead to a better understanding of fracture flow and the related hydro-mechanical effects.

Bibliography

- [1] Adelinet, M., J. Fortin, and Y. Guégen, Dispersion of elastic moduli in a porous-cracked rock: Theoretical predictions for squirt-flow, *Tectonophysics*, 503(1-2):173–181, 2011.
- [2] Almtann, J., B. Müller, T. Müller, O. Heidbach, M. Tingay, and A. Weißhardt, Pore pressure stress coupling in 3D and consequences for reservoir stress states and fault reactivation, *Geothermics*, in press, 2014.
- [3] Bakhos, T., M. Cardiff, W. Barrash, and P. Kitanidis, Data processing for oscillatory pumping tests, *Journal of Hydrology*, 511(16):310–319, 2014.
- [4] Bakulin, A., V. Grechka, and I. Tsvankin, Estimation of fracture parameters from reflection seismic data-Part I: HTI model due to a single fracture set, *Geophysics*, 65(6):1788–1802, 2000.
- [5] Bandis, S., A. Lumsden, and N. Barton, Fundamentals of rock joint deformation, *International Journal of Rock Mechanics and Mining Sciences & Geomechanics Abstracts*, 20(6):249–268, 1983.
- [6] Barton, N., S. Bandis, and K. Bakhtar, Strength, deformation and conductivity coupling of rock joints, *International Journal of Rock Mechanics and Mining Sciences & Geomechanics Abstracts*, 22(3):121–140, 1985.
- [7] Batchelor, G., *An Introduction to Fluid Dynamics*, Cambridge University Press, 2000.
- [8] Bear, J., *Dynamics of fluids in porous media*, Dover Publications Inc., New York, 1988.
- [9] Berg, S. J., P. A. Hsieh, and W. A. Illman, Estimating hydraulic parameters when poroelastic effects are significant, *Ground Water*, 49(6): 815–829, 2011.
- [10] Berkowitz, B., O. Bour, P. Davy, and N. Odling, Scaling of fracture connectivity in geological formations, *Geophysical Research Letters*, 27 (14):2061–2064, 2000.

-
- [11] Bieniawski, T., *Engineering Rock Mass Classifications*, New York: Wiley, 1989.
- [12] Biot, M. A., General theory of three-dimensional consolidation, *Journal of Applied Physics*, 12:155–164, 1941.
- [13] Brajanovski, M., B. Gurevich, and M. Schoenberg, A model for P-wave attenuation and dispersion in a porous medium permeated by aligned fractures, *Geophysical Journal International*, 163:372–384, 2005.
- [14] Brajanovski, M., T. Müller, , and B. Gurevich, Characteristic frequencies of seismic attenuation due to wave-induced fluid flow in fractured porous media, *Geophysical Journal International*, 166:574–578, 2006.
- [15] Brodsky, E. E., E. Roeloffs, D. Woodcock, I. Gall, and M. Manga, A mechanism for sustained groundwater pressure changes induced by distant earthquakes, *Journal of Geophysical Research*, 108(2390), 2003.
- [16] Bronstein, I., K. Semendjajew, G. Musiol, and H. Mühlig, *Taschenbuch der Mathematik*, Harri Deutsch, 2000.
- [17] Butler, J. J., *The design, performance, and analysis of slug tests*, CRC Press LLC, 1997.
- [18] Cappa, F., Y. Guglielmi, J. Rutqvist, C.-F. Tsang, and A. Thoraval, Estimation of fracture flow parameters through numerical analysis of hydromechanical pressure pulses, *Water Resources Research*, 44(11): W11408, 2008.
- [19] Cardiff, M., T. Bakhos, P. Kitanidis, and W. Barrash, Aquifer heterogeneity characterization with oscillatory pumping: Sensitivity analysis and imaging potential, *Water Resources Research*, 49(9):5395–5410, 2013.
- [20] Cardiff, M., W. Barrash, and P. Kitanidis, Hydraulic conductivity imaging from 3-D transient hydraulic tomography at several pumping/observation densities, *Water Resources Research*, 49:7311–7326, 2013.
- [21] Carslaw, H., and J. Jaeger, The laplace transformation: Problems in linear flow, In *Conduction of Heat in Solids*, Oxford University Press, 1959.
- [22] Chapman, M., S. V. Zatsepin, and S. Crampin, Derivation of a microstructural poroelastic model, *Geophysical Journal International*, 151: 427–451, 2002.
- [23] Chapman, M., S. Maultzsch, and E. Liu, Estimating the squirt-flow frequency, In *65th EAGE Conference & Exhibition - Session Rock Physics - Theory*, EAGE, 2003.

- [24] Chen, S., and G. D. Doolen, Lattice Boltzmann method for fluid flow, *Annual Review of Fluid Mechanics*, 30:329 – 364, 1998.
- [25] Coussy, O., *Poromechanics*, John Wiley & Sons., 2004.
- [26] Daniel, D., *Geotechnical Practice for Waste Disposal*, Springer, 1993.
- [27] de Boer, R., *Theory of Porous Media*, Springer, 2000.
- [28] de Boer, R., *Trends in Continuum Mechanics of Porous Media*, Springer Netherlands, 2005.
- [29] Detournay, E., Propagation regimes of fluid-driven fractures in impermeable rocks, *International Journal of Geomechanics*, 4(1):35–45, 2004.
- [30] Detournay, E., and A.-D. Cheng, Fundamentals of poroelasticity, In *Comprehensive Rock Engineering: Principles, Practice and Projects*, Pergamon, 1995.
- [31] Doré, A., and R. Sindling-Larsen, *Quantification and Prediction of Hydrocarbon Resources*, Elsevier, 1996.
- [32] Dvorkin, J., and A. Nur, Dynamic poroelasticity: a unified model with the squirt and the Biot mechanisms, *Geophysics*, 58(4):524–533, 1993.
- [33] Ehlers, W., and J. Bluhm, *Porous Media: Theory, Experiments and Numerical Applications*, Springer, 2002.
- [34] Fetter, C., *Applied Hydrogeology*, Prentice Hall, Upper Saddle River, New Jersey, 2001.
- [35] Gassmann, F., Über die Elastizität poröser Medien, *Vierteljahresschrift der Naturforsch. Ges. Zürich*, 96:1–23, 1951.
- [36] Gellasch, C., H. Wang, K. Bradbury, J. Bahr, and L. Lande, Reverse water-level fluctuations associated with fracture connectivity, *Groundwater*, 52(1):105–117, 2014.
- [37] Gleeson, T., Y. Wada, M. Bierkens, and L. van Beek, Water balance of global aquifers revealed by groundwater footprint, *Nature*, 488:197–200, 2012.
- [38] Gonzalez, O., and A. M. Stuart. *A First Course in Continuum Mechanics*, Cambridge University Press, 2008.
- [39] Greve, R., *Kontinuumsmechanik: Ein Grundkurs für Ingenieure und Physiker*, Springer, 2003.
- [40] Guimera, J., and J. Carrera, A comparison of hydraulic and transport parameters measured in low-permeability fractured media, *Journal of Contaminant Hydrology*, 41:261–281, 2000.

- [41] Gurevich, B., M. Brajanovski, R. Galvin, T. Müller, and J. Toms-Stewart, P-wave dispersion and attenuation in fractured porous reservoir - poroelasticity approach, *Geophysical Prospecting*, 57:225–237, 2009.
- [42] Gurevich, B., D. Makarynska, O. Bastos de Paula, and M. Pervukhina, A simple model for squirt-flow dispersion and attenuation in fluid-saturated granular rocks, *Geophysics*, 75:109–120, 2010.
- [43] Hainzl, S., T. Kraft, J. Wassermann, H. Igel, and E. Schmedes, Evidence for rainfall-triggered earthquake activity, *Geophysical Research Letters*, 33(L19303), 2006.
- [44] Hoek, E., and M. Diederichs, Empirical estimation of rock mass modulus, *International Journal of Rock Mechanics and Mining Sciences*, 43:203–215, 2006.
- [45] Holzapfel, G. A., *Nonlinear Solid Mechanics*, John Wiley, 2005.
- [46] Horne, R. N., *Modern well test analysis: a computer-aided approach*, Petro Way, 1996.
- [47] Hsieh, P. A., Deformation-induced changes in hydraulic head during ground-water withdrawal, *Ground Water*, 34(6):1082–1089, 1996.
- [48] Jäenicke, R., B. Quintal, and H. Steeb, Numerical homogenization of mesoscopic loss in poroelastic media, *European Journal of Mechanics - A/Solids*, under review.
- [49] Johnson, C., R. Greenkorn, and E. Woods, Pulse-testing: a new method for describing reservoir flow properties between wells, *Journal of Petroleum Technology*, 18(12):1599–1604, 1966.
- [50] Kamal, M., and W. Brigham, Pulse-testing response for unequal pulse and shut-in periods, *Society of Petroleum Engineers Journal*, 15:399–410, 1975.
- [51] Kim, J.-M., and R. R. Parizek, Numerical simulation of the Noordbergum effect resulting from groundwater pumping in a layered aquifer system, *Journal of Hydrology*, 202:231–243, 1997.
- [52] Kurzeja, P., and H. Steeb, About the transition frequency in Biot's theory, *Journal of the Acoustical Society of America (Express Letters)*, 131:EL454–EL460, 2012.
- [53] Kurzeja, P., H. Steeb, and J. Renner, The critical frequency in biphasic media: beyond Biot's approach, *American Society of Civil Engineers*, pages 2361–2370, 2013.
- [54] Landau, L., and E. Lifshitz, *Fluid Mechanics*, Butterworth-Heinemann, 1987.

- [55] Li, X., L. Zhong, and L. Pyrak-Nolte, Physics of partially saturated porous media: residual saturation and seismic-wave propagation, *Annual Review of Earth and Planetary Sciences*, 29:419–460, 2001.
- [56] Majer, E. L., R. Baria, M. Stark, S. Oates, J. Bommer, B. Smith, and H. Asanuma, Induced seismicity associated with enhanced geothermal systems, *Geothermics*, 36(3):185–222, 2007.
- [57] Matthews, C. S., and D. G. Russell. *Pressure buildup and flow tests in wells*, Monograph Series, Society of Petroleum Engineers, 1967.
- [58] Mavko, G., and A. Nur, Wave attenuation in partially saturated rocks, *Geophysics*, 44:161–178, 1995.
- [59] Mavko, G., T. Mukerji, and J. Dvorkin, *The Rock Physics Handbook: Tools for Seismic Analysis of Porous Media*, Cambridge University Press, 2009.
- [60] Mays, L., *Water Resources Engineering*, Wiley, 2010.
- [61] Munson, B., D. Young, T. Okiishi, and Huebusch, *Fundamentals of Fluid Mechanics*, John Wiley & Sons, 6th edition, 2009.
- [62] Murdoch, L. C., and L. N. Germanovich, Analysis of a deformable fracture in permeable material, *International Journal for Numerical and Analytical Methods in Geomechanics*, 30:529–561, 2006.
- [63] Murdoch, L. C., and L. N. Germanovich, Storage change in a flat-lying fracture during well tests, *Water Resources Research*, 48:W12528, 2012.
- [64] Nolte, D. D., L. J. Pyrak-Nolte, and N. G. W. Cook, The fractal geometry of flow paths in natural fractures in rock and the approach to percolation, *Pure and Applied Geophysics*, 131:111–138, 1989.
- [65] Ortiz, A. E., J. Renner, and R. Jung, Hydromechanical analyses of the hydraulic stimulation of borehole Basel 1, *Geophysical Journal International*, 185:1266–1287, 2011.
- [66] Ortiz, A., R. Jung, and J. Renner, Two-dimensional numerical investigations on the termination of bilinear flow in fractures, *Solid Earth*, 4: 331–345, 2013.
- [67] Pedrosa Jr., O. A., Pressure transient response in stress-sensitive formations, In *SPE California Regional Meeting, 2-4 April 1986, Oakland, California*, 1986. SPE 15115.
- [68] Pride, S., and Y. Masson, Acoustic attenuation in self-affine porous structures, *Physical Review Letters*, 97:184301, 2006.

- [69] Pyrak-Nolte, L. J., and J. P. Morris, Single fractures under normal stress: The relation between fracture specific stiffness and fluid flow, *International Journal of Rock Mechanics and Mining Sciences*, 37:245–262, 2000.
- [70] Quintal, B., Frequency-dependent attenuation as a potential indicator of oil saturation, *Journal of Applied Geophysics*, 82:119–128, 2012.
- [71] Quintal, B., H. Steeb, M. Frehner, and S. M. Schmalholz. Quasi-static finite element modeling of seismic attenuation and dispersion due to wave-induced fluid flow in poroelastic media, *Journal of Geophysical Research*, 116:B01201, 2011.
- [72] Quintal, B., H. Steeb, M. Frehner, S. M. Schmalholz, and E. Saenger, Pore fluid effects on S-wave attenuation caused by wave-induced fluid flow, *Geophysics*, 77:13–23, 2012.
- [73] Quintal, B., R. Jänicke, H. Steeb, G. Rubino, and K. Holliger, Effect of fracture connectivity and inclination on S- and P-wave attenuation in fluid-saturated rocks, *Geophysical Journal International*, under review.
- [74] Rasmussen, T., K. Haborak, and M. H. Young, Estimating aquifer hydraulic properties using sinusoidal pumping at the Savannah River site, South Carolina, USA, *Hydrogeology Journal*, 11:466–482, 2003.
- [75] Renner, J., and M. Messar, Periodic pumping tests, *Geophysical Journal International*, 167:479–493, 2006.
- [76] Renner, J., and H. Steeb, Modeling of fluid transport in geothermal research, In *Handbook of Geomathematics*, editors: Freeden, W., Nashed, M.Z., and Sonar, T., in press.
- [77] Renshaw, C., On the relationship between mechanical and hydraulic apertures in rough-walled fractures, *Journal of Geophysical Research*, 100(B12):24629–24636, Dec 10 1995.
- [78] Rice, J., and M. Cleary, Some basic stress diffusion solutions for fluid-saturated elastic porous media with compressible constituents, *Reviews of Geophysics*, 14:227–241, 1976.
- [79] Rodrigues, J. D., The Noordbergum effect and characterization of aquitards at the Rio Maior mining project, *Ground Water*, 21(2):200–207, 1983.
- [80] Roeloffs, E., Persistent water level changes in a well near Parkfield, California, due to local and distant earthquakes, *Journal of Geophysical Research*, 103:869–889, 1998.
- [81] Rojstaczer, S., and D. Agnew, The influence of formation properties on the response of water levels in wells to earth tides and atmospheric loading, *Journal of Geophysical Research*, 94:12403–12411, 1989.

- [82] Rubino, J. G., and K. Holliger, Research note: Seismic attenuation due to wave-induced fluid flow, *Geophysical Prospecting*, 61:882–889, 2013.
- [83] Rubino, J. G., L. Guarracino, T. Müller, and K. Holliger, Do seismic waves sense fracture connectivity?, *Geophysical Research Letters*, 40, 2013.
- [84] Rubino, J. G., T. Müller, L. Guarracino, M. Milani, and K. Holliger, Seismoacoustic signatures of fracture connectivity, *Solid Earth*, 119:2252–2271, 2014.
- [85] Shapiro, S. A., and C. Dinske, Scaling of seismicity induced by nonlinear fluid-rock interaction, *Journal of Geophysical Research*, 114:B09307, 2009.
- [86] Sibson, R., J. Moore, and A. Rankin, Seismic pumping - a hydrothermal fluid transport mechanism, *Journal of the Geological Society*, 131:653–659, 1975.
- [87] Simpson, D. W., W. S. Leith, and C. H. Scholz, Two types of reservoir-induced seismicity, *Bulletin of the Seismological Society of America*, 178 (6):2025–2040, 1988.
- [88] Slack, T. S., L. C. Murdoch, L. N. Germanovich, and D. B. Hisz, Reverse water-level change during interference slug tests in fractured rock, *Water Resources Research*, 49:1552–1567, 2013.
- [89] Sneddon, I. N., *Fourier Transforms*, Dover, 1995.
- [90] Steeb, H., P. Kurzeja, M. Frehner, and S. M. Schmalholz, Phase velocity dispersion and attenuation of seismic waves due to trapped fluids in residual saturated porous media, *Vadose Zone Journal*, 11, 2012.
- [91] Stegemeier, G., Interwell pressure testing for field pilots, *SPE*, SPE 11086, 1982.
- [92] Terzaghi, K., Die Berechnung der Durchlässigkeit des Tones aus dem Verlauf der hydromechanischen Spannungsercheinungen, *Sitzungsber. Akad. Wiss. (Wien), Mathematisch-Naturwissenschaftliche Klasse, Abteilung IIa*, 132:125–138, 1923.
- [93] Terzaghi, K., Stress conditions for the failure of saturated concrete and rock, *Proceedings of American Society for Testing Materials*, 45:777–792, 1932.
- [94] Valkó, P., and M. Economides, *Hydraulic Fracture Mechanics*, John Wiley & Sons, 1995.
- [95] Vasco, D., and S. Minkoff, Modelling flow in a pressure-sensitive, heterogeneous medium, *Geophysical Journal International*, 179:972–989, 2009.

- [96] Verruijt, A., Elastic storage of aquifers, In *Flow Through Porous Media*, editors: DeWiest, R.J.M., and J. Bear, Academic Press, New York, 1969.
- [97] Verruijt, A., *An Introduction to Soil Dynamics*, Springer, 2010.
- [98] Vinci, C., J. Renner, and H. Steeb, A hybrid-dimensional approach for an efficient numerical modeling of the hydro-mechanics of fractures, *Water Resources Research*, 50:1616–1635, 2014.
- [99] Vinci, C., J. Renner, and H. Steeb, On attenuation associated with fracture flow, *Geophysical Research Letters*, to be submitted.
- [100] Vinci, C., H. Steeb, and J. Renner, The imprint of hydro-mechanical effects in periodic pumping tests, *Geophysical Journal International*, to be submitted.
- [101] Walsh, R., C. McDermott, and O. Kolditz, Numerical modeling of stress-permeability coupling in rough fractures, *Hydrogeology Journal*, 16:613–627, 2008.
- [102] Wang, H., *Theory of Linear Poroelasticity with Applications to Geomechanics and Hydrogeology*, Princeton University Press, 2000.
- [103] Witherspoon, P. A., J. S. Y. Wang, K. Iwai, and J. E. Gale, Validity of cubic law for fluid flow in a deformable rock fracture, *Water Resources Research*, 16(6):1016 – 1024, 1980.
- [104] Zhang, M. Y., and A. K. Ambastha, New insights in pressure-transient analysis for stress-sensitive reservoirs, In *SPE Annual Technical Conference and Exhibition, 25-28 September 1994, New Orleans, Louisiana*, 1994. SPE 28420.
- [105] Zienkiewicz, O. C., A. Chan, M. Pastor, B. Schrefler, and T. Shiomin, *Computational Geomechanics With Special Reference to Earthquake Engineering*, John Wiley, 1999.
- [106] Zoback, M. D., and H. Harjes, Injection-induced earthquakes and crustal stress at 9 km depth at the KTB deep drilling site, Germany, *Journal of Geophysical Research*, 102:18,477–18,492, 1997.

CURRICULUM VITAE - Carlo VINCI

PLACE AND DATE OF BIRTH: Este, Italy | 03 April 1986

School Education

SEPTEMBER 1991 - Elementary School
JUNE 1996 Scuola Sacro Cuore, Monselice, Italy

SEPTEMBER 1996 - Middle School
JUNE 1999 Scuola Media Zanellato, Monselice, Italy

SEPTEMBER 1999 - High school degree in classical studies
JULY 2004 Liceo G.B. Ferrari, Este, Italy

SEPTEMBER 1998 - Music education (main instrument: cello)
JULY 2002 Conservatorio di musica C. Pollini, Padova, Italy

SEPTEMBER 2002 - Music education (main instrument: cello)
JULY 2005 Conservatorio di musica F. Venezzes, Rovigo, Italy

University Education

OCTOBER 2004 - B.Sc | Civil Engineering
JUNE 2007 Università degli Studi di Padova, Italy

OCTOBER 2007 - M.Sc | Computational Mechanics
NOVEMBER 2009 Technische Universität München, Germany

MAY 2008 Student assistant
Chair of Structural Analysis,
Technische Universität München, Germany

since JANUARY 2010 PhD student and research assistant
Chair of Continuum Mechanics and
Research group in Experimental Geophysics,
Ruhr-Universität Bochum, Germany

since APRIL 2010 Member of RUB Research School

Non-university Education and Experience

SUMMER OF 2003, Internship-Summer Job | Installation of photo-
2004, AND 2005 voltaic and thermic solar energy systems,
Seiler Gebäudetechnik, Bad Windsheim, Germany

**Mitteilungen aus dem Institut für Mechanik
RUHR-UNIVERSITÄT BOCHUM
Nr. 161**

ISBN 978-3-935892-39-1